Wearable pressure sensing for intelligent gesture recognition

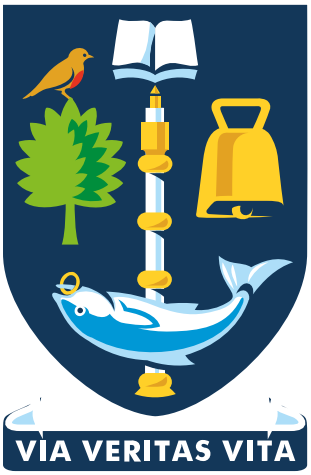

Yuchi Liu

James Watt School of Engineering

University of Glasgow

This dissertation is submitted for the degree of

Doctor of Philosophy

May 2023

Declaration

I hereby declare that except where specific reference is made to the work of others, the contents of this dissertation are original and have not been submitted in whole or in part for consideration for any other degree or qualification in this, or any other university. This dissertation is my own work and contains nothing which is the outcome of work done in collaboration with others, except as specified in the text and Acknowledgements.

Yuchi Liu
May 2023

Acknowledgements

First and foremost, I would like to express my deepest gratitude to my PhD supervisor, Dr. Rami Ghannam, for his endless support, patient guidance, and warm encouragement throughout my entire PhD journey. He always discovered and praised every progress I made and gave encouragement during tough times. His rigour and enthusiasm for research also inspired me to work hard. Next, I would like to thank my co-supervisors, Prof. Hadi Heidari and Dr. Francesco Fioranelli, for their technical guidance and support.

I would like to show great appreciate to Prof. Xiaosheng, who accepted me in his lab during the outbreak of COVID-19. He treated me as his own student and gave me full permission to access his lab. I am extremely grateful for his invaluable support in both research and life when I was lost. I had a joyful time in the IML group.

Many thanks also to my friends and colleagues in the MeLAB of UofG, especially Mengyao Yuan and Haobo Li, Jinwei Zhao, Kaung Oo Htet, Asfand Tanwear, Rupam Das and Adnan Zahid, for their friendship and those enjoyable moments. In addition, I would thanks to the friends in the IML lab of UESTC, Haitao Deng, Xinran Zhang, Danliang Wen, Yanyuan Ba, Yilin Wang, and so many others, for their kindness and help.

I must appreciate my husband, Xiangpeng Liang, for all his support and encouragement during my PhD. Finally, I would like to thank my parents for giving me unconditional love, endless encouragement and all aspects of support.

Abstract

The development of wearable sensors has become a major area of interest due to their wide range of promising applications, including health monitoring, human motion detection, human-machine interfaces, electronic skin and soft robotics. Particularly, pressure sensors have attracted considerable attention in wearable applications. However, traditional pressure sensing systems are using rigid sensors to detect the human motions. Lightweight and flexible pressure sensors are required to improve the comfortability of devices. Furthermore, in comparison with conventional sensing techniques without smart algorithm, machine learning-assisted wearable systems are capable of intelligently analysing data for classification or prediction purposes, making the system 'smarter' for more demanding tasks. Therefore, combining flexible pressure sensors and machine learning is a promising method to deal with human motion recognition.

This thesis focuses on fabricating flexible pressure sensors and developing wearable applications to recognize human gestures. Firstly, a comprehensive literature review was conducted, including current state-of-the-art on pressure sensing techniques and machine learning algorithms. Secondly, a piezoelectric smart wristband was developed to distinguish finger typing movements. Three machine learning algorithms, K Nearest Neighbour (KNN), Decision Tree (DT) and Support Vector Machine (SVM), were used to classify the movement of different fingers. The SVM algorithm outperformed other classifiers with an overall accuracy of 98.67% and 100% when processing raw data and extracted features.

Thirdly, a piezoresistive wristband was fabricated based on a flake-sphere composite configuration in which reduced graphene oxide fragments are doped with polystyrene spheres to achieve both high sensitivity and flexibility. The flexible wristband measured the pressure distribution around the wrist for accurate and comfortable hand gesture classification. The intelligent wristband was able to classify 12 hand gestures with 96.33% accuracy for five participants using a machine learning algorithm. Moreover, for demonstrating the practical applications of the proposed method, a real-time system was developed to control a robotic hand according to the classification results.

Finally, this thesis also demonstrates an intelligent piezoresistive sensor to recognize different throat movements during pronunciation. The piezoresistive sensor was fabricated using two PolyDimethylsiloxane (PDMS) layers that were coated with silver nanowires and reduced graphene oxide films, where the microstructures were fabricated by the polystyrene spheres between the layers. The highly sensitive sensor was able to distinguish throat vibrations from five different spoken words with an accuracy of 96% using the artificial neural network algorithm.

Table of Contents

Declaration ..... **II**

Acknowledgements ..... **III**

Abstract ..... **IV**

List of Figures ..... **IX**

List of Tables ..... **XVII**

List of Abbreviations ..... **XVIII**

1. Introduction **1**

1.1. Background and Motivation 1

1.2. Main Contributions 4

1.3. Thesis Overview 5

1.4. Publication List 7

2. Literature Review **9**

2.1. Review of Pressure Sensing Techniques 9

2.1.1. Piezoresistive Sensor 10

2.1.2. Piezoelectric Sensor 20

2.1.3. Other Sensing Techniques 27

2.1.4. Comparison Between Different Types of Pressure Sensors 30

2.2. Review of Classification Methods 32

2.2.1. Conventional Classifiers 33

2.2.2. Deep Learning Model 37

2.3. Summary 40

3. Piezoelectric Sensor for Finger Motions 42

3.1. Experimental Setup and Data Collection 44

3.2. Data Processing and Feature Extraction 49

3.3. Summary 54

4. Piezoresistive Sensor for Hand Gesture Recognition 56

4.1. Structure Design of Piezoresistive Sensor 58

4.2. Fabrication Process of Piezoresistive Sensor 59

4.3. Characterization 62

4.3.1. Characterization of AgNW 62

4.3.2. Characterization of GO and rGO 65

4.3.3. Working Principle and Sensing Performance 69

4.4. Sensor-Machine Interface Design and Analysis 75

4.4.1. Experimental Setup and Data Collection 75

4.4.2. Classification Results of Hand Gestures 79

4.4.3. Control Robot Hand in Real Time 82

4.5. Summary 85

5. Piezoresistive Sensor for Speech Recognition 88

5.1. Structure Design of Piezoresistive Sensor 91

5.2. Fabrication Process of Piezoresistive Sensor 92

5.3. Characterization and Working Principle 94

5.4. Sensor-Machine Interface Design and Analysis 105

5.5. Summary 108

6. Conclusions and Future Work 110

6.1. Conclusions 110

6.2. Future Work 112

Reference 114

List of Figures

Figure 1.1 An overview of various sensing technologies used for human motions recognition assisted with ML. 3

Figure 2.1 Schematic illustrations of sensing mechanisms of pressure sensors (a) piezoresistive, (b) capacitance, (c) piezoelectric and (d) triboelectric. 10

Figure 2.2 Schematic illustrations of structure strategies and transduction methods for piezoresistive sensors: (a) conductive polymeric composite, (b) porous conductive material, (c) architected conductive material. 12

Figure 2.3 Various piezoelectric energy harvesting techniques from different locations on the human body including (a) The shoulder [51], (b) Elbows, (c) The wrist, (d) Fingers [52], (e) Eyes, (f) Chest, (g) Knees [53], and (h) Feet [54]. 21

Figure 2.4 Piezoelectric material operated in (a) 31 mode, and (b) 33 mode. (c) Electromechanical equivalent circuit of the piezoelectric sensor. 23

Figure 2.5 Four working modes of triboelectric effect-based electronics. 28

Figure 2.6 Architecture of K nearest neighbour algorithm. 34

Figure 2.7 Architecture of decision tree. 35

Figure 2.8 Architecture of artificial neural network. 37

Figure 2.9 Architecture of convolutional neural network. 38

Figure 2.10 Architecture of recurrent neural network. 39

Figure 3.1 Building block of a typical wearable device. 44

Figure 3.2 Photograph of the piezoelectric sensors and the wristband. 45

Figure 3.3 (a) Schematic of signal conditioning circuit for piezoelectric sensor. (b) Frequency response plot of the charge mode amplifier circuit. 46

Figure 3.4 (a) The signal conditioning circuit design. (b) PCB layout. 47

Figure 3.5 Example piezoelectric voltage signal for middle finger tapping. 48

Figure 3.6 Examples of piezoelectric sensor output for five fingers. 49

Figure 3.7 Classification confusion matrix for the raw data of five tapping fingers (a) by using KNN algorithm with 94.67% accuracy; (b) by using DT algorithm with 88% accuracy; (c) by using SVM algorithm with 98.67% accuracy. (d) Cluster results for five fingers. 51

Figure 3.8 Classification accuracy for all five hand gesture using SVM with between 1 and 6 sensors. 54

Figure 4.1 The structure of the fabricated rGO/PS sensor. 58

Figure 4.2 (a) and (b) Photographs of the fabricated rGO/PS sensor with the dimension of 20 mm × 20 mm × 0.5 mm, which shows outstanding flexibility of the developed sensor. (c) and (d) Cross sectional SEM images

of the piezoresistive sensor. 59

Figure 4.3 Schematic illustration of the fabrication process of the flexible rGO/PS piezoresistive sensor. (a) 2 mg/ml AgNW ethanol-based solution was spray coated on the as-prepared PDMS film. (b) Doped the mixed GO/PS solution on the AgNW electrodes and the PDMS film, and heat for 3 hours until it obtained the dry film. (c) The GO/PS film was patterned by laser-induced reduction that directly converted GO into rGO. The color of the functional layer changed from dark brown to black. (d) Finally, the sensor was encapsulated by a thin PU film and a PDMS layer. 61

Figure 4.4 (a,b) Surface SEM images of AgNW electrodes in different magnifications. (c,d) TEM images of AgNW electrodes in different magnifications. (e) AFM image of AgNW. (f) Cross-sectional analysis of AgNW. 64

Figure 4.5 GO converted to rGO after laser reduction, where most of the oxygen functional groups were removed.....65

Figure 4.6 (a) Surface SEM image of GO. (b) Surface SEM image of rGO. (c) Cross-sectional SEM image of GO. (d) Cross-sectional SEM image of rGO. (e) TEM images of GO. (f) TEM images of GO. 67

Figure 4.7 AFM images and cross-sectional analysis of (d) GO, (e) rGO.....67

Figure 4.8 Raman spectra of GO and rGO. 68

Figure 4.9 Working principle of rGO/PS piezoresistive sensor. 70

Figure 4.10 (a) Cross-sectional SEM image of the fabricated GO/PS sensor. (b)

Cross-sectional SEM image of the fabricated rGO/PS sensor. (c) Surface SEM image of GO/PS structure. (d) Surface SEM image of rGO/PS structure. (e) Cross-sectional SEM image of fracture surface of the rGO/PS sensor. (f) A magnified SEM image of the fracture surface, showing that the PS spheres are sandwiched between the rGO layers. 70

Figure 4.11 The relationship between applied force and resistance changes with (a) different doping PS spheres sizes, (b) different doping PS sphere weight ratios.....71

Figure 4.12 The photographs of the flexible sensor: (a) non-doped GO film; (b) 2 μm PS spheres doped GO film at 0.5 wt%; (c) 2 μm PS spheres doped GO film at 1 wt%; (d) 2 μm PS spheres doped GO film at 0.4 wt%; (e) 2 μm PS spheres doped GO film at 0.4 wt%, and half part is reduced by laser, which shows the color of the film changes from the dark brown to black; (f) 2 μm PS spheres doped rGO film at 0.4 wt%. 72

Figure 4.13 (a) The resistance change of the rGO/PS sensor depends on different weights. (b) The piezoresistive sensor shows rapid response and relaxation time. (c) Test the repeatability performance of 1000 cycles under a pressure of 3 N. 74

Figure 4.14 (a) The resistance value of the developed sensor under different humidity environments. (b) A comparison of the resistance changes of the sensor during finger tapping movements in air and water at room temperature. 75

Figure 4.15 Photographs of flexible piezoresistive wristband.....76

Figure 4.16 (a) Circuit schematic diagram and (b) PCB board layout for piezoresistive wristband signals transfer. 76

Figure 4.17 Schematic diagram of hand gesture recognition system. 77

Figure 4.18 Generated signal patterns for different hand gestures, and the corresponding pressure maps on the smart wristband. 79

Figure 4.19 (a) Classification confusion matrix for all 12 hand gestures, the accuracy was 96.33%. (b) t-SNE analysis for all 12 gestures. (c) Classification confusion matrix for 8 finger flexion, the accuracy was 97%. (d) Classification confusion matrix for 4 wrist movements, the accuracy was 100%. 82

Figure 4.20 The schematic diagram of the proof-of-concept real-time control for HMI. 83

Figure 4.21 LabVIEW interface of collecting gesture signals and showing recognition results to control a robotic hand in real-time. 84

Figure 4.22 Real-time robotic hand control with flexible piezoresistive wristband. 84

Figure 4.23 Robotic hand controlled by flexible wristband. 85

Figure 5.1 (a) Schematic diagram of the piezoresistive sensor. (b) Photograph of the fabricated sensor which shows outstanding flexibility. (c) AgNWs solution was sprayed onto the as-prepared PDMS film. (d) PS solution was sprayed onto the AgNWs film. (e) The rGO film was prepared by laser-induced reduction that directly converted GO into rGO. 92

Figure 5.2 SEM image of (a) AgNWs, (b) PS spheres on the AgNWs film and (c) rGO. 94

Figure 5.3 (a) Schematic diagram of the working principle of the AgNW/rGO piezoresistive sensor without PS microspheres during (i) release and (ii) pressure cycles. (b) Cross-sectional SEM image of AgNW/rGO piezoresistive sensor, indicating some contact points between the AgNWs layer and the rGO layer at release state. (d) Schematic diagram of the working principle of the AgNW/PS/rGO sensor during (i) release and (ii) pressure cycles. (d) Cross-sectional SEM image of AgNW/PS/rGO piezoresistive sensor, where PS spheres separate the AgNWs layer from the rGO layer at release state. 96

Figure 5.4 (a) The resistance changes of the AgNWs/rGO sensor without PS spheres under different pressure. (b) The resistance changes of the AgNWs/rGO sensor without PS spheres under different pressure. 96

Figure 5.5 The resistance changes of the sensor with different diameters of PS spheres at 0.25 wt%,0.025 wt% and 0.0025 wt% under 10 kPa. 98

Figure 5.6 (a) The resistance changes of the sensor with 40 μm PS spheres at 0.25 wt% and the sensor without PS spheres under different pressure. (b) The resistance changes of the sensor with 40 μm PS spheres at 0.25 wt% under different pressure. 98

Figure 5.7 SEM images of (a) 2 μm PS spheres at 0.0025 wt%. (b) 2 μm PS spheres at 0.025 wt%. (c) 2 μm PS spheres at 0.25 wt%. (d) 2 μm PS spheres at 2.5 wt%. (e) 20 μm PS spheres at 0.0025 wt%. (f) 20 μm PS

spheres at 0.025 wt%. (g) 20 μm PS spheres at 0.25 wt%. (h) 20 μm PS spheres at 2.5 wt%. (i) 40 μm PS spheres at 0.0025 wt%. (j) 40 μm PS spheres at 0.025 wt%. (k) 40 μm PS spheres at 0.25 wt%. (l) 40 μm PS spheres at 2.5 wt%. 99

Figure 5.8 (a) The response and recovery time of the prepared sensor. (b) Test of the repeatability performance over 5000 cycles under 10 kPa. 101

Figure 5.9 (a) The PS sphere on the AgNW layer before testing. (b) The PS spheres on the AgNW layer after testing. (c) The PS spheres on the rGO layer after testing.....101

Figure 5.10 (a) The resistance value of the developed sensor under temperatures.The resistance change decreased by 0.04 when temperature increased from 20 ℃ to 50 ℃. (b) The resistance value of the developed sensor under different humidity environments. The resistance of the developed sensor remained stable when the relative humidity changed by about 30%. 102

Figure 5.11 The prepared sensor was used to monitor different mechanical forces (a) compression and (b) bending, as well as various human body activities (c) finger movements, (d) eye blinking, (e) wrist flexion at different angles and (f) throat movements. 104

Figure 5.12 The resistance changes of the sensor before and after repeated bending.....104

Figure 5.13 (a) Schematic diagram of the speech recognition process. (b) Cluster results of word signals. (c) Classification confusion matrix for 5 different

pronunciations. 106

Figure 5.14 Training epoch of the ANN classifier. 108

List of Tables

Table 2.1 State-of-the-art flexible piezoresistive sensor for human motion. 17

Table 2.2 State-of-the-art flexible piezoelectric sensor for human motion.....26

Table 2.3 Comparison of the typical features of wearable pressure sensors. 31

Table 2.4 State-of-the-art pressure sensor for human motions with ML algorithm. 39

Table 3.1 Features extracted from the piezoelectric sensors in time domains. ...52

Table 3.2 Classification results of different algorithms by using six piezoelectric sensors. 53

Table 4.1 The comparison of different fabrication processes of AgNW. 63

Table 4.2 Features extracted from the wristband signals. 80

Table 4.3 Performance comparison of hand gesture recognition system with rGO/PS flexible wristband and similar wristband products. 87

Table 5.1 Parameters for the ANN training. 107

Table 5.2 Performance comparison of developed flexible sensor and similar intelligent throat products. 109

List of Abbreviations

ACC	Accelerometer
AFM	Atomic Force Microscopy
AgNW	Silver Nanowires
ANN	Artificial Neural Network
CB	Carbon Black
CNN	Convolutional Neural Network
CNT	Carbon Nanotubes
DT	Decision Tree
ECG	Electrocardiograph
EEG	Electroencephalograph
EMG	Electromyography
FEM	Finite Element Method
GO	Graphene Oxide
HMI	Human-Machine Interface
ITO	Indium Tin Oxide
KNN	K Nearest Neighbour
LDA	Linear Discrimination Analysis

LSTM	Long Short-Term Memory
ML	Machine Learning
OCG	Oxygen-Containing Groups
PDMS	Polydimethylsiloxane
PET	Polyethylene Terephthalate
PI	Polyimide
PLA	Polylactic Acid
PMMA	Polymethyl Methacrylate
PP	Polypropylene
PPG	Photoplethysmogram
PS	Polystyrene
PU	Polyurethane
PVDF	Polyvinylidene Difluoride
PZT	Lead Zirconate Titanate
rGO	Reduced Graphene Oxide
RNN	Recurrent Neural Network
SEM	Scanning Electron Microscope
SVM	Support Vector Machine
TEM	Transmission Electron Microscope
t-SNE	T-Distributed Stochastic Neighbour Embedding

Chapter 1

Introduction

1.1. Background and Motivation

A sensor is a device that detects and responds to a physical stimulus, such as light, heat, pressure, motion, or sound and converts it into a measurable electrical signal [1]. Due to the rapid development of the electronics industry in recent decades, various sensors along with their readout circuit became increasingly accurate, robust and miniaturised, thus enabling their wearable applications. Wearable sensing is a promising field that has received considerable attention in the 21st century. The global market size of wearable technology was estimated at USD 52.14 billion in 2021 and is expected to grow at a compound annual growth rate of 14.9% from 2022 to 2030 [2].

An increasing number of customers are using smart wearable technology products to track physiological information and human activities for healthcare monitoring [3-7], human-machine interaction [8, 9], assistive living [10], etc. Given the potential of

wearable electronics, the recent advances in Machine Learning (ML) further boost the application scenarios of the sensory system [11, 12]. Using ML algorithms can empower a sensing system with the capabilities of information extraction, pattern recognition and noise cancelling. Particularly, ML algorithms can properly process mass sensory signals in an intelligent and trainable manner. These novel functionalities make the sensor 'smarter' and thus enable more applications. For example, (i) the combination of optical sensor (camera) and convolutional neural network (a brain-inspired ML algorithm commonly used in image processing) can achieve face recognition and object detection [13], which has been massively deployed on our cell phone; (ii) the combination of radar sensor and recurrent neural network (a brain-inspired ML algorithm suitable for analysing time-dependent data) can protect elderly people by recognizing their activities in a privacy-preserving way, and even detecting their heartbeat rate wirelessly [14, 15]; (iii) in wearable domain, ML can indirectly access human activities and physical condition through processing the output of wearable sensors [16, 17]. Figure 1.1 gives examples about wearable sensors and signals in which bio-potential—electrical signals that are generated by philological processes occurring within the body, including Electromyography (EMG), Electroencephalograph (EEG), Electrocardiograph (ECG), has been well-studied for human-machine interface and health monitoring. In addition to bio-potential, there are various novel wearable sensing systems with ML algorithms that have been developed to work in recent years, such as Photoplethysmogram (PPG) [18].

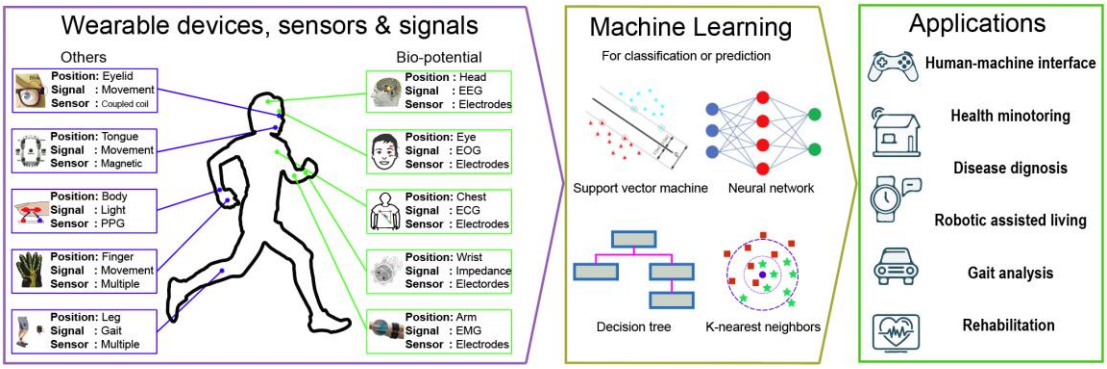

Figure 1.1 An overview of various sensing technologies used for human motions recognition assisted with ML.

Benefiting from a number of attractive features, such as light weight, good compliance, and desirable comfortability, pressure sensors have attracted much attention in wearable applications. Pressure sensing techniques are able to directly convert physical stimuli to measurable electrical signals such as the variation of resistance, capacitance or generation of charges. Hence, the conversion mechanism of electromechanical sensors can generally be divided into piezoresistive, piezocapacitive, piezoelectric and triboelectric types. With the fast development of wearables, higher requirements are placed on electromechanical sensors. High sensitivity, excellent flexibility, fast response time and good durability are some of the essential characteristics for wearable devices. Hence, researchers have made great efforts to explore new materials [19], structures [20] and fabrication processes [21] to improve the performance of sensors.

The integration of pressure sensing techniques and ML algorithms enhance the intelligence of wearable systems. Researchers currently focus on developing lightweight, flexible and miniaturized wearable sensors and use ML algorithms to process sensory data. Assisted with ML algorithms, electromechanical sensing

systems can analyse the collected data more thoroughly and process more accurate classification results.

1.2. Main Contributions

This thesis focuses on the fabrication of high-performance wearable sensors and their combination with machine learning algorithms for novel applications. Thus, three wearable applications were designed based on the wearable pressure sensors to recognize different human activities. My work involves theoretical analysis, structural design, fabrication process, sensor characterization, experimental setup, data collection, data processing and human-machine interface exploration in each wearable device.

The main contributions and innovations of this thesis are as follows:

- A wristband was developed based on piezoelectric sensors to distinguish finger movements. Three ML algorithms, K Nearest Neighbour (KNN), Decision Tree (DT) and Support Vector Machine (SVM) were implemented to classify different finger movements. The SVM algorithm achieved the best performance with a classification accuracy of 98.35% for raw data and 100% for extracted features.

- A highly flexible piezoresistive wristband was designed and fabricated. The wristband integrated five piezoresistive sensors based on Reduced Graphene Oxide (rGO). The total wristband weight was only 2.8 g, which is comfortable for users to wear. The flexible wristband was able to recognize 12 hand gestures of five subjects using an ML algorithm with a high accuracy of 96.33%. Moreover, a human-machine interface was developed to control a robotic hand in real time

followed by the user's hand when wearing the smart wristband.

- A new and simple approach was developed to fabricate microstructures for the piezoresistive sensor. Polystyrene (PS) microspheres were spray coated between two conductive layers, which acted as insulator microstructures to change the conductive pattern of the sensor. The microstructure can be changed simply by varying the weight ratio and size of the PS spheres. In comparison with other architecture design strategies, such as photolithography, which have complex preparation processes and high equipment requirements, this microstructure fabrication process has the advantage of one-step process and low-cost equipment.

- A new approach to recognising speech using a wearable device was proposed. The wearable intelligent throat was attached to the user's throat to detect muscle movement and vibration when the user spoke. The device was highly flexible and lightweight, which is more comfortable than the traditional hand-held electrolarynx. Moreover, the intelligent throat not only detects sounds but also classifies the pronunciation of different words. When attaching the sensor on the human throat, it can distinguish the throat vibrations of speaking five different words by the Artificial Neural Network (ANN) algorithm with a high accuracy of 96%. As far as we know, this work achieves the highest accuracy in recognizing word pronunciations than recent publications.

1.3. Thesis Overview

The organisation and content of the thesis are as follows:

Chapter 2 presents state-of-the-art pressure sensing techniques for wearable devices

to detect human motions, which include piezoresistive, piezoelectric, triboelectric and capacitive. The working mechanisms and structures of each electromechanical sensor are discussed in detail. In addition, ML algorithms are also introduced in this chapter. The recent progress in ML-assisted wearable applications for human gesture recognition is outlined.

Chapter 3 provides a wristband consisting of piezoelectric sensors to classify different finger motions. A smart wristband based on lead zirconate titanate (PZT) sensors was fabricated to achieve hand gesture recognition, and the classification results of different ML algorithms were compared.

Chapter 4 describes a flexible piezoresistive wristband system to classify different hand gestures. The fabrication process and characterization of the rGO/PS flexible sensor are provided in this chapter. Next, a flexible piezoresistive wristband with an array of five sensors was fabricated to recognize 12 different hand gestures using the SVM algorithm. Moreover, a human-machine interface was developed to control a robotic hand in real-time.

Chapter 5 presents an intelligent throat to classify different word pronunciations. The fabrication processes and characterization of the flexible piezoresistive sensor are provided. With the help of the deep learning algorithm, the sensor was able to distinguish throat vibrations for five different spoken words.

Chapter 6 summarizes the key outcome of the research work and provides suggestions for future works.

1.4. Publication List

Journal Publication

[1] **Y. Liu** *et al.,* " Speech Recognition Using Intelligent Piezoresistive Sensor Based on Polystyrene Sphere Microstructures," *Advanced Intelligent Systems,* Accepted for publication.

[2] **Y. Liu** *et al.,* "Ultralight Smart Patch with Reduced Sensing Array Based on Reduced Graphene Oxide for Hand Gesture Recognition," *Advanced Intelligent Systems,* vol. 4, no. 11, p. 2200193, 2022/11/01 2022.

[3] **Y. Liu** *et al.,* "Piezoelectric energy harvesting for self-powered wearable upper limb applications," *Nano Select,* vol. 2, no. 8, pp. 1459-1479, 2021.

[4] J Zhao, R Ghannam, KO Htet, **Y Liu** *et al.,* "Self-Powered Implantable Medical Devices: Photovoltaic Energy Harvesting Review," *Advanced Healthcare Materials,* vol. 9, no. 17, p. 2000779, 2020/09/01 2020.

[5] A Tanwear, X Liang, **Y Liu** *et al.,* "Spintronic Sensors Based on Magnetic Tunnel Junctions for Wireless Eye Movement Gesture Control," *IEEE Transactions on Biomedical Circuits and Systems,* vol. 14, no. 6, pp. 1299-1310, 2020.

[6] H Li, X Liang, A Shrestha, **Y Liu** *et al.,* "Hierarchical Sensor Fusion for Micro-Gesture Recognition With Pressure Sensor Array and Radar," *IEEE Journal of Electromagnetics, RF and Microwaves in Medicine and Biology,* vol. 4, no. 3, pp. 225-232, 2020.

[7] X Liang, H Li, W Wang, **Y Liu** *et al.*, "Fusion of Wearable and Contactless Sensors for Intelligent Gesture Recognition," *Advanced Intelligent Systems,* vol. 1, no. 7, p. 1900088, 2019/11/01 2019.

Conference Proceedings

[1] **Y. Liu**, S. Zuo, X. Liang, H. Khanbareh, H. Heidari, and R. Ghannam, "Gesture Recognition Wristband Device with Optimised Piezoelectric Energy Harvesters," in *2020 27th IEEE International Conference on Electronics, Circuits and Systems (ICECS)*, 2020, pp. 1-4.

Book Chapter

[1] R Ghannam, Y Hao, **Y Liu** and Y Xiao, "Energy Harvesting for Wearable and Portable Devices," in *Engineering and Technology for Healthcare*: IEEE, 2021, pp. 129-152.

Chapter 2

Literature Review

Rapid development in wearable electronics has greatly changed the way people live. People have become accustomed to using smart wearable products, such as smart watch, fitness trackers and heart rate monitors to track physiological information and human activities for healthcare monitoring, assistive living and entertainment [22]. In this chapter, a brief overview of pressure sensing techniques is presented, including the material, structure and applications in smart wearables. The advantages and disadvantages of each sensing techniques are discussed. In addition, the current classification methods for human activities recognition are also shown in this chapter.

2.1 Review of Pressure Sensing Techniques

Recent advances in wearable pressure sensors have attracted great interest in the fields of wearable electronics, electronic skins, medical diagnosis and physical health detection. Traditional pressure sensors are generally based on metal or semiconductor

materials that are rigid and unsuitable for uneven surfaces. In this case, flexible pressure sensors have been extensively investigated due to their excellent sensitivity, simple structure and light weight. Nowadays, plenty of pressure sensing mechanisms have been explored to achieve the conversion between mechanical and electrical signals, which are mainly divided into four categories: piezoresistive, capacitive, piezoelectric and triboelectric, as shown in Figure 2.1. In the following parts, the working principle of each transduction method will be explained in detail.

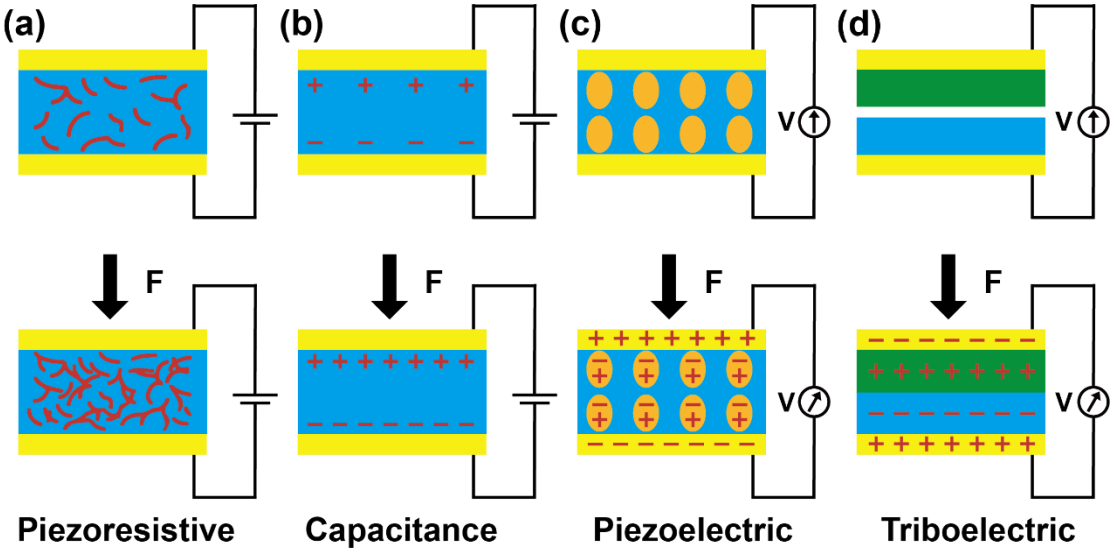

Figure 2.1 Schematic illustrations of sensing mechanisms of pressure sensors (a) piezoresistive, (b) capacitance, (c) piezoelectric and (d) triboelectric.

2.1.1 Piezoresistive Sensor

Piezoresistive sensors detect pressure by changes in the resistivity of a material. When pressure is applied, the changing contact area or density of the conductive material leads to the variation of material resistance, and then the pressure is detected according to the change of resistance. Typically, the resistance of the conductor (R) is

given by:

$$R = \frac{\rho L}{A} \tag{2.1}$$

where L represents the length, ρ is the conductor's resistivity, and A represents the cross-sectional area of the sensor. Additionally, variations in contact resistance (R_c) can also significantly affect resistance. R_c varies with applied force due to changes in contact area or geometry between materials. The relationship between applied force F and R_c for a piezoresistive sensor is defined as follows:

$$R_c \propto F^{-\frac{1}{2}} \tag{2.2}$$

The piezoresistive-based pressure sensors have advantages in simple construction and readout circuits, low power consumption and robustness of both static and dynamic pressure, which are widely used in wearable intelligent electronics. With the development of wearable systems, there are more requirements for piezoresistive sensors, for example, the excellent flexibility, high sensitivity, fast response time, wide detection range, outstanding mechanical durability and good biocompatibility. However, traditional piezoresistive pressure sensors made of metals or inorganic semiconductors are difficult to meet these requirements [23]. Therefore, new materials and architectures of piezoresistive sensors are being explored to achieve better performance.

Flexible piezoresistive sensors can be divided into three types according to their structure characteristics:

- Conductive polymer composite — polymer matrix dispersed with conductive

fillers.

- Architected conductive material — conductive material system with carefully designed geometry.

- Porous conductive material — conductive material with three-dimensional interconnected porous structure.

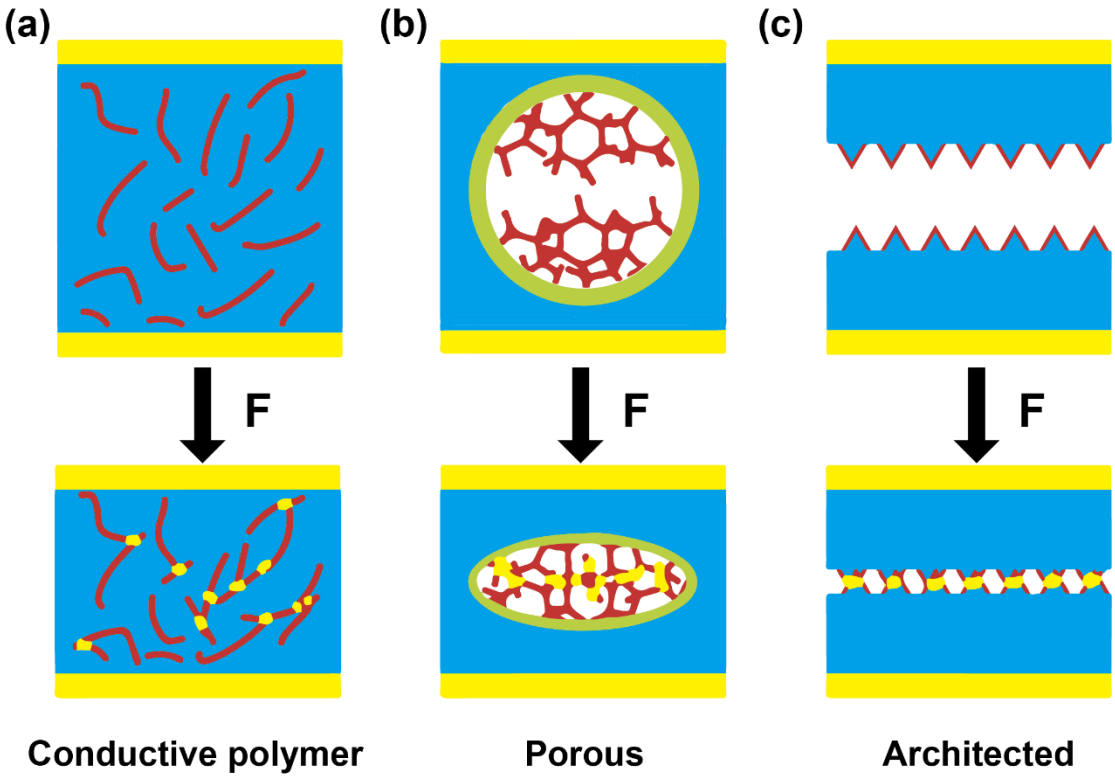

Figure 2.2 Schematic illustrations of structure strategies and transduction methods for piezoresistive sensors: (a) conductive polymeric composite, (b) porous conductive material, (c) architected conductive material.

- **Conductive polymer composite**

  Polymers are insulating matrices that are characterised by excellent optical and mechanical properties. Polymeric sensors doped with conductive fillers possess

both the excellent electrical properties of conductors and the remarkable mechanical properties of flexible polymers. Therefore, many attempts have been made on particle-incorporated polymeric sensors to study their electrical properties and conduction patterns.

Many commercially available polymers are chosen as polymeric matrices, including PDMS [24, 25], Ecoflex, Polyurethane (PU) [26], Polyvinylidene Difluoride (PVDF) [27], Polymethyl Methacrylate (PMMA), Polylactic Acid (PLA), Polypropylene (PP) and epoxy. These polymers possess low Young's modulus, intrinsic extensibility, high transparency, excellent stability, and easily preparation, which are advantageous in flexible wearable electronics. The conductive fillers used in the flexible piezoresistive polymeric sensors typically contain metallic materials (*e.g.* metal particles and metal nanowires), carbon-based micro/nanophases (*e.g.* Carbon Nanotubes (CNTs), Carbon Black (CB), and graphene nanoplatelets [25, 28]), conductive polymers (e.g. Polypyrrole (PPy), Polyaniline (PANI) and Poly(3,4-ethylenedioxythiophene): Polystyrene Sulfonate (PEDOT:PSS) and liquid metals [29].

Conductive polymers are widely used in wearable electronics to detect human motions. For instance, a transparent conductive polymer composed of sea-urchin shaped metal nanoparticles and PU elastomer was demonstrated to detect minute movements of human muscles, such as finger bending and hand motion [26]. Besides, a novel piezoresistive sensor was prepared by graphene nanoplatelets and PDMS elastomer [25]. The obtained piezoresistive sensor showed tunable piezoresistivity under different graphene nanoplatelets concentrations. To demonstrate potential applications, the obtained sensor was able to distinguish the

finger motions accurately.

Conductive polymer composites are commonly prepared by mixing the conductive fillers and polymers in low-frequency stirring, which is a quick, simple, and low-cost fabrication process. The large selection of materials and the weight ratios allows both electrical and mechanical properties of developed sensors to be tuned. However, the doped conductors are usually randomly orientated and distributed within the polymer matrix, which would limit the performance and functionality of the piezoresistive sensors. Moreover, the choice of the mix ratio of the conductive fillers and the polymer material needs to be careful, as the high ratio of fillers leads to the reduction of flexibility which will restrict the application of piezoresistive sensors in the field of wearable devices.

- **Architected conductive material**

To achieve higher sensitivity, the architectural design has been incorporated into sensor development. The designed microstructures could amplify mechanical loading effects, and the resulting resistance change in the material system can be enlarged which leads to better sensitivity.

One of the most common strategies is the template-assisted method to develop microstructures. Silicon templates are usually prepared by photolithography, and the size and shape of the microstructure can be controlled according to actual needs [30]. Furthermore, the template-assisted method enables mass production and reuse of templates [31]. Typically geometry structures such as dome [32], wave [33], pillar [34, 35], fibres [36] and pyramid [37] shapes are involved. The regular and uniform microstructure offers piezoresistive sensors better

performance and small sizes. For example, a highly sensitive piezoresistive sensor was built by rGO/PDMS pyramid microstructure array affixed to a flat conductive Indium Tin Oxide (ITO)-coated flexible Polyethylene Terephthalate (PET) film face-to-face [38]. The microstructured piezoresistive sensor achieved the sensitivity of -5.5 kPa^{-1} at low pressure range (<100 Pa), which is more than 50 times higher than that of the unstructured counterpart. However, the procedures of micro/nanofabrication technologies are always complex, high cost, and high equipment requirements. Moreover, the designed microstructures usually have single shapes and are mostly periodic, making it difficult to use them for multi-level structures [31].

In addition to the artificial designed template method, much research has been inspired by nature architectures to obtain various microstructures. Living organisms in nature have developed a great number of materials with abundant microstructures. Sensors with bionic patterns are proven to present excellent performance. Leaves are the functional organs for plants that are rich in natural micro/nanostructures after long-term evolution, which can be used as low-cost and eco-friendly templates to prepare microstructural sensors with high sensitivity. For example, the hierarchical microstructure was obtained by mimicking banana leaves and improved the sensor sensitivity to 10 kPa^{-1} [39]. Other bionic pattern of plants such as petals of rose [40], mimosa [41] and lotus leaves [42] are also reported as good moulds for preparing microstructures to enhance device performance. Compared with the template-based methods, the manufacturing process for bioinspired sensors is simple and has less requirement for the equipment.

- **Porous conductive material**

The porous structures present an alternative approach to realise the dynamic conductive pathway of flexible piezoresistive sensors with excellent stability. The 3D interconnected architectures endow the pressure senor with large surface area, low density, high porosity and high flexibility. For example, a soft porous composite pressure sensor was fabricated by 3D printing technology [43]. The printing ink was prepared by mixing silicone elastomer polymer with conductive CNTs and insulating silica nanoparticles SiNP fillers, where SiNPs were used to change the rheological properties and piezoresistive mechanism of the sensor. The piezoresistive coefficient can be tuned by changing the weight ratios of CNTs and SiNPs. At low CNT content and high SiNP content, the printed sensor showed a positive piezoresistive coefficient, resulting in high sensitivity and a large pressure detection range. The obtained pressure sensor was demonstrated to be used in grasp sensing and gait monitoring systems.

Commercially available sponges have been used to fabricate the pressure sensors, and various conductive fillers are chosen to decorate 3D microporous material, such as rGO [44], multiwalled carbon nanotubes (MWNT)–rGO [45] and Au [46]. For example, a simple and low-cost CB @ PU sponge was proposed [47]. The CB was uniformly coated on PU sponges by natural polymer-mediated water-based layer-by-layer assembly. The conductive CB@PU sponges exhibit excellent sensitivity and fast response time which can monitor various human activities such as pronouncing, coughing, swallowing, pulse, breathing, joint bending, etc. besides the commercial sponges based, various conductive sponges

have been realized by a variety of routes, including chemical vapor deposition, cellulose nanofiber sponges, and carbonization of hybrid (metal–polymer) nanocable sponges to develop piezoresistive sensors.

Aerogels and hydrogels are other forms of 3D porous structures that a considerable number of studies have focused on piezoresistive aerogel sensors. For example, a piezoresistive sensor based on hybrid MXene/rGO aerogel was fabricated by a simple ice-template freezing technique [48]. The sensor with highly ordered hierarchical architectures is advanced in sensitivity and durability, and it can recognize subtle human activities such as throat movements and pulse beating. Besides, another MXene-based aerogel was constructed by MXene nanosheets and Cellulose Nanocrystals (CNCs) [49]. The interaction between MXene and CNCs produces a wave-shaped lamellar architecture that shows an ultrahigh sensitivity of 114.6 kPa^{-1} in low-pressure range. In [50], a novel microsphere-structured hydrogel was proposed by in situ synthesizing Polyacrylamide (PAM) and Polyaniline (PANI) in closely packed swollen chitosan microspheres. Due to the mismatch between the hard microspheres and the soft substrate, the surface of the hydrogel is self-wrinkling, conferring a wide pressure detection range (100 Pa-6 MPa) to the sensor.

Table 2.1 State-of-the-art flexible piezoresistive sensor for human motion.

Category	**Material**	**Structure**	**Sensitivity**	**Response time**	**Durability**	**Detection limit**	**Human motion monitoring**	**Ref**
Conductive	Metal	Conductiv	2.46 kPa^{-1}	30 ms	200 cycles	N/A	Finger bending	[26]

polymeric composite	nanoparticles/ PU	e polymer					and hand motion	
Architected conductive material	CNT/PDMS	Dome	−15.1 kPa^{-1}	40 ms	N/A	0.2 Pa	Finger bending, human breathing, voice monitoring	[32]
Architected conductive material	CNT/PDMS	Pillar–wrinkle	20.9 kPa^{-1}	24 ms	10000 cycles	2 Pa	Finger bending, foot postures	[35]
Architected conductive material	rGO/PDMS/ITO-PET	Pyramid Microstructure	–5.53 kPa^{-1}	0.2 ms	5000 cycles	1.5 Pa	Finger touch	[38]
Architected conductive material	Ag/PDMS	Banana leaves microstructure	10 kPa^{-1}	36 ms	10000 cycles	1 Pa	Pronouncing, wrist pulses, forearm muscle contraction, breathing	[39]
Architected conductive material	Cu–Ag NWs/PDMS	Rose petal microstructure	1.35 kPa^{-1}	36 ms	5000 cycles	2 Pa	Voice recognition, wrist pulse	[40]
Architected conductive material	Ti/Au/PDMS	Mimosa leaves microstructure	50.17 kPa^{-1}	20 ms	10000 cycles	10.4 Pa	Finger touch	[41]
Porous conductive material	MXene/rGO	Aerogel	22.56 kPa^{-1}	<200 ms	>10000 cycles	10 Pa	Pronouncing, jugular venous pulse of neck, arterial pulse of	[48]

							wrist	
Porous conductive material	CB@PU	Sponge	0.068 kPa^{-1}	<20 ms	>50 000 cycles	91 Pa	Pronouncing, coughing, swallowing, pulse, breathing, joint bending	[47]
Porous conductive material	CNTs/ SiNPs/ Ecoflex silicone rubber	Porous	0.096 kPa^{-1}	N/A	10000 cycles	N/A	Grasp sensing and gait monitoring	[43]
Porous conductive material	rGO@PU	Sponge	0.26 kPa^{-1}	N/A	>10000 cycles	9 Pa	Heartbeat	[44]
Porous conductive material	MWNT–rGO@PU	Foam	0.088 kPa^{-1}	30 ms	5000 cycles	3.7 Pa	Pronouncing, pulsing of blood, blowing of air through the cheeks, and bending and extension of fingers	[45]
Porous conductive material	Au@PU	Sponge	0.122 kPa^{-1}	9 ms	1000 cycles	0.568 Pa	Speech recognition systems, heart monitoring	[46]
Porous conductive material	MXene +CNCs	Aerogel	114.6 kPa^{-1}	189 ms	10000 cycles	1.0 Pa	Finger clicks; bending finge; Pulse signal detection,	[49]

							pronouncing,	
Porous conductive material	PAAm+ PANI+ chitosan microspheres	Hydrogel	0.35 kPa^{-1}	N/A	5000 cycles	100 Pa	Hand grasping	[50]

2.1.2 Piezoelectric Sensor

Piezoelectric materials have the ability to directly convert changes in mechanical stimuli into voltage signals without any further external input. Piezoelectric sensors are constructed by piezoelectric materials and electrodes, as shown in the Figure 2.1(c). Hence, the architecture of the piezoelectric sensor is simple, which is particularly advantageous in small-scale wearable devices. As shown in Figure 2.3.

The direct piezoelectric effect is the ability of certain crystalline materials to develop an electric charge proportional to the mechanical stress, which was first discovered in quartz by Pierre and Jacques Curie in 1880 [51]. Equation 2.3 shows the basic principle of the direct piezoelectric effect.

$$D_i = d_{ij} \cdot T_j + \varepsilon_{ik}^{T} \cdot E_k \tag{2.3}$$

where D_i is the electric displacement, T_j is the stress tensor, E_k is the electric field, ε_{ik}^{T} is the dielectric permittivity under zero or constant stress, d_{ij} is the direct piezoelectric charge coefficient [52]. Where *i* and *k* vary from 1 to 3, and *j* varies from 1 to 6. The detailed constitutive matrix is described in Equation 2.4.

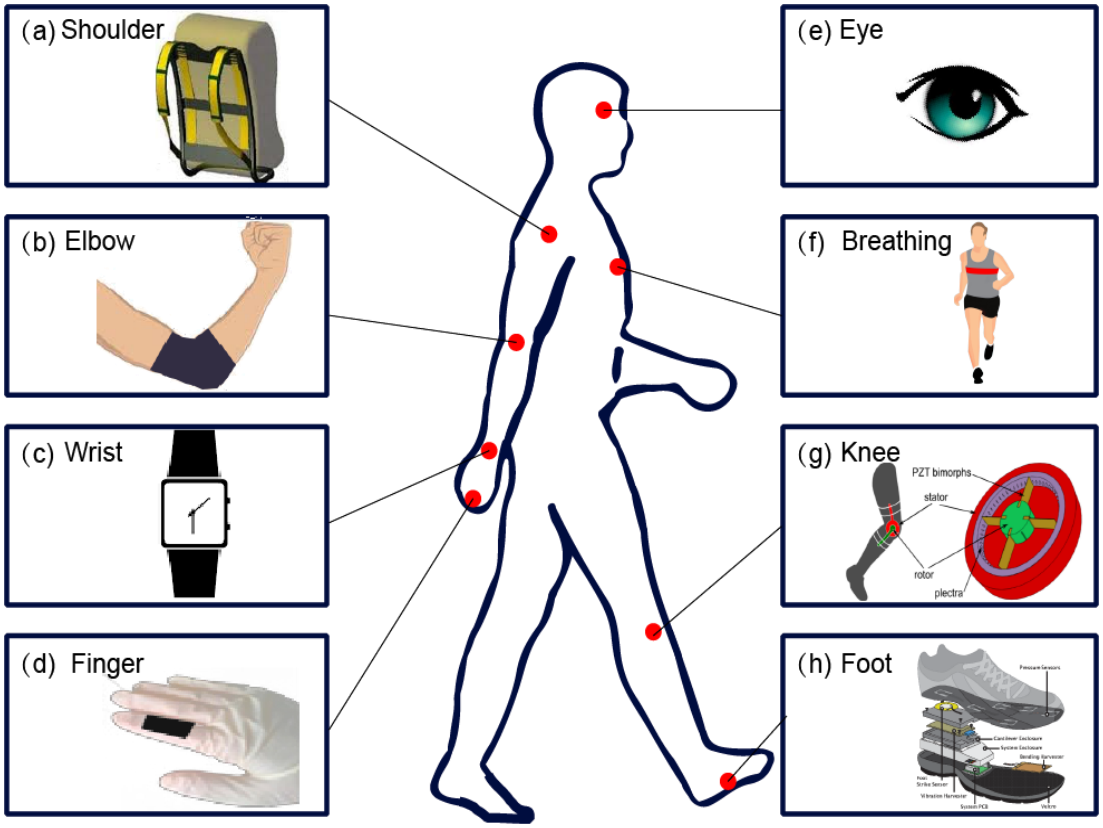

Figure 2.3 Various piezoelectric energy harvesting techniques from different locations on the human body including (a) The shoulder [53], (b) Elbows, (c) The wrist, (d) Fingers [54], (e) Eyes, (f) Chest, (g) Knees [55], and (h) Feet [56].

$$\begin{bmatrix} D_1 \\ D_2 \\ D_3 \end{bmatrix} = \begin{bmatrix} d_{11} & d_{12} & d_{13} & d_{14} & d_{15} & d_{16} \\ d_{21} & d_{22} & d_{23} & d_{24} & d_{25} & d_{26} \\ d_{31} & d_{32} & d_{33} & d_{34} & d_{35} & d_{36} \end{bmatrix} \begin{bmatrix} T_1 \\ T_2 \\ T_3 \\ T_4 \\ T_5 \\ T_6 \end{bmatrix} + \begin{bmatrix} \varepsilon_{11}^T & \varepsilon_{12}^T & \varepsilon_{13}^T \\ \varepsilon_{21}^T & \varepsilon_{22}^T & \varepsilon_{23}^T \\ \varepsilon_{31}^T & \varepsilon_{32}^T & \varepsilon_{33}^T \end{bmatrix} \begin{bmatrix} E_1 \\ E_2 \\ E_3 \end{bmatrix} \quad (2.4)$$

where subscripts 1, 2 and 3 present x, y and z directions in the cartesian coordinate system, and subscripts 4,5 and 6 indicate the rotational stress and strains along the x, y and z directions. There are two general modes 33 and 31 of piezoelectric materials. The first number (3) means the voltage generated along the Z-axis for both modes. The electrodes are attached to the top and bottom sides of the piezoelectric material.

The second number indicates the direction of the applied force. In 33 mode (Figure 2.4(b)), the applied pressure is the same direction as the generated voltage, while 31 mode (Figure 2.4(a)) shows the force is applied along the x-axis.

According to the literature [57], there are three major steps associated with the piezoelectric sensor in an electromechanical system, as shown in Figure 2.4(c):

(i) Mechanical-mechanical transfer, which includes mechanical stability and mechanical impedance matching.

(ii) Mechanical-electrical transfer, which includes electromechanical coupling in a piezoelectric element. Electromechanical coupling is an important factor, where high coupling means a large amount of mechanical energy can be converted into useful electricity.

(iii) Electrical-electrical transfer, which includes electrical impedance matching.

In the second phase, part of the mechanical force through the piezoelectric transducer is converted into electrical output due to electromechanical coupling. The induced voltage in this transducer can be determined using:

$$V = \frac{gFt}{A} \tag{2.5}$$

where g is the piezoelectric voltage constant, F is the applied force, t is the thickness of the piezoelectric transducer, and A is the area of the surface [58].

The phenomenon of piezoelectricity occurs in naturally occurring single crystals such as quartz (SiO2), Lithium Niobate (LiNbO3) and Lithium Tantalate (LiTaO3). Moreover, it also occurs in polycrystalline ceramics such as Barium Titanate

(BaTiO3), PZT [Pb (Zr1–xTix) O3)] and Potassium Niobate (KNbO3), polymers such as PVDF, PLA and piezo-composites.

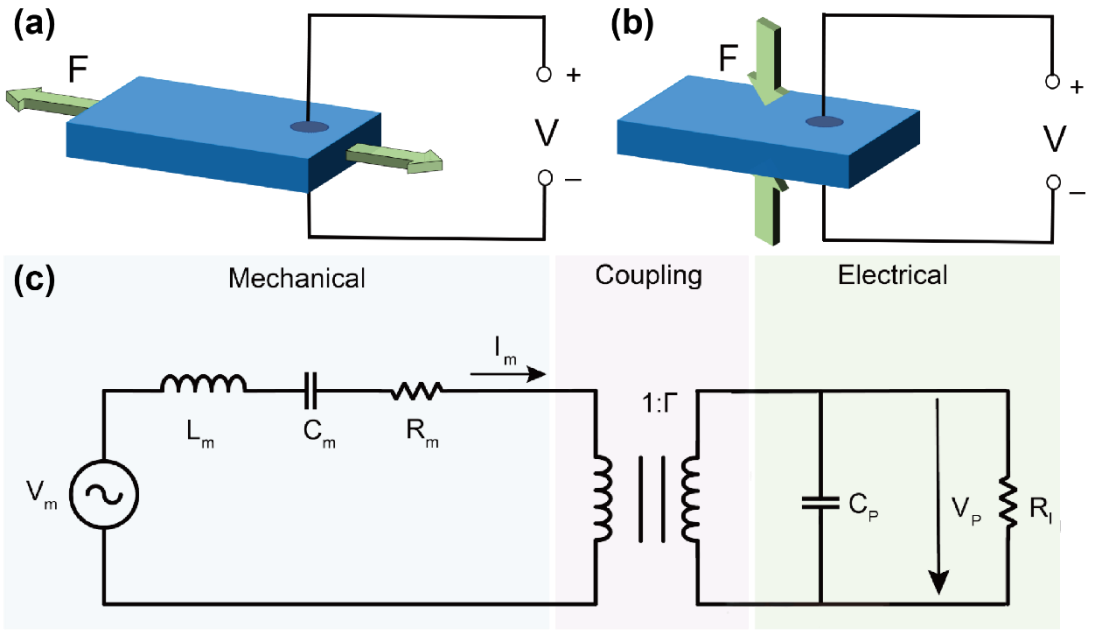

Figure 2.4 Piezoelectric material operated in (a) 31 mode, and (b) 33 mode. (c) Electromechanical equivalent circuit of the piezoelectric sensor.

- **Ceramics**

It is noteworthy to mention that the materials used during the fabrication of piezoelectric sensors have evolved tremendously since World War II [59]. Desirable material properties and characteristics for wearable applications include high flexibility, high time stability, high insulation resistivity and low cost of production [59]. Ceramic materials today are more economical and can be fabricated to achieve high, consistent and reliable performance for a variety of applications. PZT is the most well-known piezoceramic material based on solid solutions of PbZrO3 (PZ) and

PbTiO3 (PT) [59]. Due to their excellent piezoelectric properties and wide commercial availability, PZT ceramics are preferred materials to detect human motions. For example, PZT sensors were used to monitor gait patterns [60], hand gestures [61] and atrial pulse [62].

- **Polymers**

Piezopolymers are also attracting plenty of interest due to their desirable properties in flexible piezoelectric generators. The typical commercial piezoelectric polymer of choice is PVDF, which was discovered by Kawai and Kureha in 1969 [62]. PVDF is made from long chains of the repeating monomer (-CH2 -CF2 -), and it has small permittivity, leading to a high piezoelectric voltage constant g [83]. The piezoelectric charge coefficient of poled PVDF thin film is 6–7 pC/N, which is higher than quartz crystals, but much lower than for PZT ceramics [62, 82]. Due to their mechanical flexibility, it could be produced as a very thin film and attached to a curved structure. Additionally, PVDF sheets possess the ideal characteristics to be easily formed into the desired shape of a wearable device and are therefore suitable for pressure/stress sensor applications [62].

For example, a device was consisted of two curved piezoelectric sensors connected back-to-back [63]. Each sensor comprised a curved PI substrate and two PVDF piezoelectric films arranged in a sandwich structure. The output voltage of the curved piezoelectric sensor, with all PVDF films connected in parallel, was measured to be up to around 155 V for finger tapping motions. A single layer of the curved piezoelectric device can be attached on the watch strap to detect various wrist motions. It was recorded that most wrist motions could generate output voltages in excess of 5

V. The superior performance of the curved piezoelectric device made it possible to monitor human activities and body movements.

- **Composite**

The piezoelectric nanocomposite-based sensor has gained more attention in wearable applications. Piezoelectric-based composites were first proposed in 1972 [62]. The composite was made by hot rolling PZT powder and PVDF, which resulted in both high piezoelectricity and high flexibility. To combine the advantages of both constituent materials, the improvement method involved mixing the ceramic particles into the polymer. In order to obtain ideal piezoelectric properties for these composite materials, many researchers have investigated variations in parameters such as ceramic content and particle size, shape and configurations.

A study focused on BaTiO3 nanowires through a comparably simple hydrothermal method embedded into a P(VDF-TrFE) matrix, forming a piezoelectric-hybrid nanocomposite [64]. The ability of the device to monitor human activities was then examined by attaching a patch-design device to the back of the hand. The maximum output voltage was approximately 8 V for grabbing and releasing motions. The composite film combined the advantages of both ceramics and polymers, exhibiting higher piezoelectric potential and larger local deformation. For example, the T-ZnO/PVDF composite film was able to bend at 30◦, 45◦, 60◦ and 90◦ angle, and the output piezoelectric voltage of the piezoelectric sensor was 0.02, 0.03, 0.06 and 0.16 V, respectively, so that the composite can be used to detect finger bending [65]. Moreover, a bio-compatible piezocomposite film without additional structures was adopted to monitor the biomechanical movements [66]. An energy source

0.5(Ba0.7Ca0.3)TiO3–0.5Ba(Zr0.2Ti0.8)O3 (BCTZ) and a filler material AgNWs were blended with a PDMS matrix to produce a flexible lead-free piezoelectric nanocomposite. The device was proven to monitor different human articular motions, for instance, wrist and elbow bending motions.

Table 2.2 State-of-the-art flexible piezoelectric sensor for human motion.

Material	Structure	Output Voltage	Place	Motion	Ref
Ceramics					
PZT	Sliding track	40 V	Hand	Scratching	[67]
PZT	Sliding track	5.05 V	Hand	Hand shaking	[68]
AlN	Stacked	0.7 V	Finger	Bending	[69]
PZT	Film	0.6 V	Wrist	Hand gestures	[70]
Polymer					
PVDF	Film	2 V	Finger	Clicking	[71]
PVDF	Curved	3 - 25 V	Wrist	Wrist twisting, wrist bending, elbow pivoting, running, tapping the watch, and grabbing	[63]
PVDF nanofiber	Stacked	4.7 V	Wrist	Palm impacting	[72]

Composite					
ZnO nanowire + PVDF	Film	0.33 V	Finger	Folding	[73]
BaTiO3+ P(VDF-TrFE)	Film	8 V	Back of hand	Grabbing and releasing	[64]
PZNN-PLZT	Cantilever	5 - 40V	Wrist	Slamming on table, shaking, cooking, running, walking, walking with hand hitting the body, typing on keyboard, hand clapping, jumping, gesticulating	[74]
BCTZ/AgNW+PDMS	Film	10 V	Wrist, elbow	Wrist bending, elbow bending	[66]

2.1.3 Other Sensing Techniques

- **Triboelectric Sensor**

  Triboelectrification is a well-known phenomenon that is the combined effect of contact electrification and electrostatic induction [75]. When two friction layers are in contact, induced electrical charges appear on the surfaces by contact rubbed motions, including sliding movement, vertical touch, and torsional stress. After separation, some charges tend to lose electrons, while others tend to retain excess electrons, which may generate triboelectric charges on the material's surface. These triboelectric charges produce an electrostatic field that could drive the electrons to flow from the external circuit [76, 77]. According to this effect, Wang's group first proposed the triboelectric sensor in 2012 [78]. Since then, triboelectric sensors have experienced very rapid development and have provided

a new approach to pressure sensing techniques [79, 80].

According to different working scenarios, triboelectric sensors are subdivided into four working modes: vertical contact-separation mode, contact-sliding mode, single electrode mode and freestanding triboelectric layer mode, as illustrated in Figure 2.5. Due to simple structure, wide material choice, and fast dynamic response, triboelectric-based wearable sensors are increasingly employed for human motion tracking and human-machine interfaces. For example, a smart triboelectric band looped around human body parts to track human mobility and recognize individual's identity [81]. The flexible band was designed by a rubber tube that was filled with physiological saline. Based on the coupling of triboelectrification and electrostatic effect, the band successfully recognized six types of human motion, including swallowing, calf raising, jumping, squatting, breathing, and bicep curling, which inspired new thoughts in the human-machine interface.

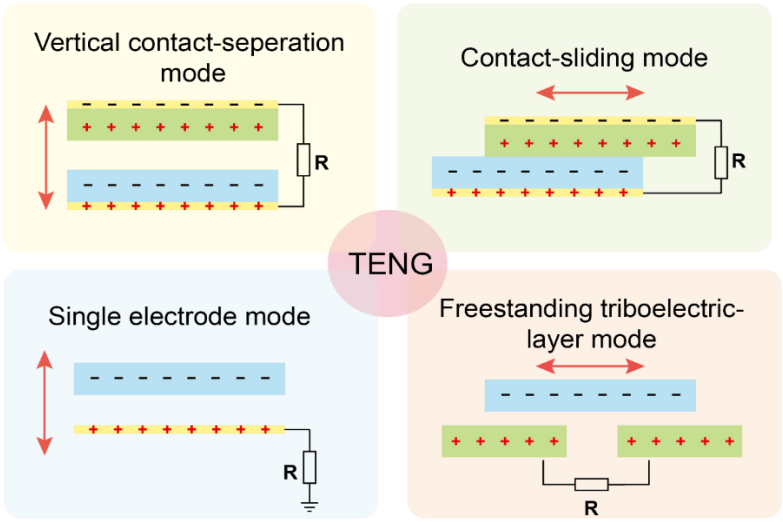

Figure 2.5 Four working modes of triboelectric effect-based electronics.

- **Capacitive sensor**

Capacitive sensors are non-contact devices that the capacitance changes under external stimulation. A common capacitive sensor acts as a simple capacitor, which usually consists of an insulating dielectric layer sandwiched between a pair of conductive electrodes. The equation for the capacitance is as follows [82]:

$$C = \frac{\varepsilon A}{d} \tag{2.6}$$

where d represents the distance between the conductive electrodes, A is the overlapping area of two electrodes, and ε is the permittivity of the dielectric material. When the external force is applied to the plates, the distance of the plates or the electrode area will change, resulting in the capacitance variation of the sensor.

The main advantages of capacitive sensors are good stability, high measurement accuracy, simple structure and better temperature tolerance than resistive sensors. To date, much research has developed new types of flexible capacitive sensors to meet the requirements of wearable devices. For example, a flexible capacitive device was constructed by the micropatterned PDMS/Au electrodes duplicated from the lotus leaf coupled with PS microspheres as the dielectric layer [83]. The capacitive changes of the device are caused by enlarging the relative plate area, reducing distance, and rearranging dielectric materials after compression. Taking advantage of unique structures, the proposed devices present high sensitivity (0.815 kPa^{-1}), wide dynamic response range (from 0 to 50 N), and fast response time (≈38 ms), which indicted its potential applications in electronic skins, wearable robotics, and biomedical devices.

2.1.4 Comparison Between Different Types of Pressure Sensors

Different pressure sensing mechanisms have been used for wearable electronics. In particular, pressure sensors can be divided into four categories: piezoresistive, capacitive, piezoelectric and triboelectric, and their advantages and disadvantages are shown in Table 2.3.

Piezoresistive sensors are widely used in wearable sensing systems due to the high sensitivity, simple construction, simple readout circuits and robustness of both static and dynamic pressure. However, the output of piezoresistive sensors is easily affected by external environmental conditions like temperature, and the response/recovery times are relatively slow. Capacitive sensors process good stability, high measurement accuracy and better temperature tolerance than piezoresistive sensors, but the crosstalk between sensing units is the typical limitation of capacitive sensors.

Piezoelectric sensors and triboelectric sensors are self-powered sensors that can directly convert mechanical force into electrical signals without external power supply, and always have fast response time and more sensitive to dynamic stimuli. However, they require a specifically designed readout circuit. In comparison with piezoelectric sensors, triboelectric sensors produce larger output voltages and wider material choices. Furthermore, triboelectric sensors in the early research stage, there are still some fundamental understanding and technology problems that need to be studied, such as choice of materials, power management, durability, and stability [77].

In this thesis, piezoelectric sensors and piezoresistive sensors are chosen to detect the

human activities, including finger motions, hand gestures and throat movements. These human activities generate small tendon movements around the wrist or slight muscle motion of the throat. Typical capacitive sensors are composed of a dielectric layer sandwiched between two electrodes, whose thickness varies upon pressure, and triboelectric sensors are based on contact-separation mode, which require a gap between two electrode layers. When compared with piezoelectric sensors and piezoresistive sensors, the capacitive sensors and triboelectric sensors are more suitable for joint bending detection [84, 85] and tactile sensing [86, 87] based on their working principle.

Therefore, piezoelectric sensors were chosen to recognize the finger tapping motions in Chapter 3, as the sensors are sensitive to the dynamic stimuli and responds quickly. However, piezoelectric sensors will miss the static information when detecting the hand gestures and throat movements. So piezoresistive sensors were used in Chapter 4 and 5 to capture both static and dynamic information.

Table 2.3 Comparison of the typical features of wearable pressure sensors.

Types	**Piezoresistive**	**Piezoelectric**	**Triboelectric**	**Capacitive**
Working mechanisms	Convert mechanical force into changes in resistance	Convert mechanical force into electric signals by the internal electrical dipoles charges	Convert mechanical force into electrical signals through a conjunction of the triboelectric effect and electrostatic induction	Convert mechanical force into changes in capacitance

Advantages	High sensitivity, simple construction, simple readout circuits, robustness of both static and dynamic pressure	High sensitivity, fast response/recover time, self-powered ability, good stability	High output voltage, fast response/recover time self-powered ability, simple fabrication, low sensing limitation	Good stability, high measurement accuracy, fast response time
Disadvantages	Poor stability, temperature-dependent, low response time	Low output voltage, high matched impedance	Susceptible to environmental influences, low output current, high matched impedance	Relative complex structure, crosstalk between sensing units

2.2 Review of Classification Methods

Wearable sensing systems have rapidly developed in recent years. Researchers and scientists have made great efforts on new structures and materials to improve the sensitivity, flexibility, durability and stability of the pressure sensors, which are used to detect human motions. The collected data from sensors contain rich valuable information, including muscle movements [88], body temperature [89, 90], sweat detection [91] and other physiological parameters [92] . Therefore, ML algorithms are used to accurately analyse and classify the sensing data. In the next sections, conventional classifiers and deep learning models are introduced. Next, state-of-the-art pressure sensors for human motion recognition using ML algorithms are discussed.

2.2.1 Conventional Classifiers

- **K Nearest Neighbour**

K Nearest Neighbour (KNN) is a non-parametric classification method based on the supervised learning technique. For an unlabelled sample, its nearest neighbours *k* samples in the dataset, the majority vote of these *k* samples is usually used to decide the classification for the unlabelled sample with or without consideration of distance-based weighting, as illustrated in Figure 2.6. The squares and triangles in the figure are labelled data, representing different labels. The black circle is data to be classified. If *k*=5, then there are 3 triangles and 2 squares closest to the circle. These 5 points vote, and the proportion of triangles accounts for 3/5, so the circle to be classified belongs to the triangle category. However, if *k*=10, then the circle is classified into square group as 6 squares are closest to the circle.

The Euclidean distance is the most commonly used distance metric in KNN. It measures the true straight-line distance between two points in Euclidean space, as shown in the equation:

$$d(x, y) = \sqrt{\sum_{i=1}^{n} (x_i - y_i)^2} \tag{2.7}$$

KNN classification is a simple but effective method for human motion classification. In [93], the KNN algorithm successfully identified 10 American Sign Languages with 97.86% accuracy by attaching stretchable strain sensors to the finger joints. Besides, an insole sheet integrated with force sensors was able to classify different gait phases by the KNN algorithm [94].

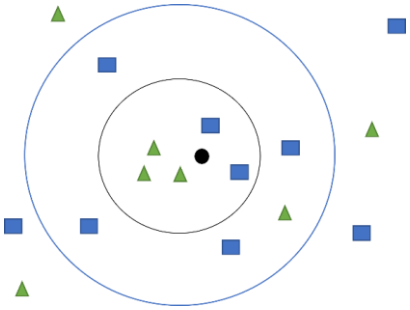

Figure 2.6 Architecture of K nearest neighbour algorithm.

- **Decision Tree**

Decision Tree (DT) is a flowchart-like structure where each internal node represents a "test" on an attribute, each branch represents the results of the test, and each leaf node represents a classification label, as indicated in Figure 2.7. As can be seen from the figure, the decision tree starts from the root node, which does not have any incoming branches. The outgoing branches of the root node then feed the internal nodes. Both types of nodes perform evaluation based on available capabilities to form homogeneous subsets, which are represented by leaf nodes. Leaf nodes represent all possible outcomes within the dataset. DT is also a common method used to recognize human activities. For example, a flexible piezoresistive pressure foam was taped on the second knuckle of each finger to distinguish Arabic numeral gestures combined with the DT classifier [95]. Moreover, the DT classifier is also used to recognize different ambulatory activities by smart shoes [96, 97].

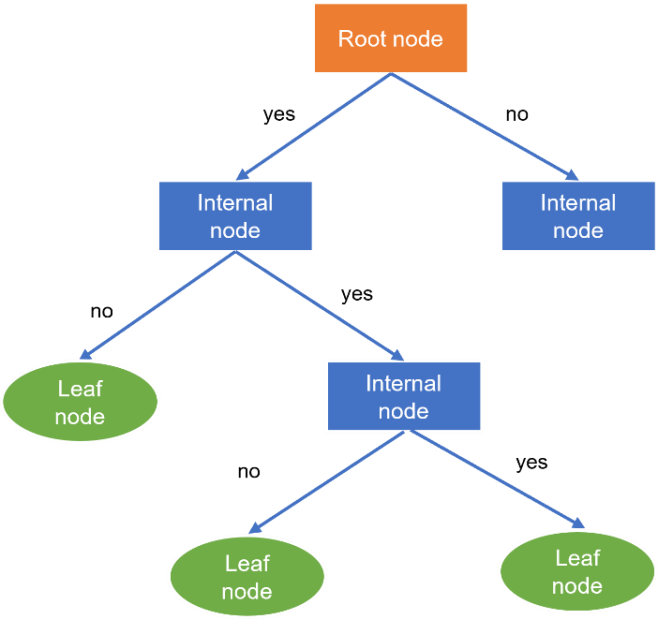

Figure 2.7 Architecture of decision tree.

- **Linear Discrimination Analysis**

Linear Discrimination Analysis (LDA) is a tool for classification, dimensionality reduction and data visualization [98]. The intuition behind the method is to project the training samples onto a straight line so that the projection points of similar samples are closed, and the projection points of different samples are far away. When classifying new samples, project them onto the same straight line, the category of the new sample is determined according to the position of the projected point. LDA can be used as the classifier for the purpose of hand gesture recognition. Combined with the machine-learning algorithm of the LDA model, the wristband constructed with piezoelectric sensors and triboelectric sensors was achieved letter-by-letter recognition of sign language actions, with a maximum recognition accuracy of 92.6% [99].

- **Support Vector Machine**

Support Vector Machine (SVM) is a learning algorithm based on the optimization theory that is derived from statistical learning theory. An optimal decision hyperplane is established to maximize the distance between the two types of samples on the two sides of the plane that are closest to the plane, thus providing a good generalization ability for the classification problem. For a multi-dimensional sample set, the system randomly generates a hyperplane and moves continuously to classify the samples until the sample points belonging to different categories in the training sample are located on both sides of the hyperplane. There may be many hyperplanes that satisfy the condition. SVM officially finds such a hyperplane while ensuring classification accuracy, maximizing the white space on both sides of the hyperplane, thus achieving optimal classification of linear separable samples.

In terms of a non-neural network-based classifier, SVM is one of the best choices for human activity recognition when the data size is relatively small. For example, a wristband with five capacitive sensors was able to recognize hand gestures in real-time with the SVM algorithm [100]. Moreover, Chengkuo Lee's group has developed a series of artificial devices based on pressure sensors combined with ML algorithms to recognize different human motions and interact with VR applications. In a recent article, tactile rings were developed that allow finger motion detection and object recognition based on triboelectric sensor via SVM analysis [101].

2.2.2 Deep Learning Model

- **Artificial Neural Network**

Artificial Neural Network (ANN) is a mathematical model that mimics the structure and function of biological neural networks. ANN is computed by connecting a large number of artificial neurons, and it consists of three types of processing layers: input layer, hidden layer and output layer. There can be one or multiple hidden layers where processing happens in them. The hidden layer refines the input by removing redundant information and sends the information to the next hidden layer for further processing, and computes the output based on the adjustable "weights". A variety of tasks use artificial neural networks for pattern recognition [102], material identification [103] as well as human motion recognition [104].

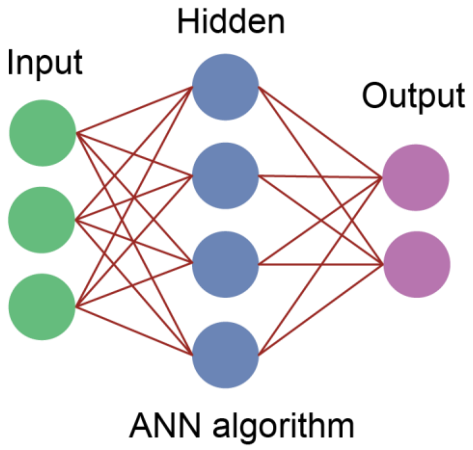

Figure 2.8 Architecture of artificial neural network.

- **Convolutional Neural Network**

Another popular architecture for deep learning is Convolutional Neural Network

(CNN), which mainly used for visual data processing such as images and videos. CNN also consists of three different types of layers: convolutional layer, pooling layer, and fully connected layers. The convolution layers focus on learning significant features that may appear in the data with the help of filters/kernels whose coefficients are tuned during the training phase. The pooling layers reduce the dimensionality of feature maps and also introduce some degree of translation invariance in the network. The convolutional and pooling layer forms the features extraction pipeline of the network which detects local features in the input. The fully connected layers then combine the local features to obtain global features. In [105, 106], CNNs were applied for hand gesture recognition and object identity with different types of wearable sensors. Also, CNNs were popular in speech recognition [107] and gait phases [108].

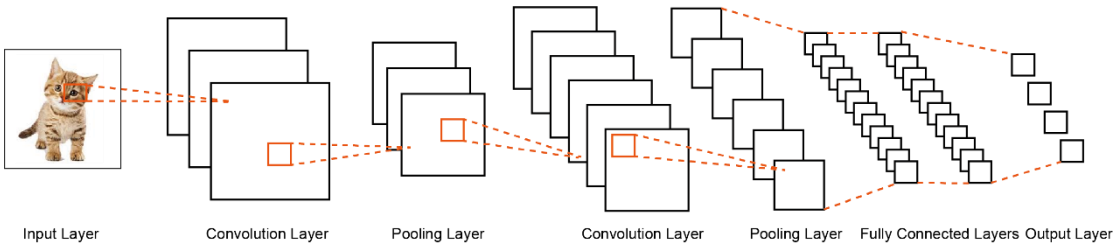

Figure 2.9 Architecture of convolutional neural network.

- **Recurrent Neural Network**

A new type of architectures was developed to detect patterns in time series data was known as Recurrent Neural Network (RNN). Each unit in RNN contains recurrent connections so that the network can retain information for a longer period of time, which enables RNNs to recognize patterns in sequential data such as speech, video, and text. The architecture of the RNN is shown in Figure 2.10, where "x_t" is the input layer, "A" is the hidden layer, and "h_t" is the output layer. At any given time t, the

current input is a combination of input at x_t and x_{t-1}. The output at any given time is fetched back to the network to improve on the output. A more advanced form of RNN is known as Long Short-Term Memory (LSTM) which improves the pattern recognition capabilities of RNN.

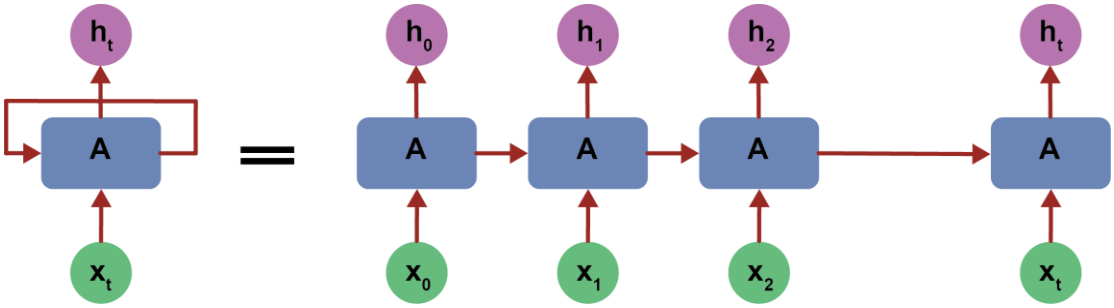

Figure 2.10 Architecture of recurrent neural network.

Table 2.4 State-of-the-art pressure sensor for human motions with ML algorithm.

Sensor	Classifier	Motion	Number of sensors	Number of participants	Accuracy	Ref
Strain sensors	LDA KNN SVM	10 Hand gestures	5	6	97.8 ± 2.3%, 97.9 ± 1.7%, 97.9 ± 1.7%	[93]
FSR	KNN	7 Gait phases	5	5	81.43%	[94]
Piezoresistive sensor	DT	10 Hand gestures	5	2	98.9%	[95]

Triboelectric sensor	SVM	14 Hand gestures	5	N/A	99.821%	[101]
Triboelectric sensor + piezoelectric sensor	LDA	26 hand gestures	8	N/A	92.6%	[99]
Piezoresistive sensor	SVM	5 hand gestures	6	1	97%	[61]
Capacitive sensor	SVM	3 hand gestures	5	1	90%	[100]
Triboelectric sensor	ANN	gait phase	2	5	98.4%	[104]
Triboelectric sensor	CNN	50 hand gestures	15	N/A	91.3%	[105]
Triboelectric sensor	CNN	5 gait phases	3	1	96.67%	[108]
Triboelectric sensor	RNN	20 Lip motions	2	1	94.5%	[109]

2.3 Summary

This chapter summarises the recent progress in wearable pressure sensing techniques

over the past few years. Pressure sensors can be divided into four categories based on their working principle. Piezoresistive and capacitive sensors are none self-powered sensors which require the external power supply to provide bias voltage. Compared with capacitive sensors, piezoresistive sensors are widely used in wearable devices due to their simple structure, simple readout circuit and wide detection range. Besides, piezoelectric and triboelectric sensors are self-powered sensors which can directly convert mechanical force into electric signals without any external input. Piezoelectric sensors are suitable for detecting small-scale motions because of their simple structure, fast response time, high sensitivity and good stability. The advantages and disadvantages of the four sensing techniques are discussed in this chapter. Meantime, the state-of-art using pressure sensors to detect human motion are also summarized in the context.

Besides the advancement in pressure sensing techniques, wearable devices have made great progress with the help of machine learning algorithms to process the data and make decisions. Recent advances in human motion recognition are summarized in this chapter. The ML algorithm-assisted wearable systems are able to accurately predict and classify the collected data. Therefore, the combination of pressure sensors and ML algorithms enhances the intelligence of pressure-sensing systems. Different machine-learning algorithms are introduced in this chapter, and the recent progress in machine-learning-assisted systems for human motion recognition has been discussed.

Chapter 3

Piezoelectric Sensor for Finger Motions

Finger gestures are important nonverbal communication for conveying information through visual perception. With the burgeoning demand for interfaces that enable humans to seamlessly interact with machines, gesture recognition systems have been fast developed, including telerobotic surgery [110], virtual reality [111, 112], health rehabilitation and human-robot collaboration [113]. Many techniques have been developed to detect finger motions. There are four main technologies for finger motion recognition, which are based on cameras, accelerometers (ACC), EMG and pressure sensors.

Camera-based technologies directly capture the gesture video or picture information, followed by processing the depth images of the pixel point to the lens distance [114]. High accuracy, efficiency and robustness make it become a commonly used method in human-computer interaction applications. In [115], CNN algorithm achieved the high accuracy of 91.41% to recognize sign language of MNIST dataset. However,

limitations related to viewing angle, sensitivity to lighting conditions and noisy background restrict application scenarios in which cameras can be used [116].

As for ACC-based technology, it is comfortable to wear without disturbing natural hand gestures, and it could provide rich information about hand movements. However, the drawback of the accelerometer-based method is that the detected signal is mixed, and it is always challenging to identify the performance of individual sensor setups. Thus, they cannot receive a separate signal from the palm and finger movements simultaneously [117].

In contrast to other solutions for hand gesture recognition, EMG-based technology provides an important opportunity to achieve natural human-computer interaction by directly sensing and decoding subtle muscle activities [118]. Due to the small electrodes attached to the arm, any subtle wearing position change will strongly influence the accuracy [119]. Meantime, signal and noise will be synchronously collected so that it will increase the complexity of signal processing and analysis.

Pressure-based finger motion recognition has recently attracted increased attention. Gloves [120-122], armbands [123-125], and wristbands [99, 126] become the main applications for collecting the pressure signal for hand gestures. The smart gloves require sensors attached to the knuckles of the fingers which are cumbersome and interfere with normal activities. Armbands are required a large number of sensors based on the EMG method. For example, 64 electrodes were attached to the forearm to detect flexion and extension of different finger degrees of freedom [127]. Compared with gloves and armbands, wristbands reduce the number of sensors to recognize gestures in a more comfortable way.

Piezoelectric sensors are sensitive to the dynamic motion base on the piezoelectric effect, as illustrated in chapter 2.1.2. When attaching the piezoelectric sensors to the wrist skin, the response of the sensors can be used to detect the finger motions. In this case, a wristband based on piezoelectric sensors was developed to achieve the finger motion recognition.

Figure 3.1 shows the basic functions of the wristband system. The bracelet device is designed to recognize finger motions. Piezoelectric sensors convert mechanical pressure to electrical signals. These transducers sense tendon movements around the wrist. The active signals are processed through the signal conditioning circuit to amplify the signals and remove the noise. The useful information is transmitted to microcontroller (Arduino UNO) and then transmitted to the computer terminals. The wristband was able to achieve finger gesture recognition with different ML algorithms.

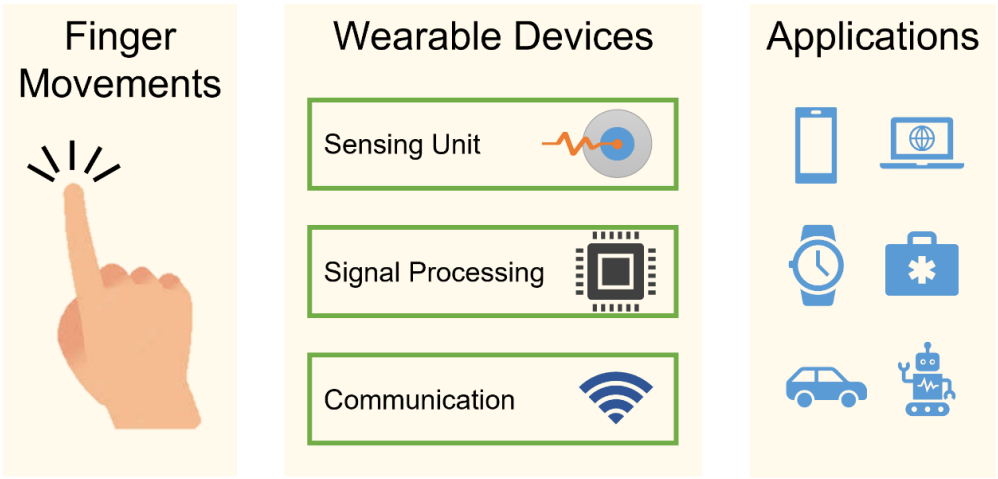

Figure 3.1 Building block of a typical wearable device.

3.1 Experimental Setup and Data Collection

Herein, a piezoelectric wristband with an array of 6 PZT ceramic disks (AB1290B-

LW100-R) was used to distinguish different finger motions. The photograph of PZT ceramic disks and the wristband are shown in Figure 3.2.

Piezoelectric sensors generate electrical signals in response to tendon movements around wrist. However, finger movements generate small tendon movements, the sensors output needs a moderate amount of amplification so that the desired signal levels are in the 5 V range for full scale to fit the microcontroller analog-to-digital converter ports. Thus, the charge amplifier is configured to serve the dual purpose of conversion to voltage as well as amplification. Herein, a charge mode amplifier circuit was used to buffer and amplify the piezoelectric sensor. The charge mode amplifier circuit is made of several components: a current source, a piezoelectric sensor resistance and a piezoelectric sensor capacitance are acted as piezoelectric sensor model, an input resistance (Ri =6 KΩ), a feedback resistor (Rf =100 MΩ), a feedback capacitor (Cf=15nF) and a bias voltage (1/2 Vcc=2.5V). The circuit diagram and the frequency response are provided in Figure 3.3.

Figure 3.2 Photograph of the piezoelectric sensors and the wristband.

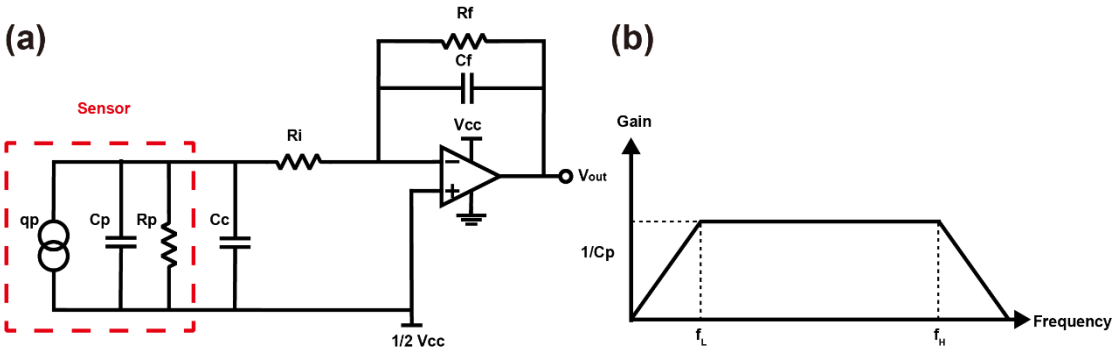

Figure 3.3 (a) Schematic of signal conditioning circuit for piezoelectric sensor. (b) Frequency response plot of the charge mode amplifier circuit.

The response signal of a piezoelectric sensor based on wrist muscle extraction induces a very small charge. The charge amplifier used in the proposed work is an operational amplifier configured as an integrator, where the circuit's output is given by:

$$Vo = -\frac{qp}{Cf} + \frac{Vcc}{2} \tag{3.1}$$

where Vo is the output voltage, qp is the charge source, Cf is feedback capacitance and 1/2 Vcc is the bias voltage that was added to the ground of the piezoelectric sensor. Meantime, the signal conditional circuit is also analogous to a first-order high-pass RC filter when the feedback resistor and capacitor are placed in parallel across the input and output of the operational amplifier, where the lower cutoff frequency is calculated by:

$$f_L = \frac{1}{2\pi RfCf} \tag{3.2}$$

Besides, the readout circuit also acts as a low-pass filter, where the higher corner cutoff frequency is derived by:

$$f_H = \frac{1}{2\pi Ri(Cp+Cc)} \tag{3.3}$$

The signal conditioning circuit was designed to amplify the piezoelectric signals in the 0-5 V range and filter the undesired signals. As mentioned previously, human motion often occurs around 1Hz. Therefore, we chose a 100 MΩ feedback resistor Rf and a 10 nF feedback capacitor Cf to build the high-pass filter. At the same time, the low pass filter also eliminates noise from the human body and environment. Hence, a 6 kΩ resistor was chosen as the input resistance Ri. Piezoelectric sensors generate both positive and negative signals when pressing and releasing the pressure. Therefore, 1/2 Vcc (2.5 V) was added to the ground of the piezoelectric sensor so that the output would swing above and below this DC level. The signal conditioning circuit design and its PCB layout are shown in Figure 3.4.

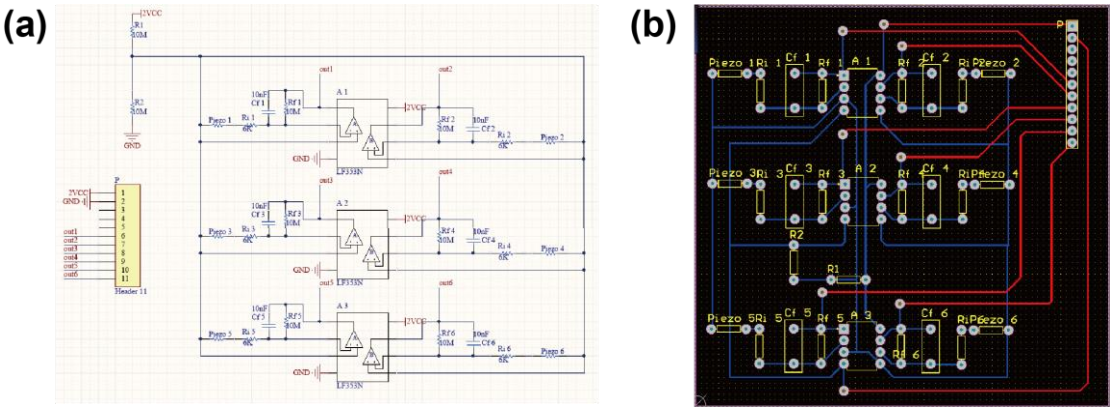

Figure 3.4 (a) The signal conditioning circuit design. (b) PCB layout.

The wristband was put on the left hand of a subject under comfortable tightness without blood restriction, pain and movement limitation. The substrate of the wristband is a soft elastic fastening wire with a Buckle of 3.8 cm width and 41 cm length. Six commercial ceramic disks with 12 mm diameter were chosen in this project since the wrist

circumference of the subject is 152 mm, and 6 disks could fully cover the wrist and get comprehensive muscle contraction information at the underside of the wrist. To ensure the place of sensors is fixed for multiple wearing, they are pasted by hot glue inside of the band.

The subject sat in front of a desk and placed the forearm and elbow in a comfortable position on the desk, and the wrist was raised above the desk to eliminate the external pressure. The total experiment time was 15 minutes. The participant was required to perform the tapping gesture for five fingers. The recording contains three times put on and takes off with around 50 repetitions for each finger. The tapping gesture repeated every two seconds, and the beginning 6 seconds and ending 5 seconds were kept stable. Figure 3.5 shows examples of the collection repetition tapping gesture by the middle finger.

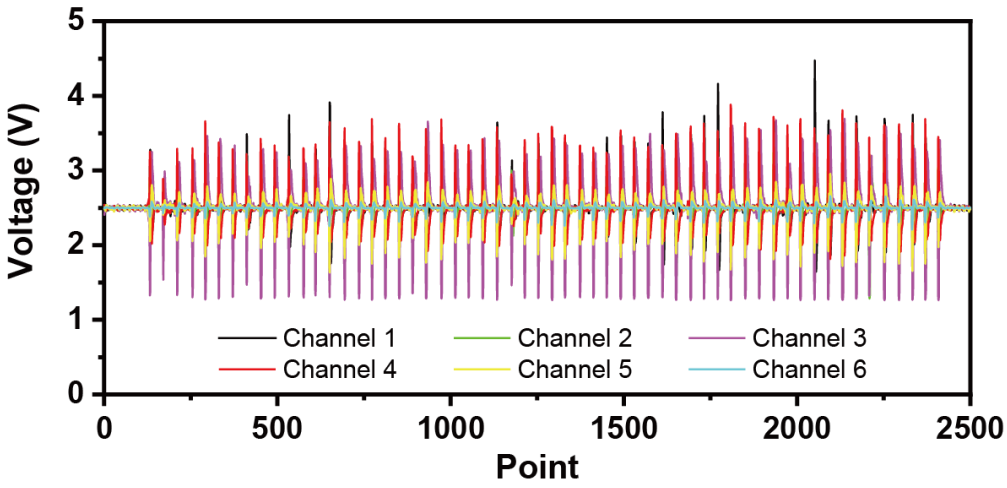

Figure 3.5 Example piezoelectric voltage signal for middle finger tapping.

3.2 Data Processing and Feature Extraction

Piezoelectric sensors convert the pressure from the tendon movement to the voltage reading. The output signals from piezoelectric sensors were connected to the analog to digital input ports of the microcontroller (Arduino UNO based on the ATmega328). Data was collected by MATLAB (2020 version) and stored in the computer for the following offline processing.

The output signal of piezoelectric sensor is usually oscillating between high positive values to negative values, so that there is one noticeable peak generated by a hand motion. Due to this characteristic, 'findpeaks' code is used to detect the local maxima and find their locations of the input vector. To avoid discovered peaks being very close to each other and the same data being intercepted multiple times, restricting the acceptable peak-to-peak separations to values greater than 2s. The whole signal is cut into small segments according to the maxima of different gestures. An example of row signals collected from the piezoelectric sensors for five fingers is shown in Figure 3.6. Every gesture is presented by six channels which are the six sensors. The amplitude of the output voltage ranges from 0 to 5 V.

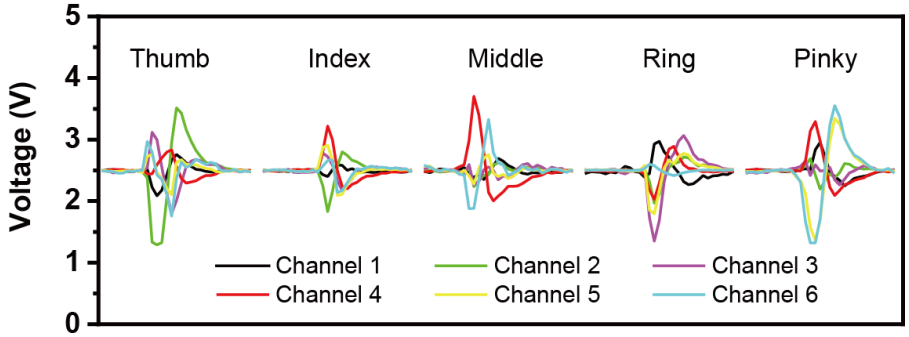

Figure 3.6 Examples of piezoelectric sensor output for five fingers.

ML techniques are widely used for hand gesture recognition (See chapter 2.2). In this chapter, KNN, DT and SVM are chosen to classify the finger motions, as they are good at dealing with the small dataset.

In supervised learning, Polynomial-kernel SVM is first chosen to process the recording values and reconstruct gestures. A kernel function of the 2-polynomial order is used to map the information to a higher dimension. In order to train the SVM classifier, an SVM template was applied in MATLAB to design and build the classifier.

KNN and DT are also commonly used ML algorithms for hand gesture recognition [118]. KNN is classified by measuring the distance (e.g. Euclidean distance) between different eigenvalues. The idea is that if most training points of the k closest in the distance to a query point belong to a certain category, the tested sample also belongs to that category [128]. Therefore, the number of adjacent samples k is the vital parameter in the algorithm. In this chapter, we considered k=7 as the best performance to discriminate between the gestures.

DT classify the new query sample by starting from the root, testing the corresponding feature attributes in the item to be classified, and selecting the output variable according to its value. Eventually, it reaches a leaf, using the category of the leaf as the decision result. A decision tree model was created with two branch nodes and ten observations per leaf. The model was used to train gestures using sample data.

The raw dataset was divided into a 200 samples training set and 75 samples test set. The raw dataset was fed to the three classifiers to recognize different fingers for tapping gestures. The confusion matrixes of KNN, DT and SVM are shown in Figure

3.6, where the SVM algorithm presented the best performance. Figure 3.7(d) shows the clustering result of five fingers realized by T-Distributed Stochastic Neighbour Embedding (t-SNE), and the boundaries between these five categories are clear.

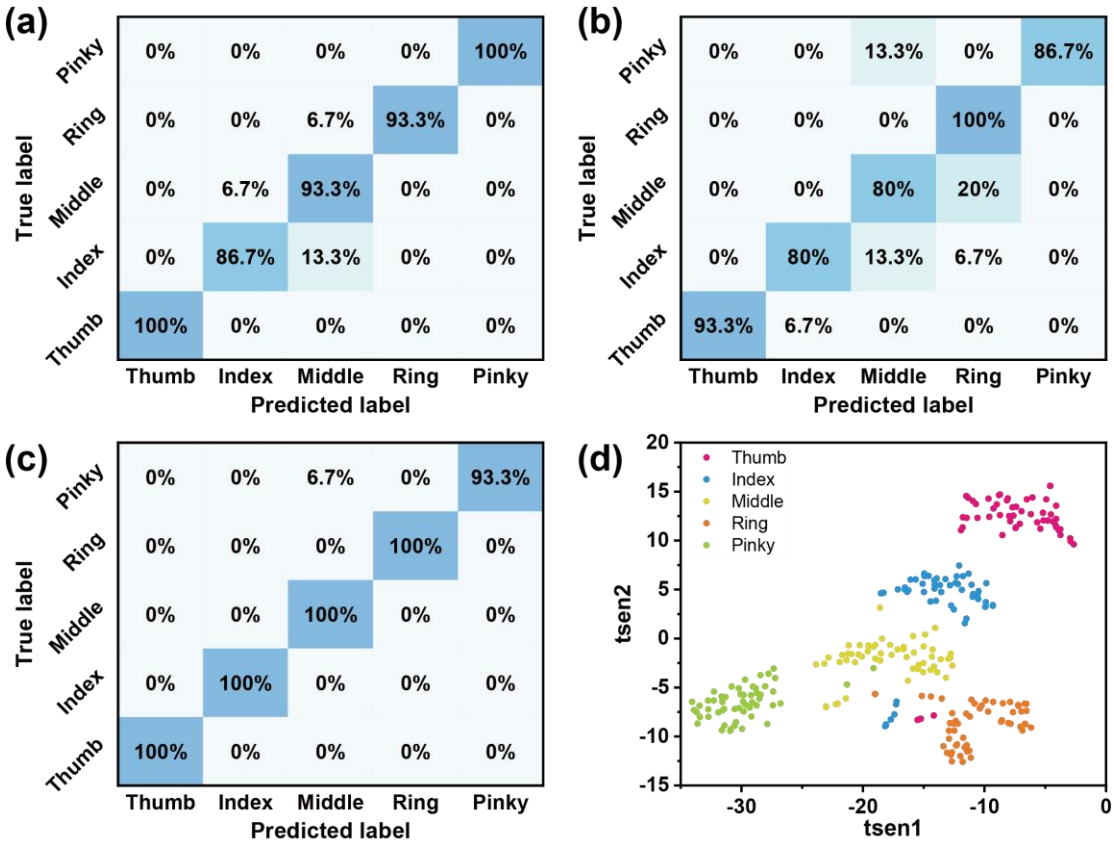

Figure 3.7 Classification confusion matrix for the raw data of five tapping fingers (a) by using KNN algorithm with 94.67% accuracy; (b) by using DT algorithm with 88% accuracy; (c) by using SVM algorithm with 98.67% accuracy. (d) Cluster results for five fingers.

Feature extraction was involved in distinguishing five different finger motions and compared with the original signal to find a better data type for higher classification accuracy. Sixty different features were extracted from piezoelectric sensors, which are summarized in Table 3.1, including the voltage mean, maximum, minimal, peak-to-peak, standard deviation, variance and the location of maximum and minimal value,

which are extracted to evaluate the deviation of the signal, and cross correlation-based features show great potential in classifying activities with significant change on signal magnitude along two dimensions.

Table 3.1 Features extracted from the piezoelectric sensors in time domains.

Feature extraction	**Number**
Mean of the voltage amplitude	6
Maximum of the voltage amplitude	6
Location of maximum amplitude	6
Minimum of the voltage amplitude	6
Location of minimum amplitude	6
Peak-to-peak	6
Mean of the cross-correlation	6
Standard deviation of the voltage amplitude	6
75th percentiles	6
Variance of the voltage amplitude	6

Total number of features	**60**

Table 3.2 shows the result of all three algorithms with original data and feature extraction by using six piezoelectric sensors. SVM dealing with feature extraction dataset was the best choice for tapping gesture recognition with 100% accuracy, which was higher than using the original dataset. While KNN processing feature extraction data has the lowest accuracy with 77.33%, which had a significant decrease than that of the raw dataset. The classification accuracies were low when using the DT algorithm to classify raw data and extracted features. Feature extraction, in this case, failed to increase the accuracy of classification.

Table 3.2 Classification results of different algorithms by using six piezoelectric sensors.

Algorithm	**KNN**	**DT**	**SVM**
Raw data	94.67%	88%	98.67%
Feature extraction	77.33%	81.33%	100%

Furthermore, the number of sensors and their locations were also studied to find the best performance of the classification, as illustrated in Figure 3.8. Sensors at different locations collect tendon movements in different parts of the wrist. When the number and location of sensors are reduced, the effective signals collected from the wrist will decrease, making it challenge to classify the different tapping fingers. The results

indicate that using more sensors exhibited a more accurate classification performance. In practical implementation, the devices prefer to reduce size, weight and cost so that fewer sensor is needed to satisfy the classification requirements. In this figure, two sensors attached to the ulnar styloid of the wrist are already sufficient to classify the present gestures, as the accuracy is over 90%. It is worth noting that the most important place was roughly at the ulnar styloid of the wrist for tapping gestures. Therefore, the future device will be considered to put at least one sensor at the ulnar styloid to make sure classification accuracy.

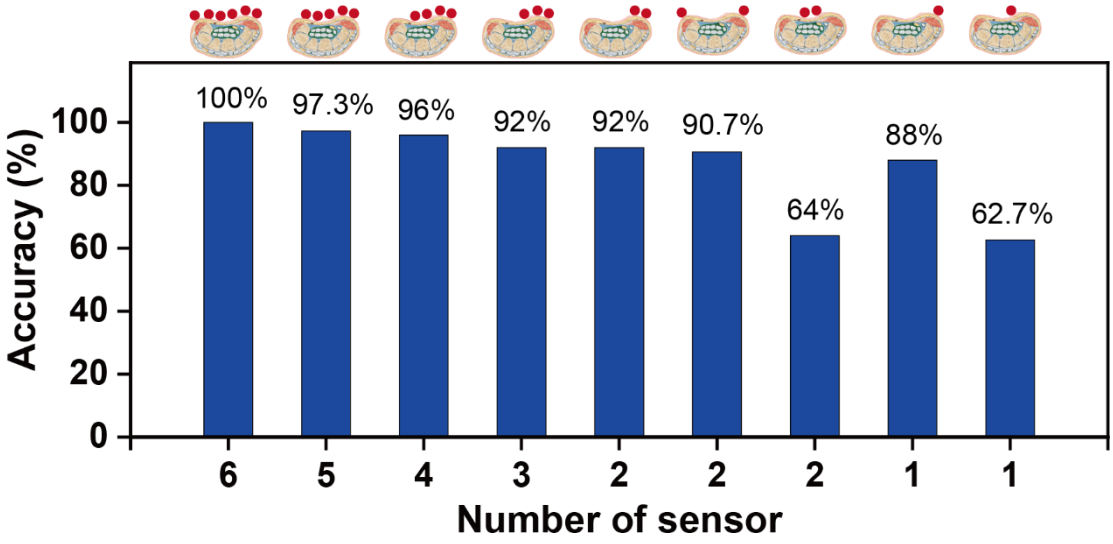

Figure 3.8 Classification accuracy for all five hand gesture using SVM with between 1 and 6 sensors.

3.3 Summary

In this chapter, a wristband with six PZT piezoelectric ceramic disk sensors was used to distinguish tapping gestures for five different fingers. A comparison between three ML algorithms (KNN, DT, and SVM) to classify the fingers with raw data and extracted features are discussed. The SVM algorithm achieved the best performance

with a classification accuracy of 98.35% for raw data and 100% for extracted features. Moreover, the number and place of sensors were also optimized for practical implementation. Two piezoelectric sensors attached to the ulnar styloid of the wrist were sufficient to classify the tapping motion of the different fingers.

Chapter 4

Piezoresistive Sensor for Hand Gesture Recognition

In this last chapter, piezoelectric sensors are used to recognize the finger motions. However, there are some improvements can be used to further increase the accuracy and wearability of the bracelet. First, the commercial piezoelectric sensor is a ceramic disk and not bendable. Thus, it is hard to fully fit to the wrist. Flexible sensors seem more suitable for hand gesture recognition. Secondly, design a more comfortable substrate for the wristband, which could also fix the placement of sensors to ensure each sensor able to capture the same muscle movement for various users so that the input signal is much more reliable for data processing. Finally, piezoelectric sensor was sensitive to dynamic motions, while the information on static gestures was lost. Therefore, piezoresistive sensors can be used to capture both dynamic motions and static gestures.

Piezoresistive sensors, whose resistance can be tuned by the mechanical forces imposed on the surfaces, have been widely investigated and used in gesture recognition due to their excellent sensitivity and continuous detection capabilities [126]. Various piezoresistive materials and structures have been investigated in recent years. It was previously demonstrated that the nano/ micro-geometrical structures yield a greater sensitivity [39, 129-131]. However, these micro-structures are expensive and require complex fabrication procedures. In contrast, the low cost and less complex fabrication processes involving Reduced Graphene Oxide (rGO), which has a two-dimensional nanosheet layer structure, exhibit high conductivity and robust mechanical strength, making it a promising candidate for flexible piezoresistive sensors [25, 132-135]. This chapter proposes a piezoresistive sensor based on a flake-sphere composite configuration in which rGO fragments are doped with PS spheres to achieve both high sensitivity and flexibility. The resistance change under pressure was related to the size and weight ratio of the doping PS sphere. Our flexible rGO/PS sensors achieved 66% resistance change when doped with 2 μm PS spheres. The rGO-based sensor also promises high mechanical durability (1000 times) and fast response time (186 ms), which offers excellent potential in wearable devices.

This chapter proposes a piezoresistive sensor based on a flake-sphere composite configuration in which rGO fragments are doped with PS spheres to achieve both high sensitivity and flexibility. Furthermore, a wearable hand gesture recognition system was developed based on two parts: a flexible piezoresistive wristband that measures the pressure distribution around the wrist, as well as an interface for intelligent gesture classification. The high-performance wristband consisted of an array of five rGO/PS sensors for detecting subtle wrist movement information. In the meantime, the

developed system was successfully demonstrated to realise the recognition of 12 different hand gestures with an accuracy of 96.33% with the help of SVM algorithm. Furthermore, an Human-Machine Interface (HMI) application was also designed to showcase that our system can wirelessly control a robotic hand.

4.1 Structure Design of Piezoresistive Sensor

The structure of the fabricated rGO/PS sensor is shown in Figure 4.1. The piezoresistive sensor was constructed with a PDMS substrate, AgNW electrodes and a functional film with deposited rGO and PS spheres mixing solutions. The sensor was encapsulated by a thin PU film to maintain the integrity of the functional layer structure and a PDMS layer to prolong the durability of the sensor.

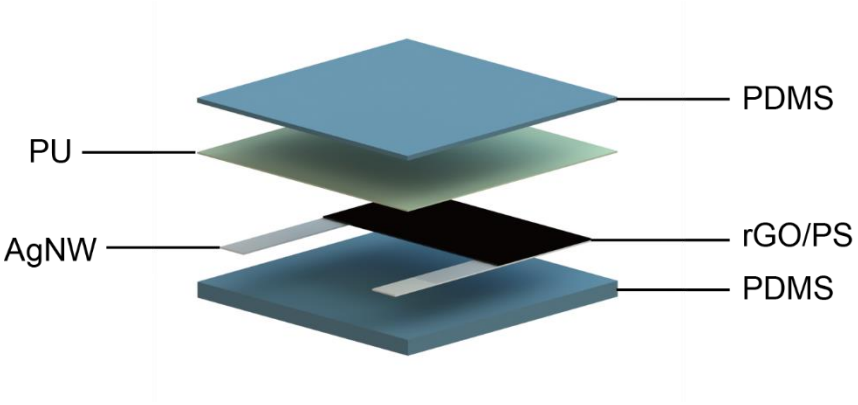

Figure 4.1 The structure of the fabricated rGO/PS sensor.

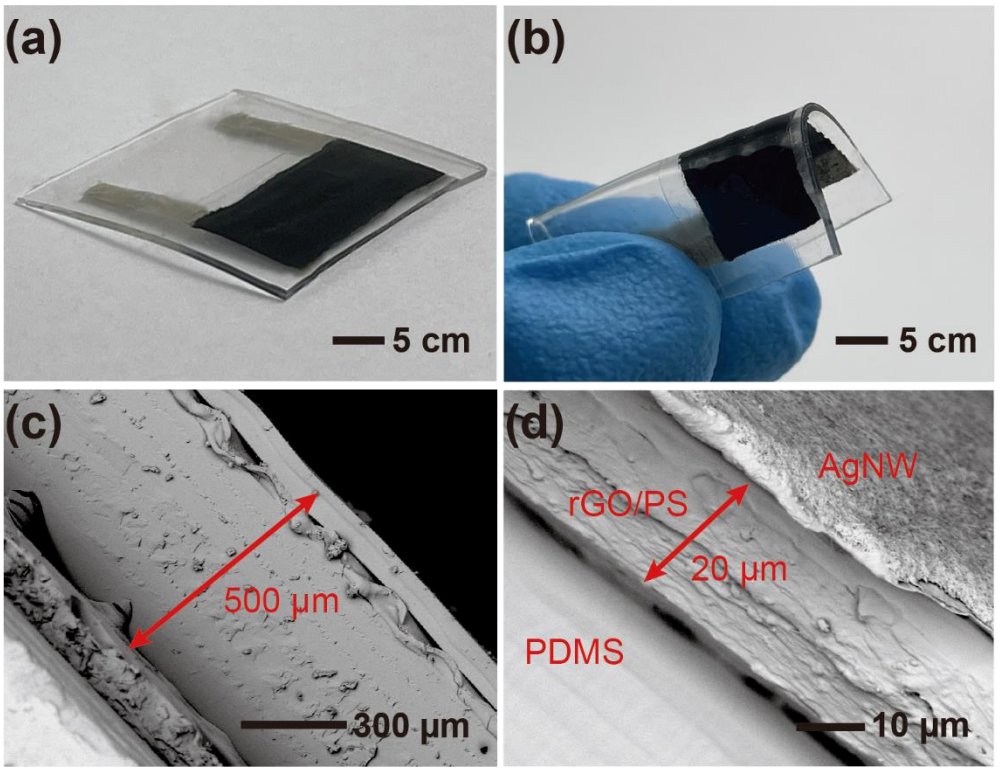

Figure 4.2 (a) and (b) Photographs of the fabricated rGO/PS sensor with the dimension of 20 mm × 20 mm × 0.5 mm, which shows outstanding flexibility of the developed sensor. (c) and (d) Cross sectional SEM images of the piezoresistive sensor.

Figure 4.2(a) and (b) shows the photographs of the developed flexible piezoresistive sensor. The fabricated sensor exhibits excellent flexibility and can be folded 180° without damaging the performance of the device, which further shows the excellent feasibility of the sensors for wearable applications. From Figure 4.2(c) and (d), we can see that the thickness of the whole device is around 500 µm, and the rGO/PS functional layer is about 20 µm.

4.2 Fabrication Process of Piezoresistive Sensor

The fabrication procedure of the rGO/PS piezoresistive sensor is schematically shown

in Figure 4.3. Firstly, the PDMS substrate was prepared. The PDMS monomer and curing agent (Sylgard 184) were mixed for 15 minutes with a weight ratio of 10:1 and then degassed in a vacuum chamber for 30 minutes. The bubble-free PDMS slurry was poured into the prepared mould and cured at 70 ℃ for an hour. The prepared PDMS film was treated with air plasma for 30 seconds to remove the dust and improve the surface adhesion.

The next step involved preparing the flexible AgNW electrodes, as shown in Figure 4.3(a). The AgNW solution (Nanjing XFNANO Materials Tech Co., Ltd. Diameter: 50 nm, length: 20-60 μm) was first diluted to 2.0 mg/ml with ethyl alcohol by 300 r/min magnetic stirring for 30 minutes. The AgNW solution was sprayed on the PDMS substrate every 30 seconds through a 3D-printed mask for a total of 20 times. Afterwards, the AgNW/PDMS film was thermally annealed in the oven at 150 ℃ for 30 minutes to allow junctions to form between AgNWs, thereby increasing the electrical conductivity.

The functional layer of the piezoresistive sensor consisted of rGO fragments and PS spheres. The 2 mg/ml GO solution was prepared by adding 16 mg GO powder (Suzhou Tanfeng Graphene Technology Co., Ltd. Lamella diameter: 0.2-10 μm, purity: 96%) into 8 ml of deionized water. The solution was exposed to a 50 W ultrasonic transducer (bisafer250up, 19-25 kHz) for 15 minutes. Then PS spheres (Tianjin BaseLine ChromTech Research Centre. 2.5 % w/v) were added into the GO solution, followed by leaving the mixture in an ultrasonic bath for another 15 minutes. Next, the 300 μL mixed solution was dropped on PDMS and AgNW in an area of 15 × 8 mm^2. The sample was placed in the oven at 50 ℃ for 3 hours to get a thin GO/PS film (Figure 4.3(b)). The film was patterned by a laser engraving machine (Ruijie RJ-4040)

which directly converted the GO film to rGO by Joule heat (Figure 4.3(c)). Finally, a PU film was placed on the surface of the rGO/PS layer to isolate the uncured PDMS from destroying the rGO interlayer structure, and also fix the wire on the AgNW electrodes. In the end, the whole sensor was encapsulated by PDMS (Figure 4.3(d)).

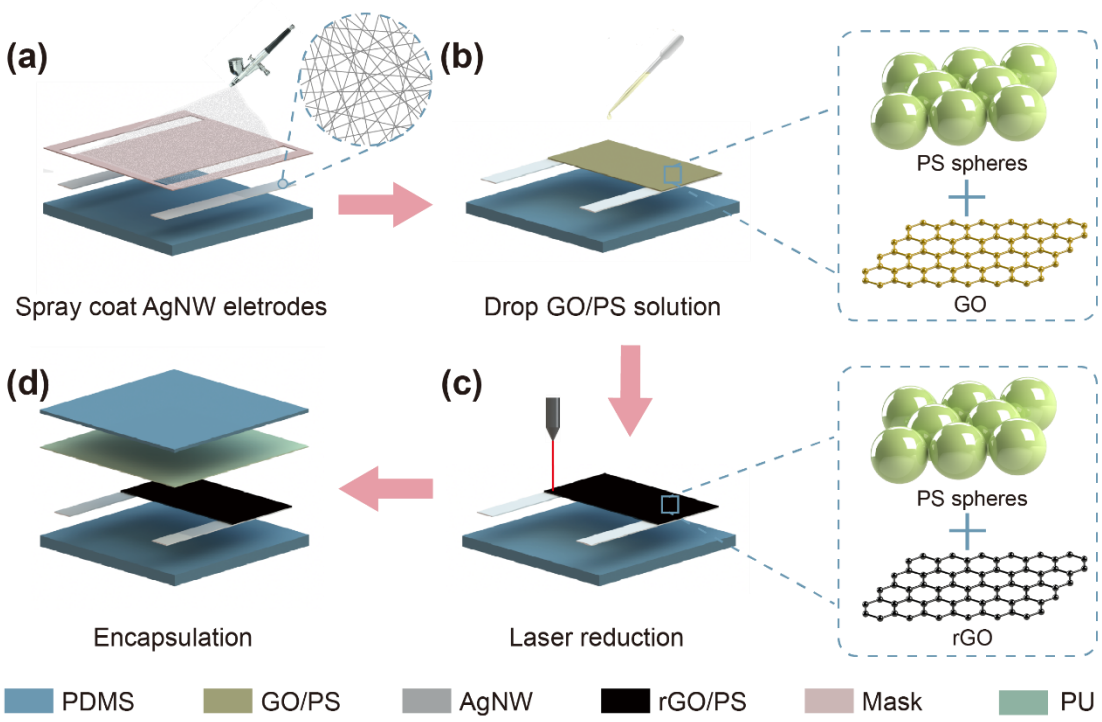

Figure 4.3 Schematic illustration of the fabrication process of the flexible rGO/PS piezoresistive sensor. (a) 2 mg/ml AgNW ethanol-based solution was spray coated on the as-prepared PDMS film. (b) Doped the mixed GO/PS solution on the AgNW electrodes and the PDMS film, and heat for 3 hours until it obtained the dry film. (c) The GO/PS film was patterned by laser-induced reduction that directly converted GO into rGO. The color of the functional layer changed from dark brown to black. (d) Finally, the sensor was encapsulated by a thin PU film and a PDMS layer.

The functional layer of the piezoresistive sensor consisted of rGO fragments and PS spheres. The 2 mg/ml GO solution was prepared by adding 16 mg GO powder (Suzhou Tanfeng Graphene Technology Co., Ltd. Lamella diameter: 0.2-10 μm, purity: 96%) into 8 ml of deionized water. The solution was exposed to a 50 W ultrasonic transducer (bisafer250up, 19-25 kHz) for 15 minutes. Then PS spheres (Tianjin BaseLine ChromTech Research Centre. 2.5 % w/v) were added into the GO solution, followed by leaving the mixture in an ultrasonic bath for another 15 minutes. Next, the 300 μL mixed solution was dropped on PDMS and AgNW in an area of 15 × 8 mm^2. The sample was placed in the oven at 50 ℃ for 3 hours to get a thin GO/PS film (Figure 4.3(b)). The film was patterned by a laser engraving machine (Ruijie RJ-4040) which directly converted the GO film to rGO by Joule heat (Figure 4.3(c)). Finally, a PU film was placed on the surface of the rGO/PS layer to isolate the uncured PDMS from destroying the rGO interlayer structure, and also fix the wire on the AgNW electrodes. In the end, the whole sensor was encapsulated by PDMS (Figure 4.3(d)).

4.3 Characterization

4.3.1 Characterization of AgNW

In order to find the optimal performance of the flexible electrode, four types of fabrication processes have been discussed： cured PDMS film with the plasma treatment; cured PDMS film without the plasma treatment; uncured PDMS film with the plasma treatment; and uncured PDMS film without the plasma treatment. As shown in Table 4.1, uncured PDMS with 60s plasma treatment achieved the best conductivity and stability. However, this plasma treatment changes the stoichiometry and morphology of the polymer surface, and it was difficult to obtain repeatable

results. In this case, cured PDMS with plasma treatment may be a better substrate for coating AgNWs, and the resistance is as low as 3.2 Ω/cm.

The surface morphologies of the AgNW electrodes are shown in Figure 4.4(a and b), indicating the formation of a conductive surface. The detailed morphologies of single AgNW were undertaken by TEM and AFM, shown in Figure 4.4(c and d) and 4.3(f and e), where the diameter of AgNW is around 50 nm. The excellent electrical conductivity and flexibility make AgNW a good material for flexible electrodes in this sensor.

Table 4.1 The comparison of different fabrication processes of AgNW.

Type	Plasma Treatment	Resistance(Ω/cm)	Stability*
Cured PDMS + AgNW	No	100	Low
Cured PDMS + AgNW	Yes	3.2	Medium
Uncured PDMS + AgNW	No	46	Medium
Uncured PDMS + AgNW	Yes	2.2	High

*Stability describes interaction between the PDMS layer and AgNW. Low stability means that AgNW falling off from the PDMS layer after using 5 times. Medium stability means that AgNW falling off from the PDMS layer after using 20 times. High stability means that AgNW falling off from the PDMS layer after using 50 times.

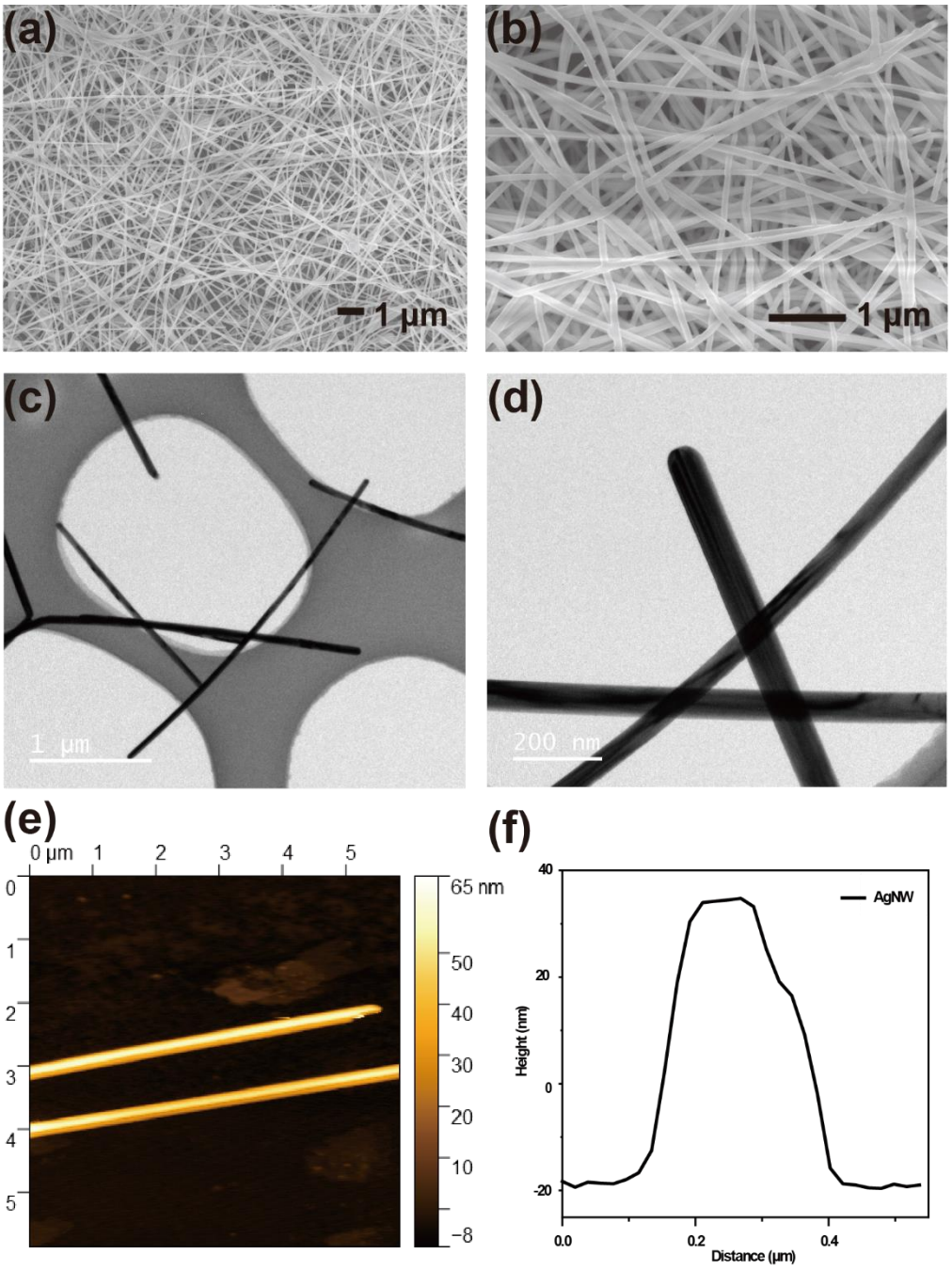

Figure 4.4 (a,b) Surface SEM images of AgNW electrodes in different magnifications. (c,d) TEM images of AgNW electrodes in different magnifications. (e) AFM image of AgNW. (f) Cross-sectional analysis of AgNW.

4.3.2 Characterization of GO and rGO

In this chapter, the GO film was treated using a CO_2 laser through a programmable patterning manner. In comparison with other reduction techniques such as chemical reduction or oven treatment, laser scribing is a convenient and fast way to formulate rGO and allows patterning of the conducting channels [33]. By laser scribing, GO was reduced to rGO according to the photothermal effect. With the increasing local temperature in the patterned laser location, water was evaporated, and Oxygen-Containing Groups (OCG) were removed from the GO film [35], as illustrated in Figure 4.5.

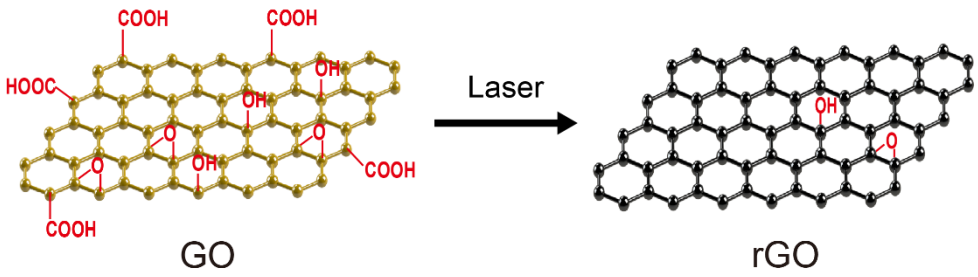

Figure 4.5 GO converted to rGO after laser reduction, where most of the oxygen functional groups were removed.

The rapid release of OCG made rGO form a highly porous structure. The surface morphologies of GO and rGO are shown in Figure 4.6(a) and (b), indicating that the surface of rGO becomes much rougher compared to that of GO. The cross-sectional SEM images of GO film (Figure 4.6(c)) and rGO film (Figure 4.6(d)) demonstrate

that laser reduction has successfully reduced GO into rGO and confirm that the rGO surface is composed of stacked layers. Besides, TEM is also used to detect the morphologies of GO and rGO since it is the tool that is frequently applied to nano-size materials. Figure 4.6(e) presents the surface morphology of GO that is flat and smooth, while it appears wrinkled after laser reduction (Figure 4.6(f)).

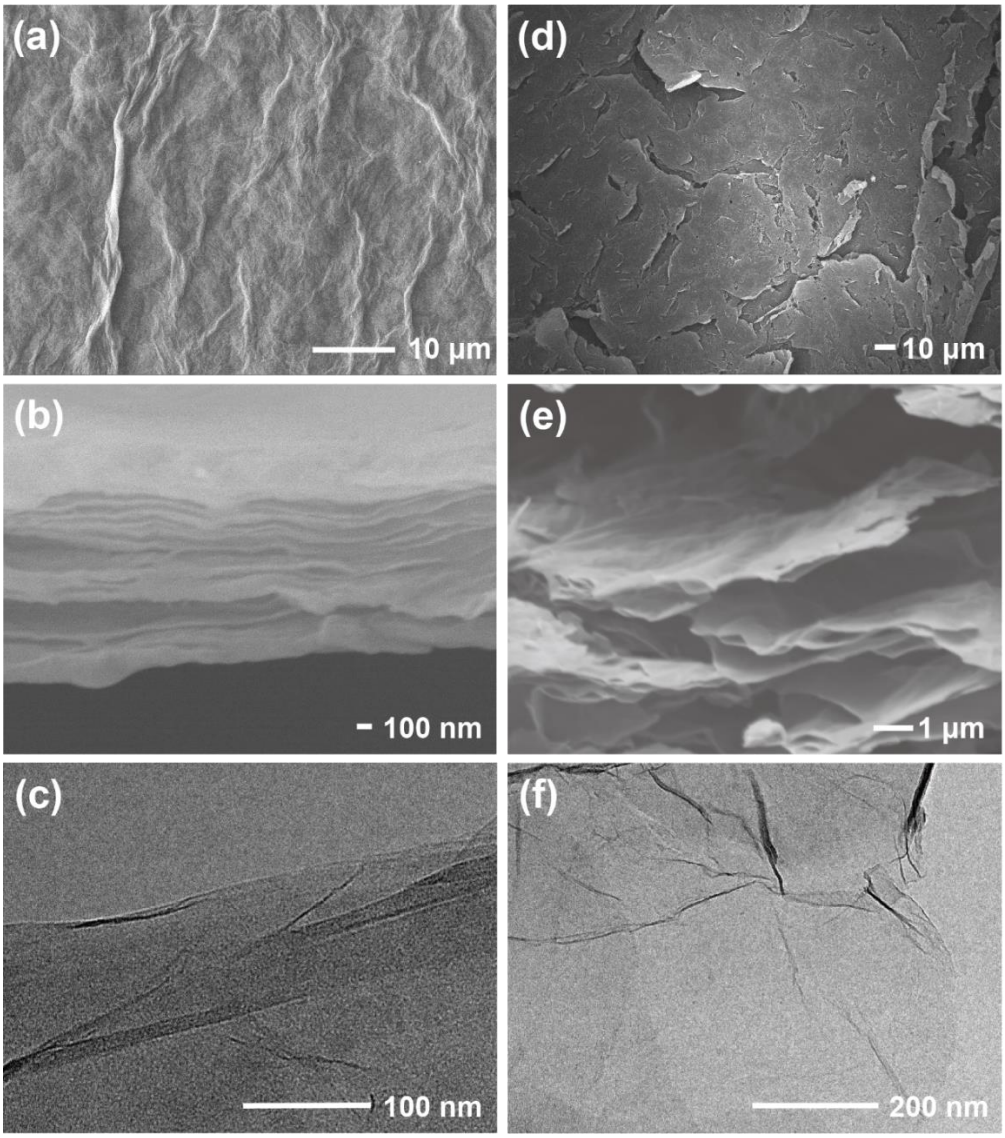

Figure 4.6 (a) Surface SEM image of GO. (b) Surface SEM image of rGO. (c) Cross-sectional SEM image of GO. (d) Cross-sectional SEM image of rGO. (e) TEM images of GO. (f) TEM images of GO.

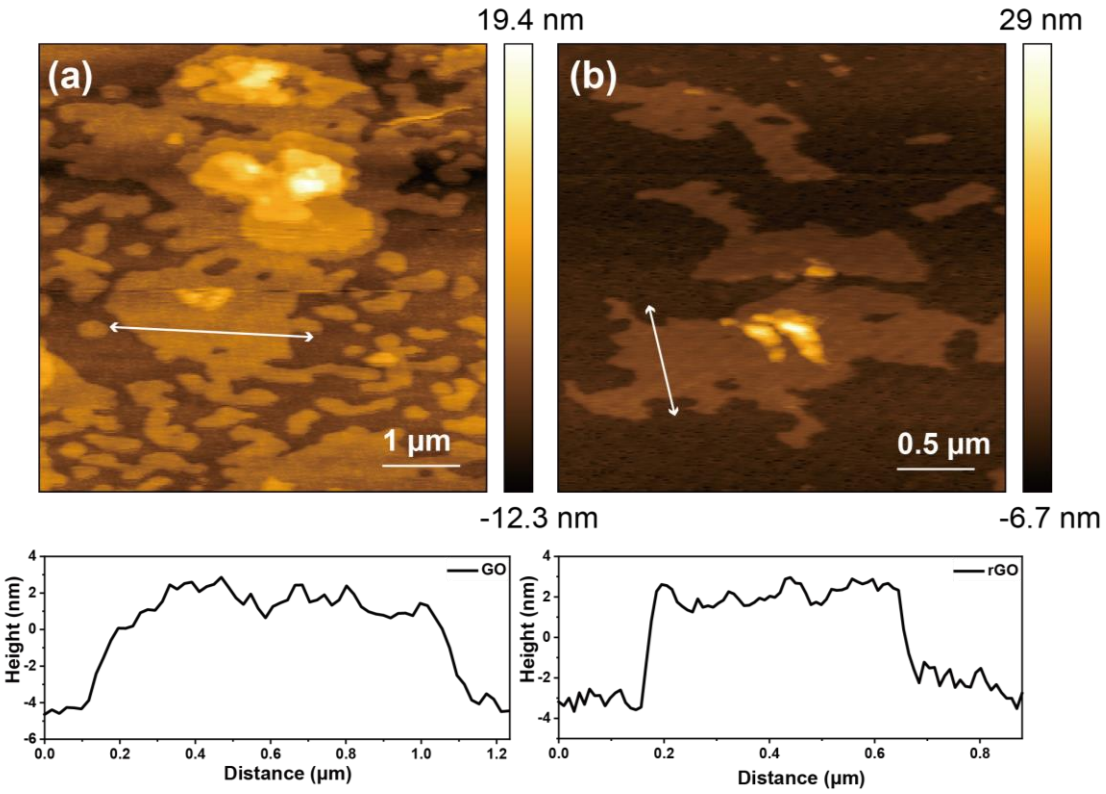

Figure 4.7 AFM images and cross-sectional analysis of (d) GO, (e) rGO.

Furthermore, the morphologies of GO and rGO were characterized in detail by AFM. AFM images of GO and rGO are shown in Figure 4.7(a) and (b). The height of the rGO sheets is around 6.18 nm, thinner than the GO sheets (6.77 nm). Compared with the previous report [36], the tested samples are multilayer. In this case, the reduction in the thickness of rGO could be due to the removal of OCG.

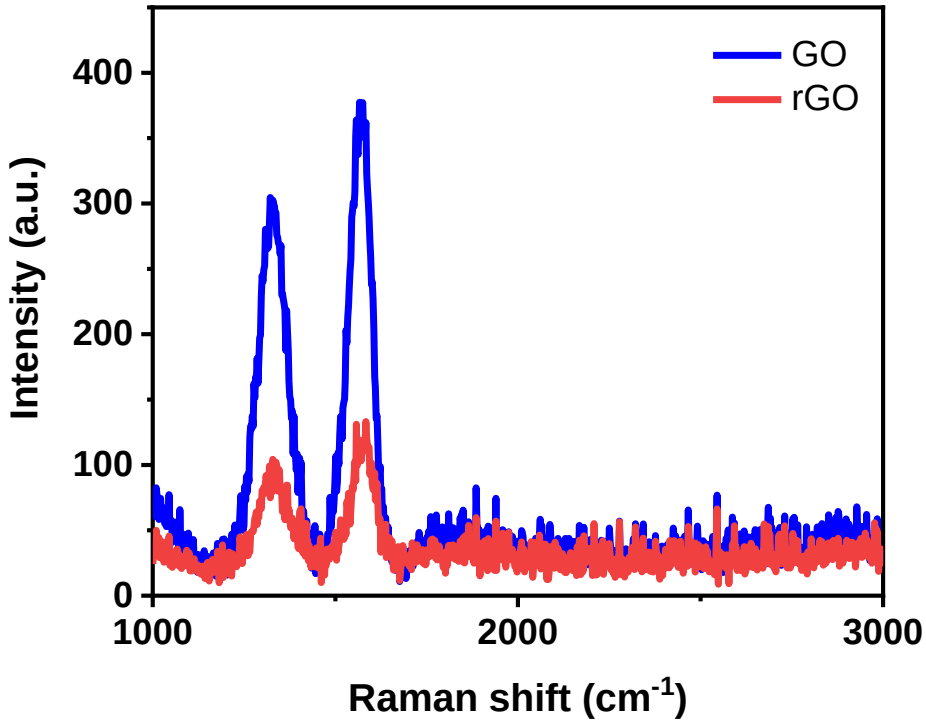

Figure 4.8 Raman spectra of GO and rGO.

To further prove the reduction of the GO film, Raman spectroscopy was conducted to characterize the surface of the sensing film. Raman spectroscopy is a widely used technique for studying structural information of carbon-based materials. The main features in the Raman spectra of graphitic carbon-based materials are the G and D peaks, where the D band is applied to characterize structural defects, amorphous carbon, or edges that split the symmetry and selection rule [37, 38], and G-band is associated with graphitic carbon [35]. The D/G intensity ratio (ID/IG) ratio is an index of the disorder in graphene. From Figure 4.8, the decreasing ID/IG from 0.80 to 0.78 demonstrates the removal of the oxygen-functional groups and the restoration of sp2 domain, so that most GO have converted to the rGO through the laser reduction process.

4.3.3 Working Principle and Sensing Performance

The resistance of the rGO sensor is mainly attributed to two parts: the intrinsic resistance (Ri) of rGO fragments and the contact resistance (Rc) of stacked rGO layers, as shown in Figure 4.9. The total resistance is given by R_{Total} =Ri + ΔRc. When the sensor is under pressure, the distance between two neighbouring interlayers in the rGO will decrease, resulting in a decrease in the internal resistance Rc and an increase in conductivity. As a result, the total resistance of the sensor will decrease. For non-doped rGO, the fragments are stacked closely due to deposition and thermal expansion, which leads to small contact resistance.

To improve the sensitivity of the sensor, the PS spheres were doped as insulators to change the stacking pattern of the rGO fragments. SEM images of prepared rGO/PS piezoresistive sensors are shown in Figure 4.10. In the high magnified figure (Figure 4.10(f)), we can see the PS spheres were sandwiched between the rGO layers, enhancing the gap between the stack layers, which led to the increasing contact resistance of the developed sensor. The between-layer fragment conduction channel is the dominant working principle in this case. Under pressure, the spaces between the rGO fragments become narrow, which results in the formation of multiple conductive channels. The conducting network makes the resistance of the rGO/PS sensor sensitive to pressure.

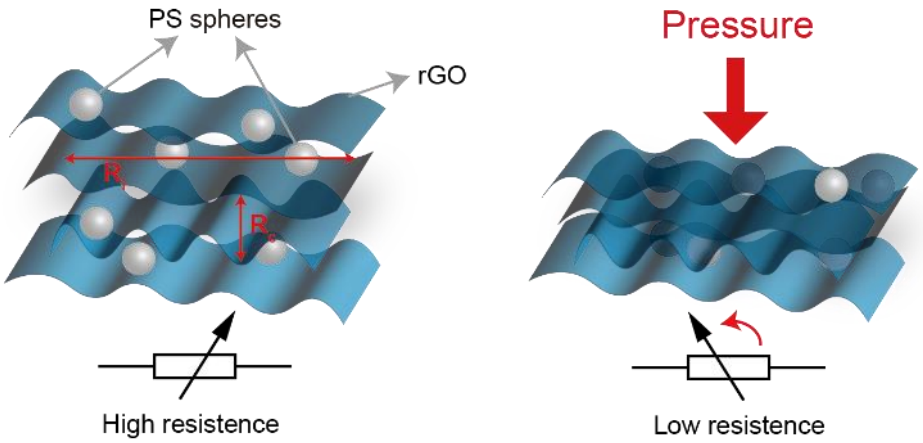

Figure 4.9 Working principle of rGO/PS piezoresistive sensor.

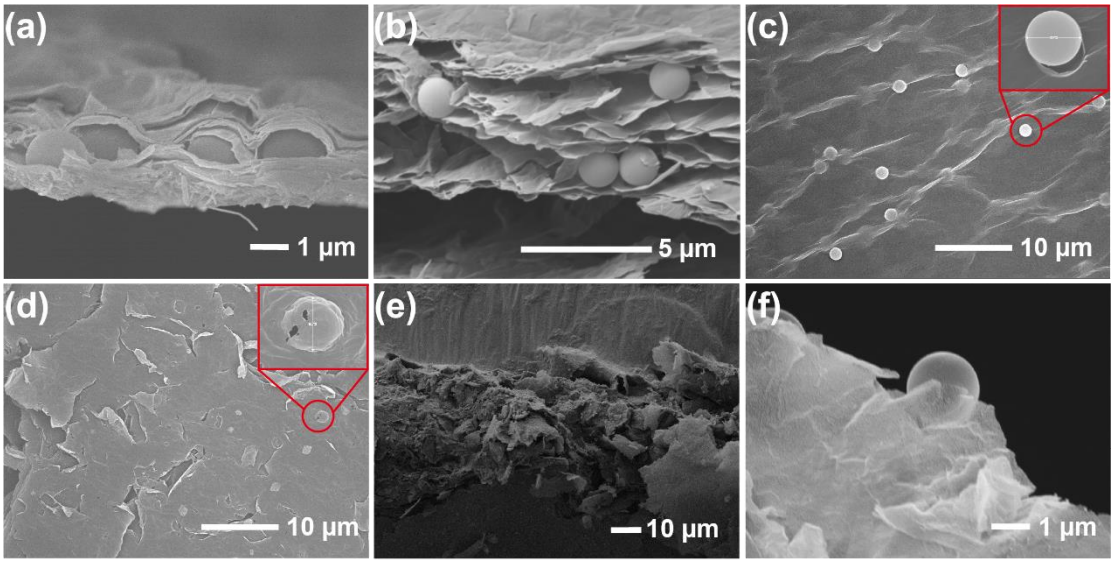

Figure 4.10 (a) Cross-sectional SEM image of the fabricated GO/PS sensor. (b) Cross-sectional SEM image of the fabricated rGO/PS sensor. (c) Surface SEM image of GO/PS structure. (d) Surface SEM image of rGO/PS structure. (e) Cross-sectional SEM image of fracture surface of the rGO/PS sensor. (f) A magnified SEM image of the fracture surface, showing that the PS spheres are sandwiched between the rGO layers.

To investigate the role of the PS spheres, a series of experiments were conducted to study the pressure behaviour of the sensors by adjusting the doping size and doping ratio of PS spheres. The sensing performance of the device was tested under an external mechanical force from 0 N to 10 N. First, different PS spheres diameters varied from 80 nm to 2 μm were investigated. From Figure 4.11(a), the maximum resistance change is over 47% with 2 μm doping PS spheres at 0.2 wt% doping ratio under 10 N, which is almost three times larger than the non-doped rGO sensor. At the small size of the doping spheres (80 nm), the maximum resistance decreases to 35%. When the large size spheres are placed between the rGO fragments, the more significant gap makes the between-layer conducting channels would partially disconnect, thereby introducing a high resistance value at the initial state. When applying external mechanical stresses on the sensor, the resistance of the sensor significantly decreases since the rGO fragments own closer contacts and more contacting sites. Therefore, the sensitivity of the device increases with larger size doping PS spheres.

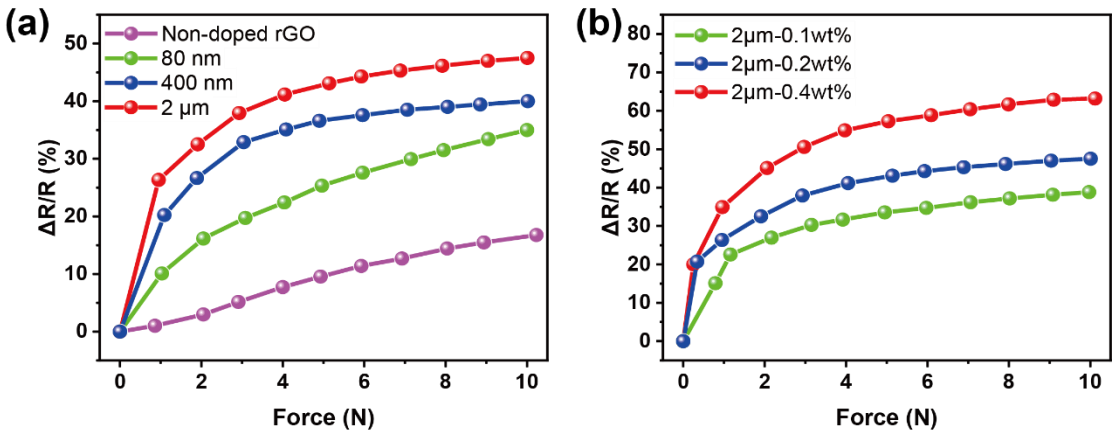

Figure 4.11 The relationship between applied force and resistance changes with (a) different doping PS spheres sizes, (b) different doping PS sphere weight ratios.

To further study the effect of PS spheres on the sensor, the resistance changes of rGO film doped with 2 μm PS spheres of different weight ratios (0.1 wt%, 0.2 wt% and 0.4 wt%) were also investigated. At a small doping ratio (0.1wt%), the space between adjacent PS spheres was large, which makes it difficult for rGO fragments to separate. Thus, the remaining contacting points will influence the sensitivity of the device. A lower doping ratio results in small spacings between adjacent PS spheres, which leads to fewer device contacting points in the initial state. Sufficient space between fragments allows the device to create more contacting channels under external forces. As a result, the resistance change of the sensor increases as the weight ratio of PS spheres increases, as shown in Figure 4.11(b). However, the proportion of PS spheres cannot consistently be increased. When the weight ratio of spheres is larger than 0.4 wt%, the surface of the rGO film arises some small cracks (Figure 4.12 (b) and (c)). Therefore, the 0.4 wt% doping PS sphere performs best as the resistance change reaches 66% under 10 N pressure.

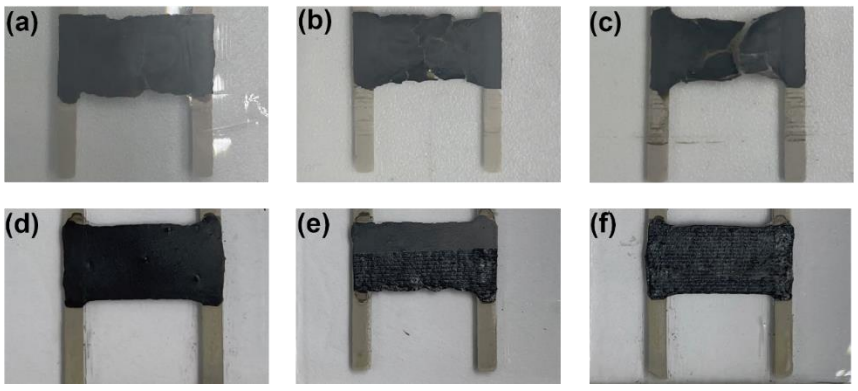

Figure 4.12 The photographs of the flexible sensor: (a) non-doped GO film; (b) 2 μm PS spheres doped GO film at 0.5 wt%; (c) 2 μm PS spheres doped GO film at 1 wt%; (d) 2 μm PS spheres doped GO film at 0.4 wt%; (e) 2 μm PS spheres doped GO film at 0.4 wt%, and half part is reduced by laser, which shows the color of the film changes from the dark brown to black; (f) 2 μm PS spheres doped rGO film at 0.4 wt%.

Moreover, to estimate the detection limit, the resistance change of the rGO/PS device is measured as the load decreases. Figure 4.13(a) shows the pressure dependence of the resistance change ratio of the rGO/PS sensor, where the resistance changes about 6% under 2 g weight, which is a testament to the outstanding sensitivity of our piezoresistive sensor. Furthermore, the piezoresistive sensor shows rapid response and relaxation properties to instantaneous pressure with good reproducibility. The test was repeated three times, and the minimum response and relaxation times were about 186 ms and 378 ms, respectively (Figure 4.13(b)). In addition, the durability of the rGO/PS sensor was tested using a stable vibration platform. To evaluate the mechanical durability of the fabricated sensor, the loading-unloading test was performed under 3 N force and 0.3 Hz frequency. After 1000 cycles, the total resistance and waveform were almost unchanged (Figure 4.13(c)).

Since the developed flexible piezoresistive sensor can work as a wearable device, the stability of the sensor in different humid environments is necessary for practical applications. Herein, the resistance of the sensor under different humidity (from 40.46% to 93.2%) was tested. Although the relative humidity changed by over 40%, the resistance of the developed sensor remained stable (Figure 4.14(a)). Besides, the responses of the sensor during finger tapping movements in air and water at room temperature were also evaluated. As shown in Figure 4.14(b), it is clearly seen that the resistance changes of the sensor in air and water were similar. All the above results show that the sensor exhibits good waterproof performance. Therefore, high sensitivity, fast response, excellent stability, outstanding flexibility and waterproofness give the sensor great advantages in wearable systems.

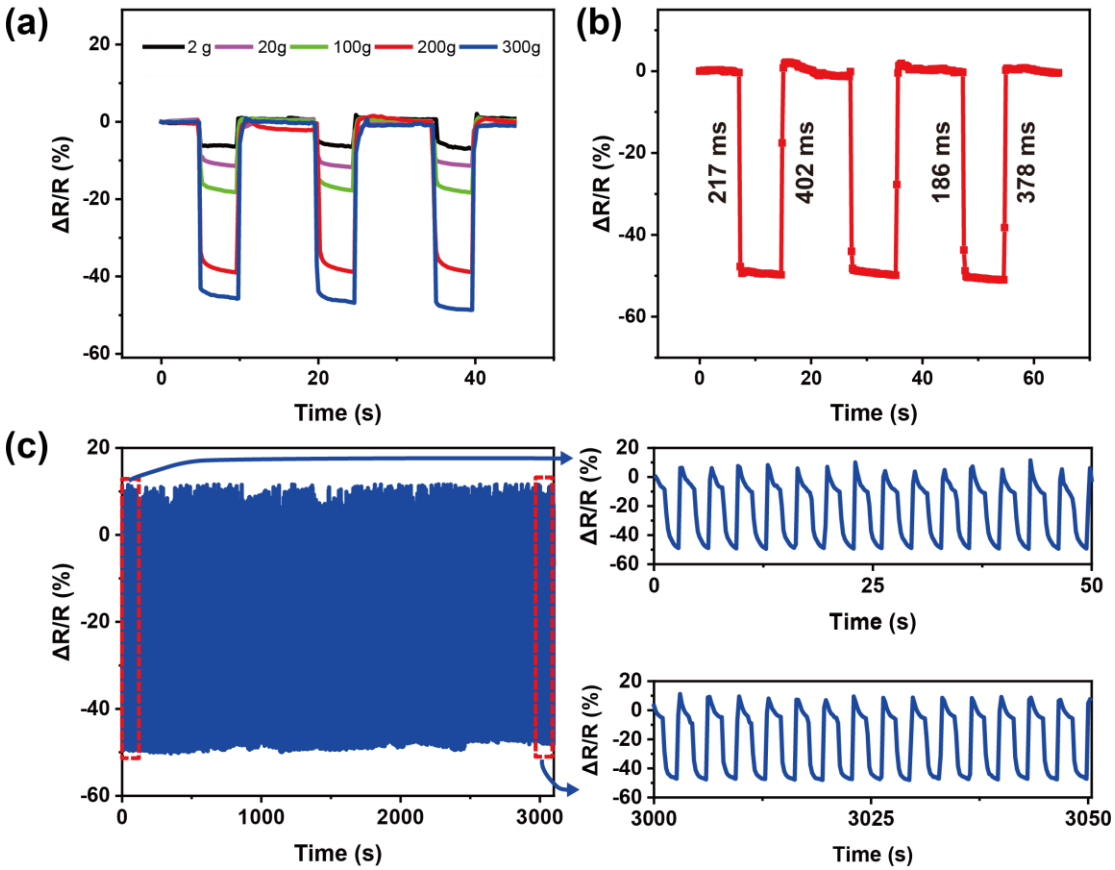

Figure 4.13 (a) The resistance change of the rGO/PS sensor depends on different weights. (b) The piezoresistive sensor shows rapid response and relaxation time. (c) Test the repeatability performance of 1000 cycles under a pressure of 3 N.

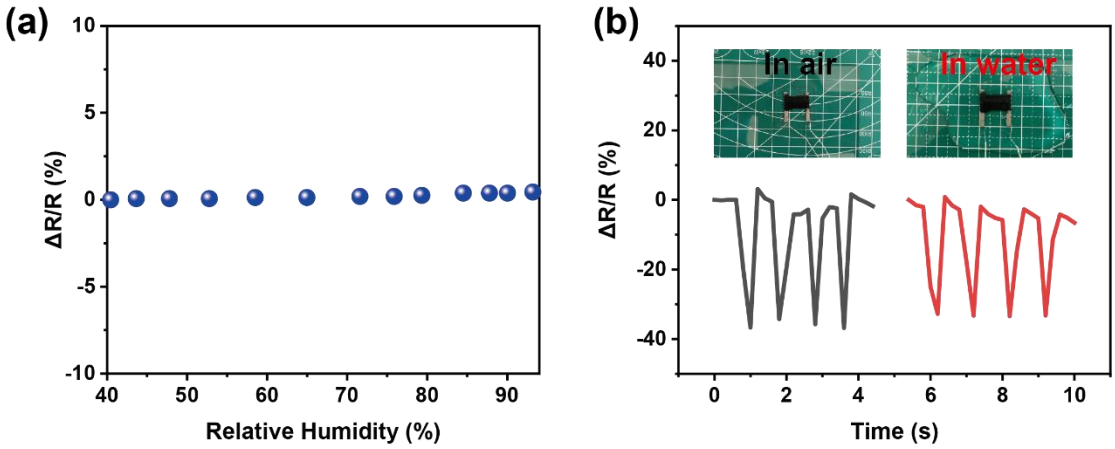

Figure 4.14 (a) The resistance value of the developed sensor under different humidity environments. (b) A comparison of the resistance changes of the sensor during finger tapping movements in air and water at room temperature.

4.4 Sensor-Machine Interface Design and Analysis

4.4.1 Experimental Setup and Data Collection

The superior performance results of fabricated rGO/PS sensors enabled us to integrate them in a wristband device. Photographs of the wristband consisting of an array of five flexible rGO/PS piezoresistive sensors are shown in Figures 4.15, which shows excellent flexibility. Besides, the weight of the whole wristband is only 2.8 g. Thus, high flexibility and lightweight make the wristband comfortable to wear.

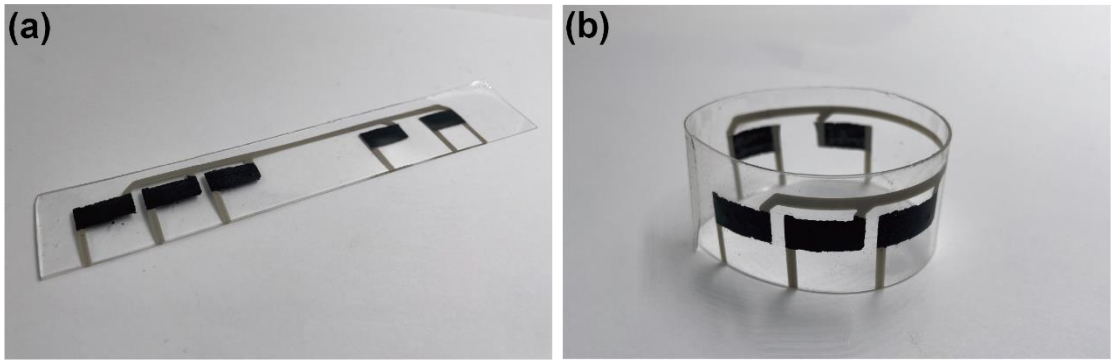

Figure 4.15 Photographs of flexible piezoresistive wristband.

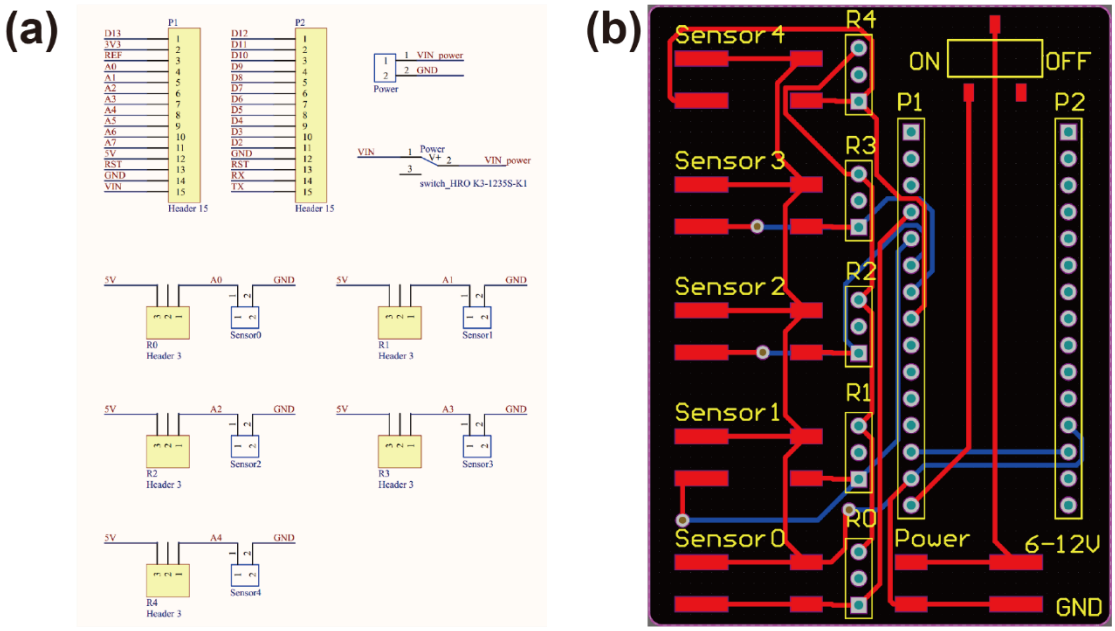

Figure 4.16 (a) Circuit schematic diagram and (b) PCB board layout for piezoresistive wristband signals transfer.

The rGO/PS piezoresistive smart wristband converted pressure signals from tendon movements around the wrist to resistance variations that were then transferred to the voltage readings accordingly through the voltage divider circuit with an additional 5 kΩ resistor, according to the sensors' initial resistance. The circuit schematic diagram and PCB board layout are shown in Figure 4.16.

The voltage calculated between the piezoresistive sensor is:

$$V_{out} = \frac{V}{1+\frac{R_{sensor}}{R}} \tag{4.1}$$

Afterwards, the five-channel output voltage signals were transmitted wireless using an Arduino Nano Bluetooth module to a computer terminal. Data was collected using a LabVIEW interface with a sampling rate of 40 Hz and stored as a five-dimensional vector in the computer for post processing, including the remove baseline drift, find active signal, feature selected and using SVM algorithm to classify the gestures in the MATLAB. The schematic diagram of hand gesture recognition system is shown in Figure 4.17.

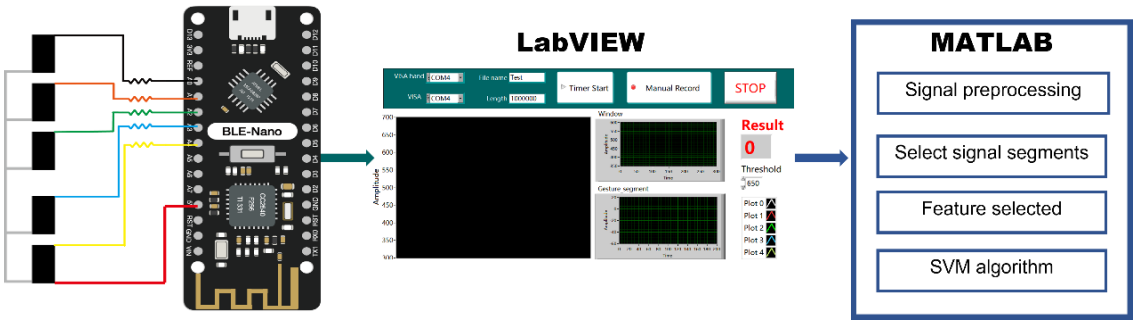

Figure 4.17 Schematic diagram of hand gesture recognition system.

The flexible wristband was placed on the left wrist of the subjects under comfortable tightness without blood restriction, pain and movement limitation. Three sensors were placed on the underside of the wrist because of the high density of tendons in this location, while the other two sensors were fixed on the backside. For hand gesture recognition, five healthy subjects (3 female and 2 male) aged between 23 to 27 were invited to take part in this experiment. The average wrist circumference of the five subjects was 161 ± 9 mm, and two of them were used to wearing a mechanical watch during their daily life. Before the experiment, all subjects were provided informed written consents and the experiments had been approved by the Ethics Committee of university.

All subjects were instructed in advance about the data collecting process and the way of wearing the wristband. The subjects sat in front of a desk and put their elbow on the desk with their forearm raised. The subjects were asked to perform 12 different hand gestures, including both finger flexion and wrist movements. Each subject conducted two trials on one gesture: one record contains 10 repetitive gestures as a training set to train the classification model, and the other record contains 5 repetitions to test the accuracy of the classification algorithm in the recognition step. During the test, the subjects held each gesture for 2 seconds and rested for 5 seconds between gestures. The subjects rested for 2 minutes between each trial to avoid fatigue. The total experiment time for each subject was around 1 hour.

Figure 4.18 presents the corresponding signals and their pressure maps on the wristband for 12 hand gestures. Figure 4.18 also shows the pressure level on each sensor and demonstrates the relationship between the gestures and their corresponding pressure values at the wristband locations.

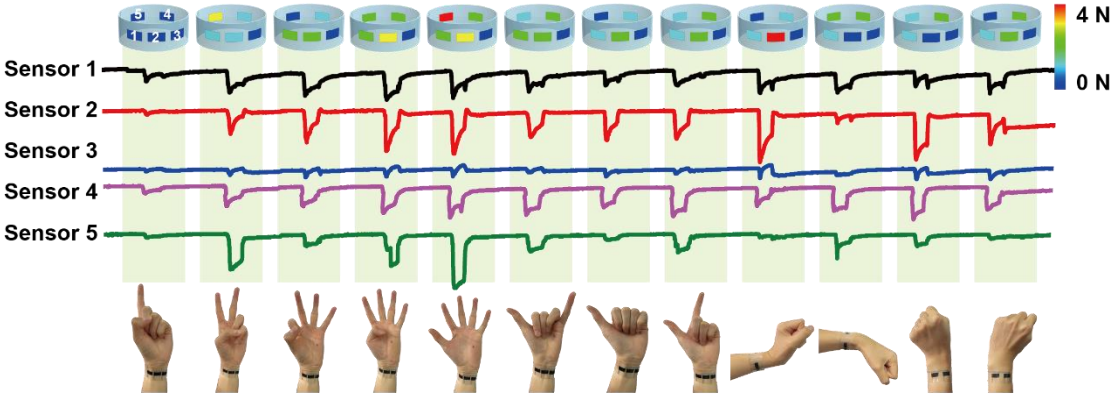

Figure 4.18 Generated signal patterns for different hand gestures, and the corresponding pressure maps on the smart wristband.

4.4.2 Classification Results of Hand Gestures

The acquired data is a mixture of output data from the rGO/PS sensors, time-varying offset and noise. This noise was challenging to completely eliminate using the analogue conditioning circuit, since it may come from sensors, equipment, power lines or electrical radiation from the environment. A low pass filter was used to remove undesirable noise in this case. In the meantime, the baseline drift was also removed. The output signal of the piezoresistive sensor usually showed one noticeable mutation generated by the motion. Due to this characteristic, peak finding was used to detect mutations and their locations for the input vector. After finding peaks in the signal, 200 points were taken before and after the peak to get a complete dynamic gesture signal. To avoid intercepting the same data multiple times, the spacing between adjacent peaks should be more than 300 points. Herein, the whole signal was truncated to small segments according to the maxima of gesture signals.

The numerical data from the piezoresistive sensor varied significantly from one

participant to another. Notably, the difference in wrist size, tendon strength, sensor location and gesture habit for subjects would affect the overall dataset. In this case, instead of using raw data to feed the SVM classifier, 35 statistical features were chosen as more compact and representative information to characterize the data, including mean, maximum, minimum, peak to peak, variance, percentiles, as well as the mean of the cross-correlation function contains the autocorrelation sequences for each channel of the dataset. The details of the feature extraction can be found in Table 4.2.

Table 4.2 Features extracted from the wristband signals.

Feature extraction	Number of features
Mean	5
Maximum	5
Minimum	5
Peak to peak	5
Variance	5
75th percentiles	5
Cross correlation (Mean)	5

Total number of features	**35**

A polynomial-kernel SVM was implemented to train the pre-processed features and reconstruct hand gestures. A kernel function of the 3-polynomial order was used to map the information to a higher dimension. The overall classification accuracy of the trained model for hand gesture recognition was 96.33%. The confusion matrix of the classification result is shown in Figure 4.19(a). The matrix row represents the test samples in an actual class, while the column represents a predicted class. The frequent misclassification occurred between Gesture 7 and Gesture 12, where they have similar pressure patterns on the wristband.

For only the finger flexion, the accuracy reached 97%. Meanwhile, the accuracy of the wrist movements can achieve 100% because movements are more distinguishable. The confusion matrixes are shown in Figure 4.19(c) and (d). For visualization purposes, t-distributed Stochastic Neighbour Embedding (t-SNE) was performed on the feature vectors. t-SNE is a popular nonlinear dimensionality reduction method that is well-suited to visualizing high-dimensional datasets. Using data visualization methods, Figure 4.19(b) demonstrates the feature clustering result of 12 gestures for the input layer in a two-dimensional space, where each colour represents a single gesture group.

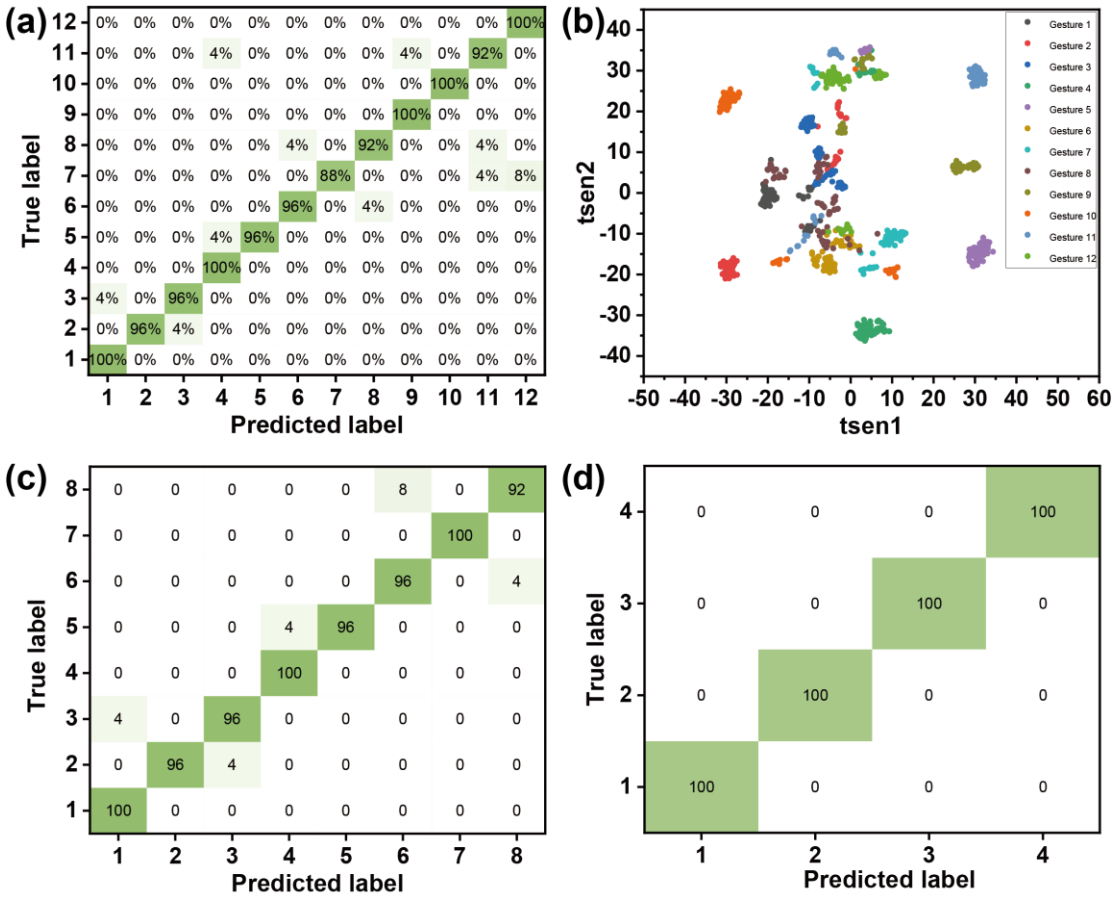

Figure 4.19 (a) Classification confusion matrix for all 12 hand gestures, the accuracy was 96.33%. (b) t-SNE analysis for all 12 gestures. (c) Classification confusion matrix for 8 finger flexion, the accuracy was 97%. (d) Classification confusion matrix for 4 wrist movements, the accuracy was 100%.

4.4.3 Control Robot Hand in Real Time

A proof-of-concept was developed that allowed humans to interact with a robotic hand in real-time by using the SVM algorithm. The schematic diagram of the for HMI is shown in Figure 4.20. The rGO/PS wristband was bound to the user's wrist to capture the tendon movements for different hand gestures. Moreover, signals generated by the piezoresistive sensors were transmitted wirelessly to the computer.

After the pre-processing, each gesture signal was windowed to perform feature extraction. A LabVIEW interface displayed the real-time signals and the recognition results (Figure 4.21). The results were transmitted to the robotic hand for real-time control. The experimental setup is shown in Figure 4.22. As shown in the Figure 4.23, different hand gestures were successfully translated from the human hand to the robotic hand. There is about 1 second delay in the system. This real-time HMI application, which has been integrated with flexible rGO/PS sensors, shows excellent capability in continuous human motion monitoring and robot control, which have a promising potential for the use in remote robot-assisted precision operations.

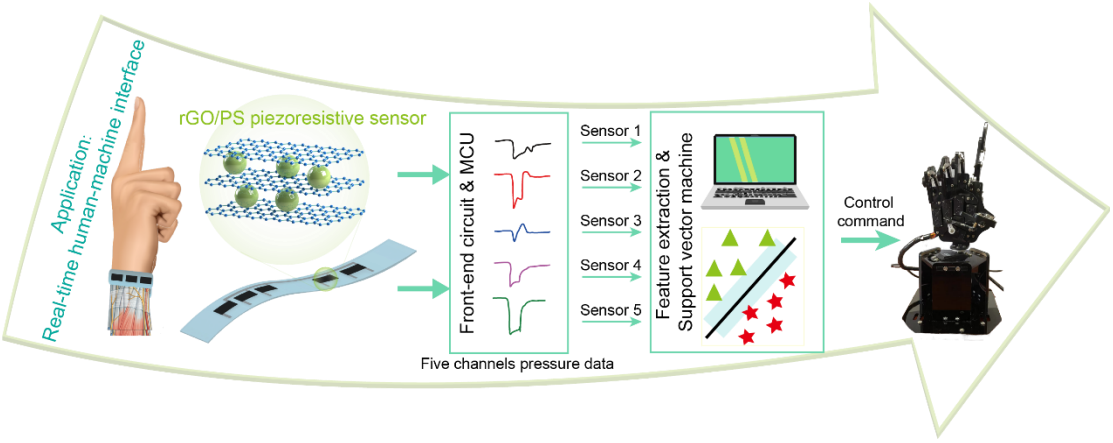

Figure 4.20 The schematic diagram of the proof-of-concept real-time control for HMI.

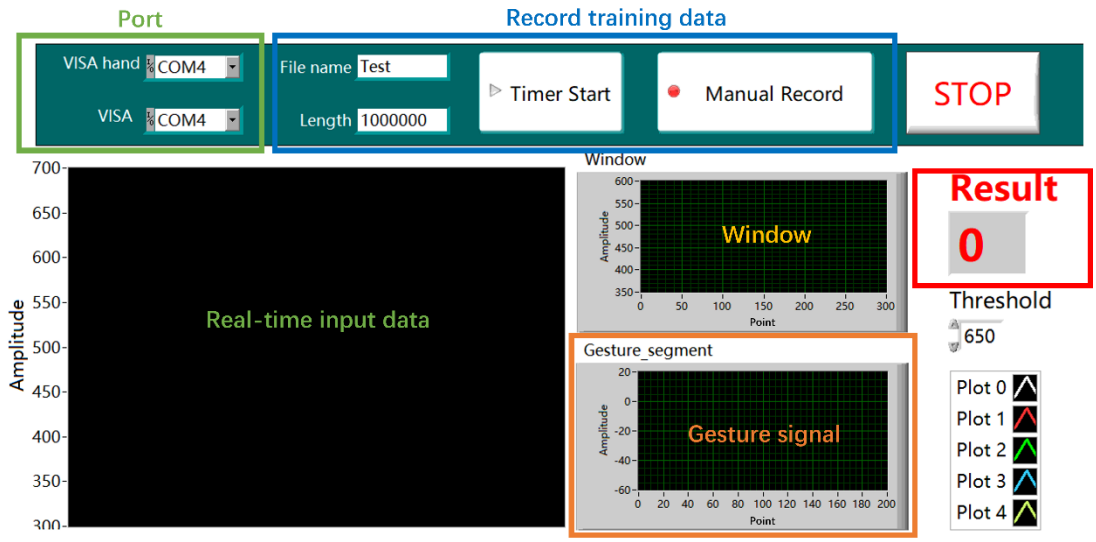

Figure 4.21 LabVIEW interface of collecting gesture signals and showing recognition results to control a robotic hand in real-time.

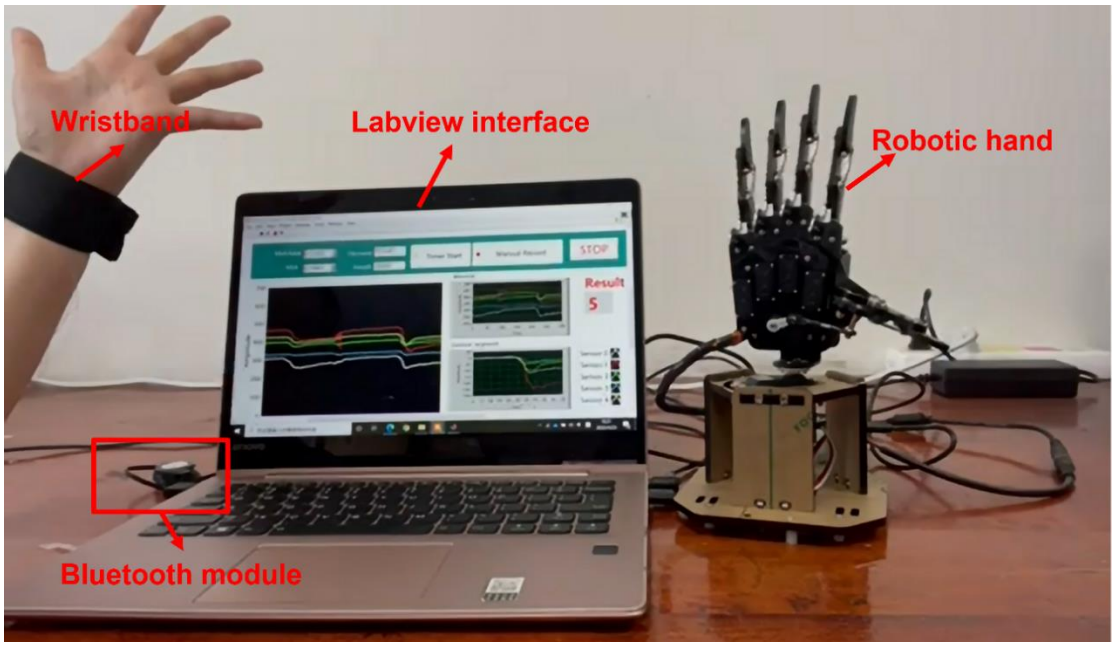

Figure 4.22 Real-time robotic hand control with flexible piezoresistive wristband.

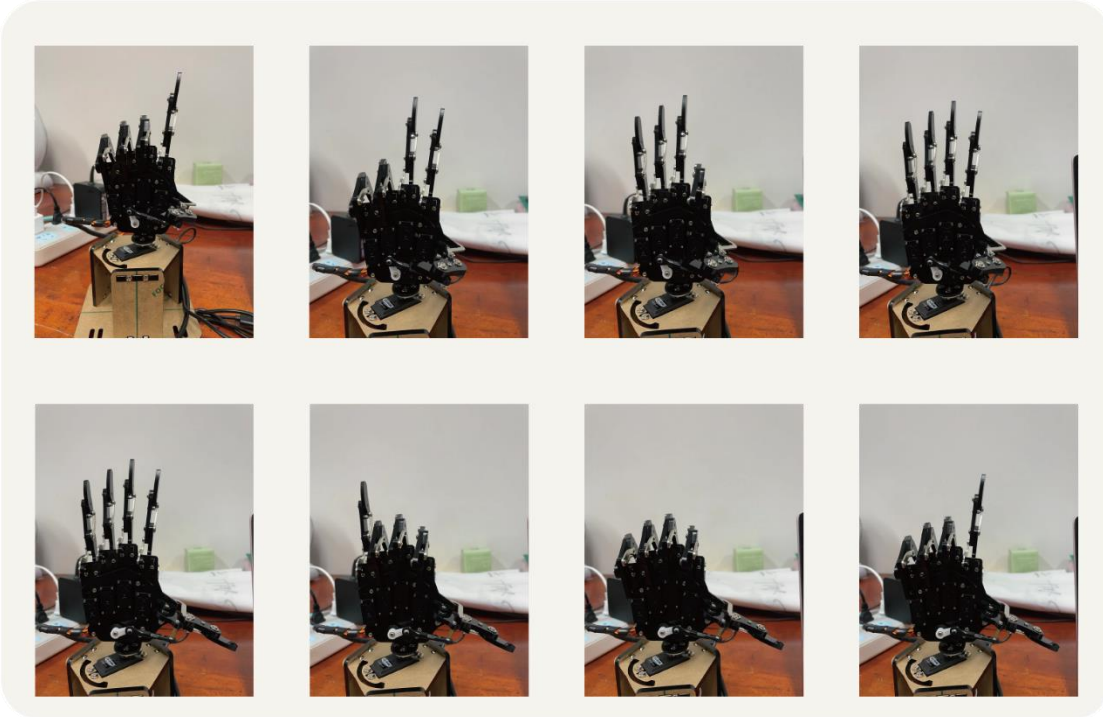

Figure 4.23 Robotic hand controlled by flexible wristband.

4.5 Summary

A flexible and highly sensitive piezoresistive sensor has been demonstrated, as well as its application in a wearable hand gesture recognition system. The sensor was deposited with a mixed solution of rGO and PS spheres, where the spheres acted as insulators to separate the rGO fragments, resulting in a larger contact resistance change under pressure. We observed that doping different sizes and weight ratios of spheres influenced the sensing performance of the device. Therefore, by optimizing our design, a maximum resistance change of 66% was achieved when doping 2 μm spheres at 0.4 wt%, which is more than 4 times higher than non-doped rGO sensors.

Therefore, a highly flexible wristband was designed based on rGO/PS sensors to

capture pressure distribution around the wrist. Data processing methods were used to truncate signal segments and extract feature information. In combination with an SVM classifier, 12 hand gestures were successfully recognized with a classification accuracy of 96.33%. To further support the use of our wristband device in an HMI application, we developed a real-time system that allows the user to control a robotic hand. The above results suggest that the flexible rGO/PS piezoresistive sensor offers excellent characteristics to assemble smart learning algorithms for next-generation wearable HMI.

A detailed comparison of our system with existing state-of-the-art wristband devices is shown in Table 4.3. The selected publications are the state-of-the-art studies with the following criteria: 1) published in recent 5 years, 2) wrist-worn sensors for gesture recognition, 3) machine learning algorithms were used for classification and 4) yielded acceptable results. Our custom-designed wristband is fully flexible and lightweight, which is essential for device wearability. In comparison with other wrist-worn methods, the rGO/PS flexible wristband demonstrated in this chapter has fewer sensor channels while achieving higher classification results.

Table 4.3 Performance comparison of hand gesture recognition system with rGO/PS flexible wristband and similar wristband products.

Sensor type	Number of sensors	Number of gestures	Number of Participants	Algorithm	Accuracy	Flexible	Weight	Ref
Triboelectric +Piezoelectric	8	26	Not mention	LDA	92.6%	No	Not mention	[136]
sEMG+IMU	4 sEMG+ 1 IMU	8 air gesture + 4 surface gesture	4	LDA	92.8%/ 88.8%	No	56g	[137]
Piezoelectric sensor	6	5	1	SVM	97%	No	1.8g+ 18.6g	[61]
Barometric Pressure sensor	10	19	10	LDA/SVM/ KNN	94%	No	3.7g+ 18.6g	[138]
Capacitive sensor	5	3	1	SVM and DAG	90%	No	Not mention	[100]
Electrical impedance tomography	16	8	2	ANN	99.5%	No	Not mention	[139]
Microphones	40	36	10	LDA/SVM	91%	No	Not mention	[140]
Inertial sensor	1	12	5	ADBA	99.2%	No	26g	[141]
Piezoresistive sensor	5	12	5	SVM	96.33%	Yes	2.8g	This work

Chapter 5

Piezoresistive Sensor for Speech Recognition

Vocal cords, as folds of pharyngeal tissue, are the main structures of human vocalization. During vocal actions such as speaking and singing, the vocal folds vibrate by interacting with the air. Lesions of the vocal cords can lead to hoarseness or even complete loss of voice, resulting in communication barriers [142]. In this case, speech-assistive devices have been proposed to help patients with language expressions. Traditionally, the hand-held electrolarynx requires the user to press the device firmly against the neck or inside the mouth when speaking, which causes significant distress when trying to speak while performing two-handed tasks such as driving or eating [143, 144]. Therefore, flexible and wearable artificial larynx devices would promote the convenience of communication for mute patients.

Different flexible force-sensitive sensors show great potential in various fields such as

electronic skins [33], health monitoring [145] and artificial intelligent systems [126, 146] since they can easily convert mechanical stresses into electrical signals. Nowadays, plenty of pressure sensing mechanisms have been explored including piezoresistive [147], capacitive [148], piezoelectric [149] and triboelectric [150, 151]. In particular, piezoresistive sensors stand out as promising candidates due to their low-cost, low power consumption and easy signal collection [152, 153]. To achieve higher sensitivity, the architectural design has been incorporated into sensor development. The microstructures are designed to amplify mechanical loading effects. Such microstructures include geometry structures such as the dome [32], wave [33], pillar [34], fibres [36] and pyramid [37] shapes, as well as bionic patterns such as banana leaves [39], petals of rose [40] and mimosa [41]. The resulting resistance changes in the material system can be enlarged and lead to better sensitivity. However, these template-assisted methods often require complex preparation processes and high-cost fabrication tools. For this reason, easy fabrication methods were required to build the microstructures. In this chapter, we demonstrate a new fabrication method that involves spraying PS spheres using an airbrush, which is a simple and time-saving method for fabricating the microstructures. Unlike other design strategies, the microstructures can be changed simply by varying the weight ratio and size of the PS spheres.

The selection of suitable conductive materials for the sensor was based on charge transport properties in piezoresistive sensors. In recent years, a variety of conductive materials, such as carbon nanotubes [154], carbon black [155], metal nanowires [156], and graphene [157], have been used in piezoresistive sensors. Generally, charge transport is easier and quicker in highly conductive materials such as AgNW, while it

is slower and less efficient in materials such as rGO which has defects and oxygen-containing groups on the surfaces and edges[134, 158]. With the two materials combined, their electrical properties can be enhanced due to synergistic effects. Therefore, the variation in conductive pathways is crucial during our design of piezoresistive sensors.

Besides, a significant body of research has been devoted to using flexible sensors to detect human neck muscle movements in recent years. For example, an intelligent artificial throat based on laser-induced graphene was able to generate sound and detect simple throat vibrations with different intensities or frequencies [159]. Another artificial graphene throat was proposed that also integrated both sound detection and emission in a single device, which can detect simple pronunciations when attaching the device to the human neck [160]. However, these devices only initially detected throat movements without further exploring the feasibility of implementing artificial intelligence for speech recognition. In this case, an MXene-based artificial throat device was developed to detect different pronunciations of several different words, and it can also recognize long vowels and short vowels of the syllable "a" with a deep-learning algorithm when the device is attached to the vibrating membrane of a loudspeaker [107]. However, this research still did not directly recognize human throat pronunciations to truly enable human-machine interaction. However, this research did not attach the sensor to human throat for experimental data collection. More recently, a graphene-based wearable sensor was attached to human throat to classify the words and throat movements with the accuracies of 55% and 85%, respectively, by using the neural network [161]. In this case, a more accurate system should be developed for speech recognition by wearable sensors.

Herein, we proposed a high-performance flexible piezoresistive sensor with a simple fabrication process that acts as an intelligent throat to recognize the different throat pronunciations. The sensor was constructed by two PDMS layers that coated by AgNWs and rGO films, respectively, where the microstructures were built by pray coating the PS spheres between the layers. Unlike other architecture design strategies, the microstructure can be changed simply by varying the weight ratio and size of the PS spheres. Compared with the piezoresistive sensor fabricated in Chapter 4, the as-prepared piezoresistive sensor demonstrates excellent sensing performance under the subtle pressure range: high sensitivity (21.8 kPa^{-1}), ultralow detection limit (2.1 Pa), quick response time (162 ms) and cycle stability (> 5000 times). The excellent properties make the sensor able to detect small physiological signals such as finger bending, eye blinking and throat movements. Moreover, an intelligent artificial throat has been realized by combining the flexible piezoresistive sensor with the ANN algorithm, which not only detects sounds but also classifies the pronunciation of different words. When attaching the sensor on the human throat, it can distinguish the throat vibrations of speaking five different words with a high accuracy of 96%.

5.1 Structure Design of Piezoresistive Sensor

The schematic diagram of the sensor is illustrated in Figure 5.1(a). Briefly, the sensor consists of two conductive layers of AgNWs and rGO, and PS spheres as the microstructures sandwiched between them. The simple device structure allows the proposed sensor to have an easy, convenient and low-cost manufacturing process, including spray coating technology for AgNWs and PS spheres (Figure 5.1(c) and (d)) and laser reduction technology for rGO preparation (Figure 5.1(e)). The laminar-

structured device also possesses remarkable flexibility, as shown in Figure 5.1(b), where the sensor was folded at 180° in a bending state without any damage. The fabricated piezoresistive sensor with the dimension of 25 mm × 15 mm, where the area of the function layer is 15 mm × 8 mm. The thickness of the sensor was 0.65 mm.

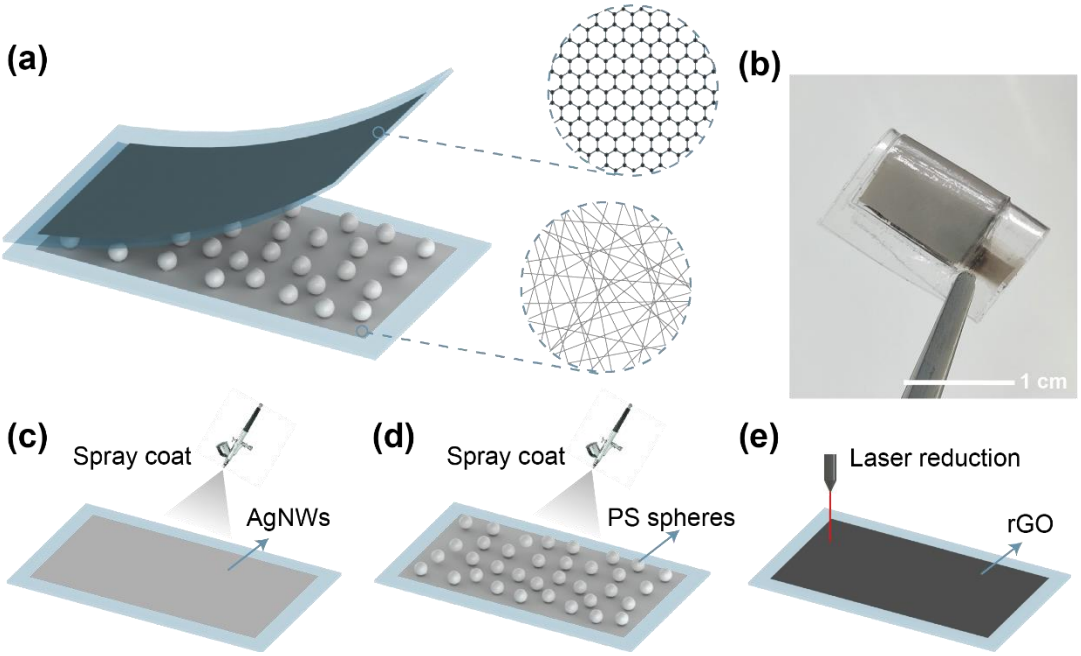

Figure 5.1 (a) Schematic diagram of the piezoresistive sensor. (b) Photograph of the fabricated sensor which shows outstanding flexibility. (c) AgNWs solution was sprayed onto the as-prepared PDMS film. (d) PS solution was sprayed onto the AgNWs film. (e) The rGO film was prepared by laser-induced reduction that directly converted GO into rGO.

5.2 Fabrication Process of Piezoresistive Sensor

First, two PDMS substrates were prepared by mixing PDMS monomer and curing agent (Sylgard 184) in a weight ratio of 10:1 for 15 min, and then the mixture was poured into two plastic petri dishes. The petri dishes were placed in a vacuum chamber to remove air bubbles at ~1×10-2 MPa for 30 min. After curing at 70°C for 1

h, the solid PDMS films were peeled off and placed on glass plates.

The second step is to prepare the AgNWs layer and two AgNWs flexible electrodes. A 2 mg/mL AgNWs solution was prepared by adding 1 mL of 20 mg/mL AgNWs stock solution (Diameter: 50 nm, length: 20-60 μm) to 19 mL of absolute ethanol. The diluted solution was stirred for 30 min to obtain a homogeneous solution. A rectangular 3D printed mask (15 mm x 8 mm) was placed on one solid PDMS film, and a 3D printed mask with two parallel slits was placed on the other PDMS film. The glass plates were placed on a hot plate to reduce the drying time of AgNWs solution during spraying and the temperature was set to 50°C to avoid deformation of the 3D printed masks. The exposed PDMS areas were sprayed with AgNWs solution using an airbrush with a 0.3 mm nozzle. The spraying was repeated every 30 s for a total of 20 times to obtain a uniform AgNWs layer. The AgNWs/PDMS was then thermally annealed in an oven at 150°C for 30 min.

The AgNWs/PMDS film with a rectangular shape worked as the functional layer. Different weight ratios (0.25 wt%, 0.025 wt% and 0.0025 wt%) of the PS spheres were prepared by diluting the original 2.5 wt% PS spheres (Diameter: 2 μm, 20 μm and 40 μm) with absolute ethanol, and magnetic stirred for 30 min. The PS spheres were sprayed on the AgNWs layer 2 times with an interval of 1 min for complete alcohol evaporation, then waiting for assembling.

Meantime, a 2mg/mL GO solution was obtained by adding 1.6 mg GO powder into 8 mL of deionized water. The prepared solution was exposed to a 50 W ultrasonic transducer (bisafer250up, 19-25 kHz) for 15 min to obtain a highly dispersed GO solution. The PMDS film with two AgNWs electrodes was covered by another

rectangular 3D printed mask (15 mm x 8mm), and 300 μL GO solution was dropped on the exposed area and then placed in an oven at 40℃ for 3 hours to get a dense film. Then the GO film was reduced by the laser engraving machine to get the rGO film. Finally, put the AgNWs/PS film on top of the rGO functional layer, and the whole sensor was encapsulated by the polyurethane film.

5.3 Characterization and Working Principle

To further investigate the morphology of the fabricated sensor, SEM images were taken after each step of the fabrication process. Figure 5.2(a) shows the surface morphology of the AgNWs on the PDMS substrate after spray coating 20 times, where a dense network of AgNWs is observed. The average diameter of the randomly oriented AgNWs is about 100 nm. The dense AgNWs film owns high conductivity, and the resistivity reaches 3 Ω/cm. Figure 5.2(b) shows the top view of PS spheres on the AgNWs film, where the microspheres are randomly scattered on the surface. Figure 5.2(c) is the cross-sectional view of the rGO film, where the stacked segments of rGO can be seen clearly. Compared to the GO film, the rGO becomes more porous after the laser reduction, and the resistivity is about 400 Ω/cm.

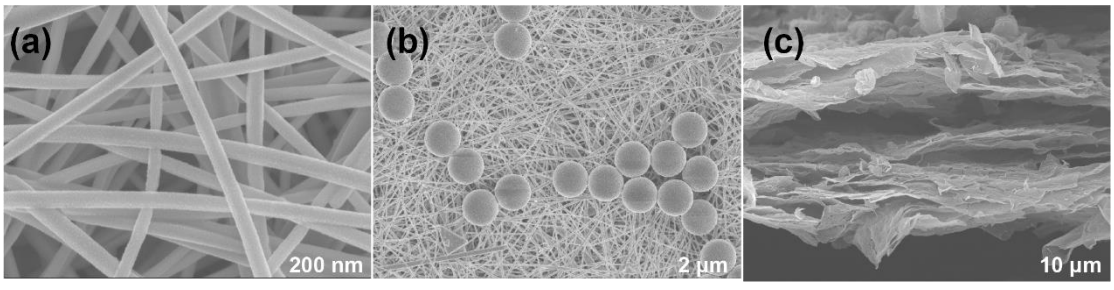

Figure 5.2 SEM image of (a) AgNWs, (b) PS spheres on the AgNWs film and (c) rGO.

To understand the basic working principle of the device, we first prepared the AgNWs/rGO device without PS spheres. Figure 5.3(a) briefly depicts the sensing mechanism of the piezoresistive sensor without PS spheres. When external force is applied to the sensor, the AgNWs layer and the rGO layer will be in close contact and generate conduction channels. It is worth noting that the resistance of AgNWs network is much smaller than that of rGO, so the current tends to flow through AgNWs, resulting in a significant reduction in the total resistance of the device. However, from the cross-sectional SEM image of the device (Figure 5.3(b)), there are some contact points between the AgNWs layer and the rGO layer without external pressure. These existing conduction points lead the device to poor response under pressure. In order to evaluate the sensing performance of the device, an LCR meter was employed to record the real-time resistance when an external mechanical force (0-10 kPa) was applied to the sensor. Figure 5.4(a) indicated the resistance change of AgNWs/rGO device on various pressures. The relative resistance change of the device is defined as $\Delta R/R$ (%), where R is the resistance of the sensor under no pressure, and ΔR equals the resistance under pressure minus R. In addition, the sensitivity of a pressure sensor is the key parameter to evaluate the performance of a pressure sensor and is described by $S = (\Delta R/R)/\Delta P$. In this case, the resistance change of the AgNWs/rGO device is about 28% under 10 kPa, and the sensitivity is 0.161 kPa^{-1} in the low-pressure range. The minimum detection limit of the device was also tested by applying different pressure. From Figure 5.4(b), the sensor was still sensitive under 20.6 Pa pressure, with a 4% change in resistance.

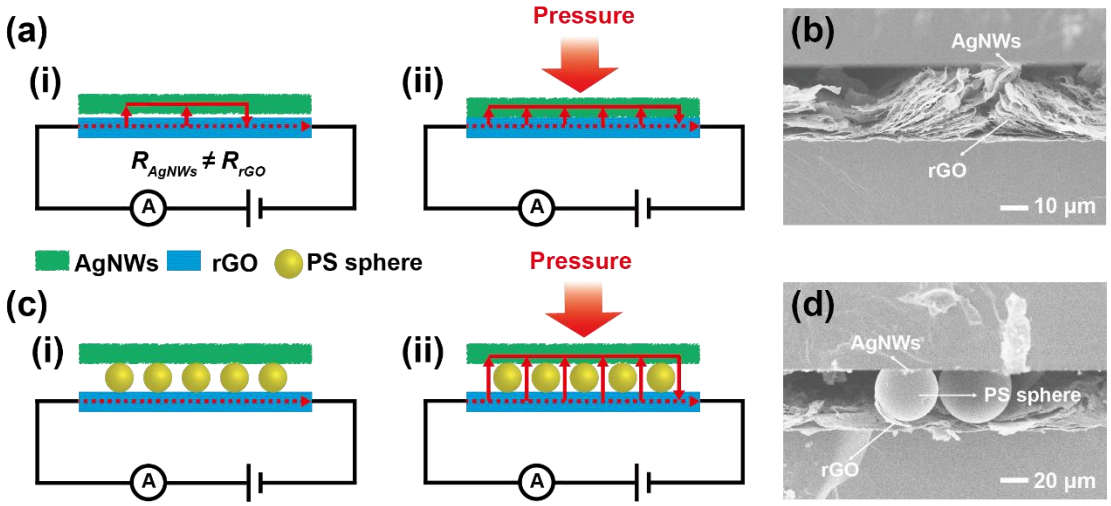

Figure 5.3 (a) Schematic diagram of the working principle of the AgNW/rGO piezoresistive sensor without PS microspheres during (i) release and (ii) pressure cycles. (b) Cross-sectional SEM image of AgNW/rGO piezoresistive sensor, indicating some contact points between the AgNWs layer and the rGO layer at release state. (d) Schematic diagram of the working principle of the AgNW/PS/rGO sensor during (i) release and (ii) pressure cycles. (d) Cross-sectional SEM image of AgNW/PS/rGO piezoresistive sensor, where PS spheres separate the AgNWs layer from the rGO layer at release state.

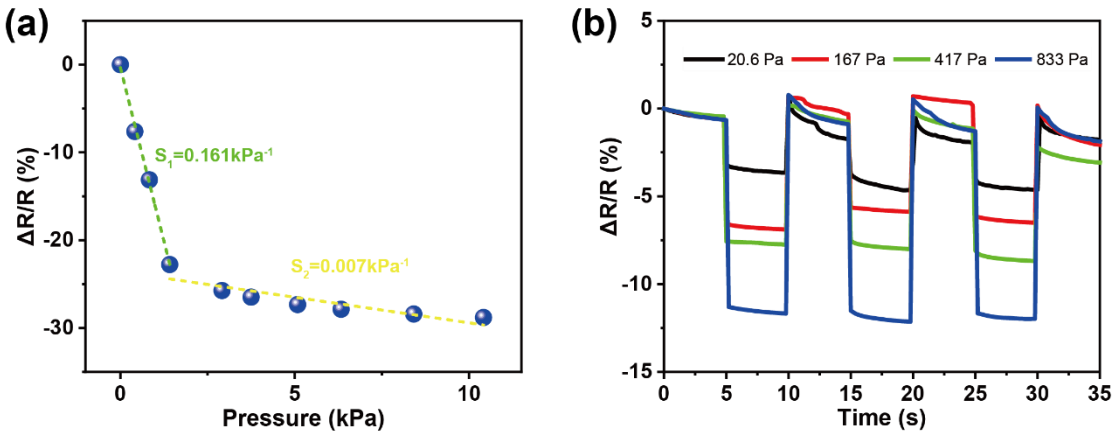

Figure 5.4 (a) The resistance changes of the AgNWs/rGO sensor without PS spheres under different pressure. (b) The resistance changes of the AgNWs/rGO sensor without PS spheres under different pressure.

To improve the device performance, PS spheres were involved between the AgNWs and rGO layers. The working principle is illustrated in Figure 5.3(c), that PS spheres are worked as insulators to separate the AgNWs layer from the rGO layer in a stress-free state, thus increasing the resistance variation of the device under pressure, which is also identified by SEM image of piezoresistive sensor with 40 μm PS spheres (Figure 5.3(d)).To further investigate the role of PS spheres, the pressure-response behaviour of the piezoresistive sensor with 2 μm, 20 μm and 40 μm diameters of PS spheres under 10kPa pressure was studied by varying the weight ratios, as shown in Figure 5.5. At a small weight ratio of 0.0025 wt%, the device with 2 μm PS spheres exhibits a high resistance variation of more than 50%, while the devices doped with larger spheres (20 μm and 40 μm) possess poor response. This is because the number of 20 μm and 40 μm spheres is less than the same weight of 2 μm spheres, so a very small number of spheres are sprayed on the AgNW layer at a small weight ratio. The distribution of PS spheres is shown in Figure 5.7. The variation in the resistance of the device increases with the increase of the weight ratio. At 0.025 wt%, the resistance change is 78% for the device with 40 μm spheres, 57% for the device with 20 μm spheres, and 70% for the device with 2 μm spheres which is the best performance for doping the 2 μm spheres. The device with 40 μm spheres at 0.25 wt% reaches the best performance that the average resistance change is about 95%. Further increasing the weight ratio, the device showed a decrease in the resistance change because there were too many spheres between the AgNW and rGO layers, covering almost the entire bottom layer. Therefore, fewer contact points are created between the two conductive layers under external forces. As a result, there is an optimal doping ratio for different sizes of PS spheres.

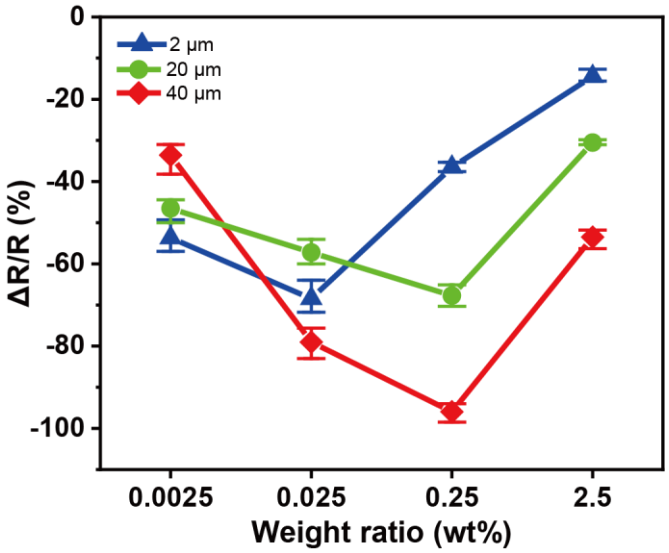

Figure 5.5 The resistance changes of the sensor with different diameters of PS spheres at 0.25 wt%,0.025 wt% and 0.0025 wt% under 10 kPa.

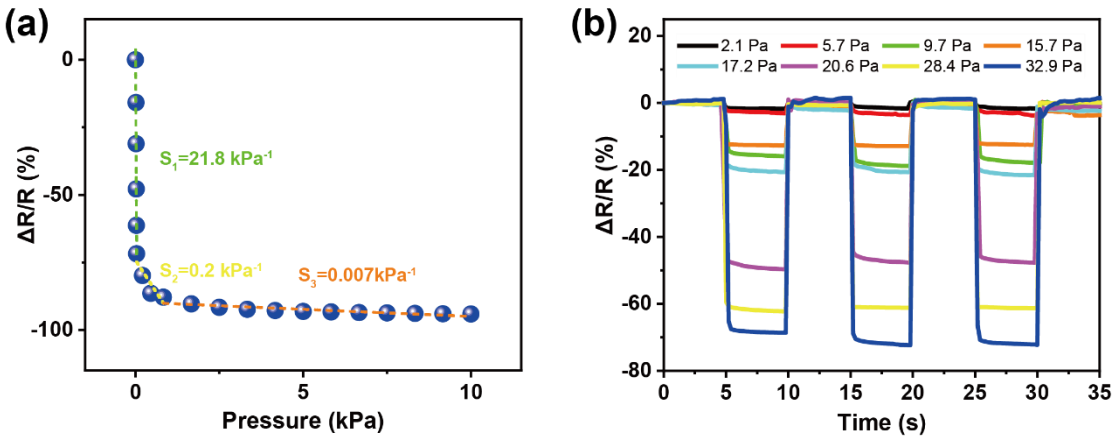

Figure 5.6 (a) The resistance changes of the sensor with 40 μm PS spheres at 0.25 wt% and the sensor without PS spheres under different pressure. (b) The resistance changes of the sensor with 40 μm PS spheres at 0.25 wt% under different pressure.

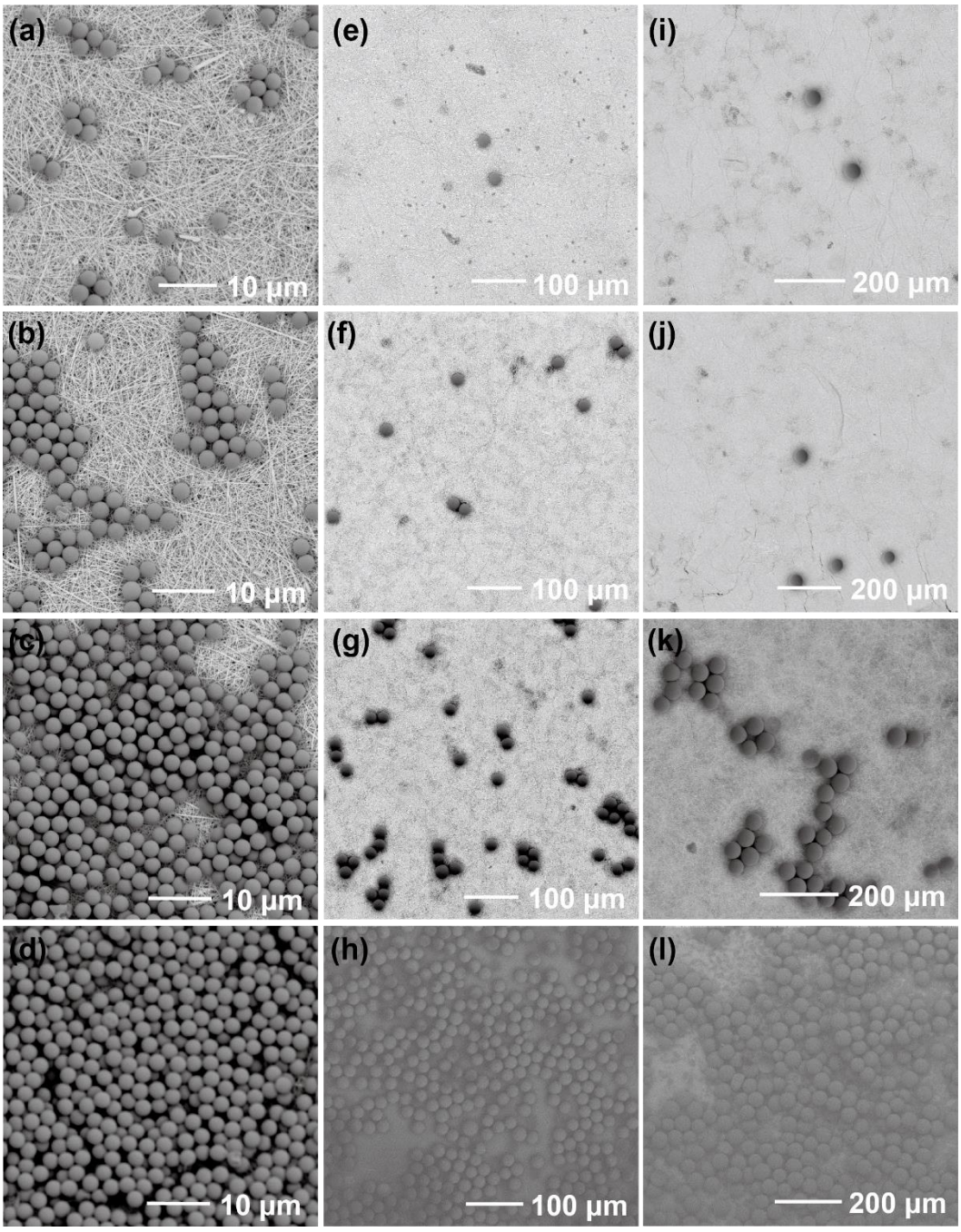

Figure 5.7 SEM images of (a) 2 μm PS spheres at 0.0025 wt%. (b) 2 μm PS spheres at 0.025 wt%. (c) 2 μm PS spheres at 0.25 wt%. (d) 2 μm PS spheres at 2.5 wt%. (e) 20 μm PS spheres at 0.0025 wt%. (f) 20 μm PS spheres at 0.025 wt%. (g) 20 μm PS spheres at 0.25 wt%. (h) 20 μm PS spheres at 2.5 wt%. (i) 40 μm PS spheres at 0.0025 wt%. (j) 40 μm PS spheres at 0.025 wt%. (k) 40 μm PS spheres at 0.25 wt%. (l) 40 μm PS spheres at 2.5 wt%.

To further investigate the pressure sensing performances of the device, Figure 5.6(a) shows the dependence of the resistance change of the device with 40 μm spheres at 0.25 wt% on various pressures. The pressure sensitivities were calculated by dividing the resistance response–pressure curves into three linear parts. The AgNW/PS/rGO device was sensitive to a low-pressure range, where the device presented a high sensitivity of 21.8 kPa^{-1} in the range of 0–33 Pa, which is more than 135 times higher than AgNW/rGO sensor. The pressure sensitivities of the device were 0.2 kPa^{-1} in the range of 33 Pa –833 Pa and 0.007 kPa^{-1} in the range of 833 Pa–10 kPa. The reduced sensitivity can be attributed to the contact between the top layer and the bottom layer gradually approaching saturation in the high-pressure range.

To further investigate the pressure response of the device in the low-pressure range, different pressure were applied on the device. In Figure 5.6(b), the resistance change increase in accordance with the increase of applied pressure, indicating the device is capable of distinguishing different levels of pressure. It is worth mentioning that the device can detect ultra-light weight. The resistance drops 1.7% when 2.1 Pa pressure applied on it. Moreover, the device shows a rapid response and recovery time of 162 ms in Figure 5.8(a). The device also shows excellent durability and stability during long-term operation. As shown in Figure 5.8(b), the change in resistance of the fabricated device remained fairly stable (only dropped by 1.38%) after 5000 cycles of continuous press-release process. The distribution of the PS spheres also observed before and after the durability test, as shown in Figure 5.9. The density of PS spheres on the AgNW layer decreased after the test, while some PS spheres were observed on the rGO layer. Thus, the PS spheres were not fixed on the AgNW layer. Indeed, they were also attached to the rGO layer when two layers connected by applying pressure.

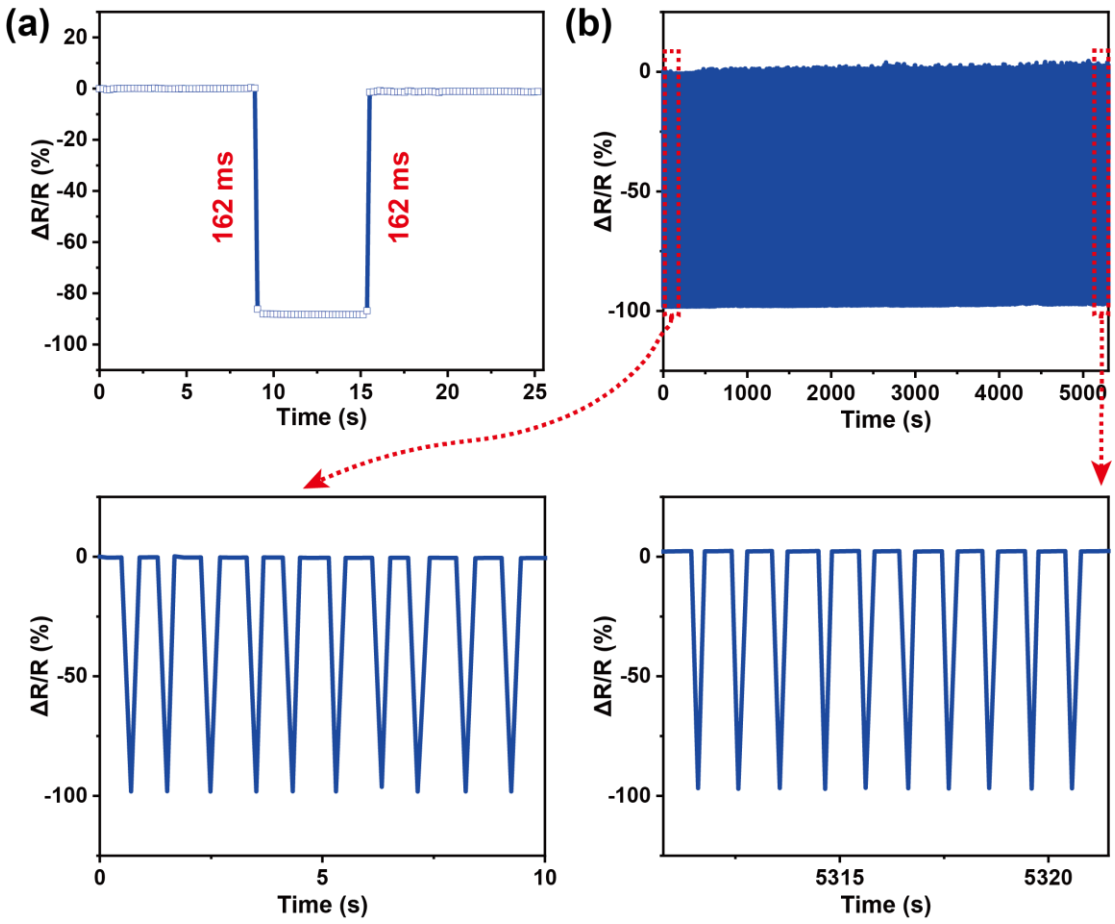

Figure 5.8 (a) The response and recovery time of the prepared sensor. (b) Test of the repeatability performance over 5000 cycles under 10 kPa.

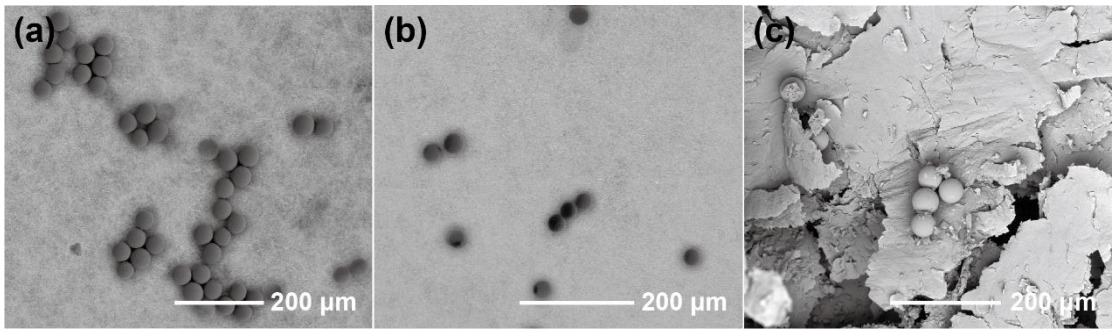

Figure 5.9 (a) The PS sphere on the AgNW layer before testing. (b) The PS spheres on the AgNW layer after testing. (c) The PS spheres on the rGO layer after testing.

Furthermore, the sensor's performance for changes in ambient temperature and humidity were studied. As shown in Figure 5.10(a), the resistance change decreased by 4% when temperature increased from 20 °C to 50 °C. As shown in Figure 5.10(b), when the relative humidity changed by about 30%, the resistance of the developed sensor remained stable. Thus, the temperature and humidity have little influence on the response of the sensor in comparison to the effects of pressure.

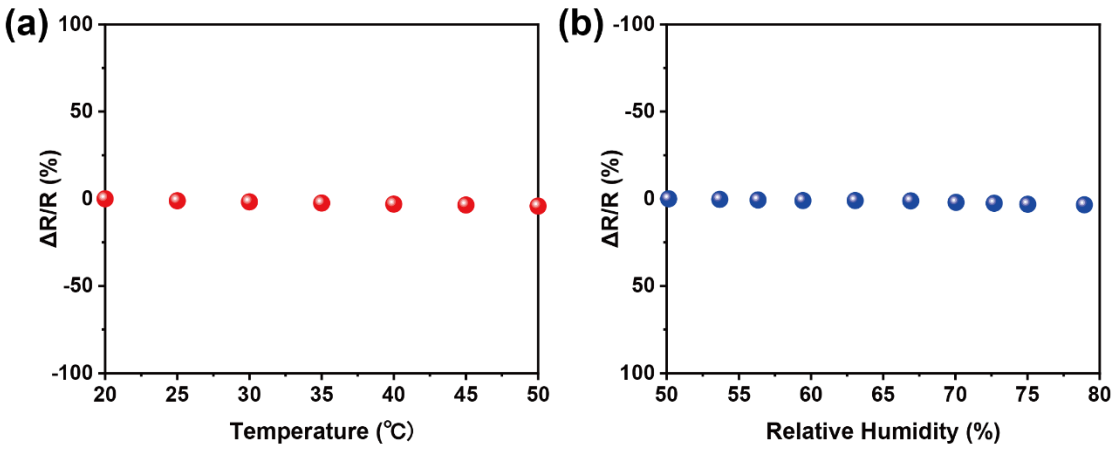

Figure 5.10 (a) The resistance value of the developed sensor under temperatures.The resistance change decreased by 0.04 when temperature increased from 20 °C to 50 °C. (b) The resistance value of the developed sensor under different humidity environments. The resistance of the developed sensor remained stable when the relative humidity changed by about 30%.

The device can also respond to different mechanical forces, such as compression and bending, as illustrated in Figure 5.11(a) and (b), indicating the multi-functionalities and versatilities of the device. The resistance response of the fabricated sensor before and after multiple bending (20 times, 50 times and 100 times) was tested, and the bending angle was larger than 90°. As shown in Figure 5.12, the resistance response of the sensor was stable, and the resistance change was about 87% before bending tests. After 20 times bending, the resistance response of the sensor fluctuated slightly

when pressure was applied. The initial resistance of the sensor was increased, while the resistance under pressure was almost unchanged. Thus, the resistance changes of the sensor increased after 20 bending times. The same situation also happened after the sensor bent 50 and 100 times, the signal fluctuations got bigger and bigger, and the initial resistance of the sensor also continually increased. It is because the rGO structure became porous after bending. Some connections between rGO fragments were broken, which resulted in the resistance of the rGO layer to increase. As shown in Figure 2(c), the initial resistance of the sensor relied on the rGO resistance. Therefore, the initial resistance of the sensor increased as the rGO resistance increased after bending.

Meantime, benefiting from the remarkable sensitivity and stability of the fabricated AgNW/PS/rGO sensor, it can be used as a wearable device for human motion detection. The device can be easily mounted on different body parts due to its small size, lightweight and excellent flexibility. As shown in Figure 5.11(c), the pressure sensor was placed on the finger to detect the finger-bending movements. Figure 5.11(d) illustrates the resistance response of the eye blinking. Moreover, the different wrist bending angles of 30°, 60° and 90°can be observed, and the resistance change was 38%, 50% and 88%, respectively. The results illustrate that the detected waveform positively correlates with muscle contraction intensity. When attaching the device to the human throat (Figure 5.11(f)), different throat movements are able distinguished based on the unique characteristic waveforms. Consequentially, the device shows attractive potential in the field of wearable applications.

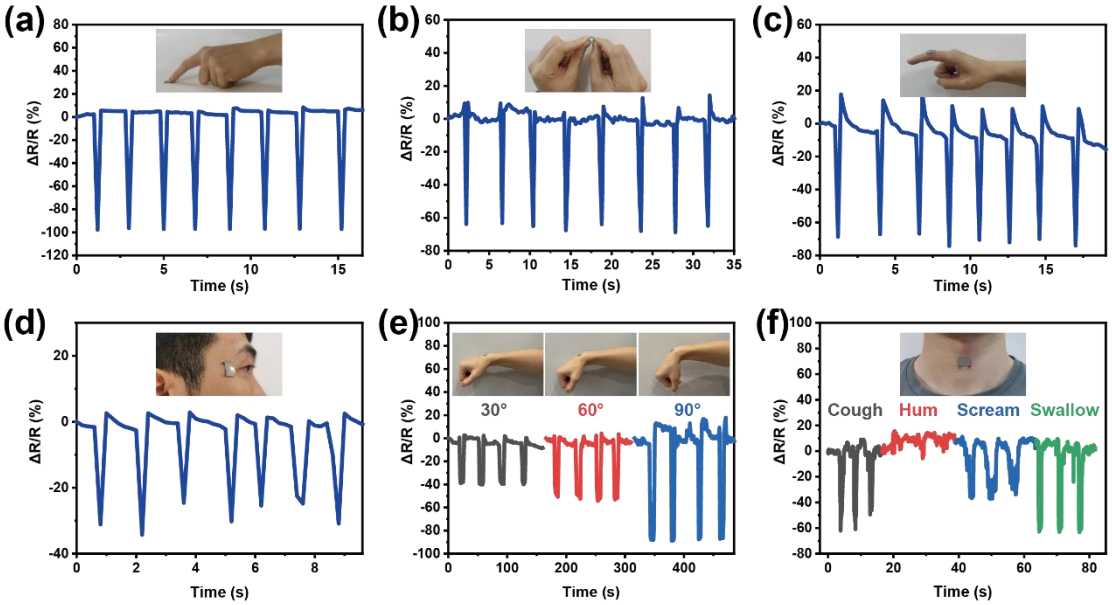

Figure 5.11 The prepared sensor was used to monitor different mechanical forces (a) compression and (b) bending, as well as various human body activities (c) finger movements, (d) eye blinking, (e) wrist flexion at different angles and (f) throat movements.

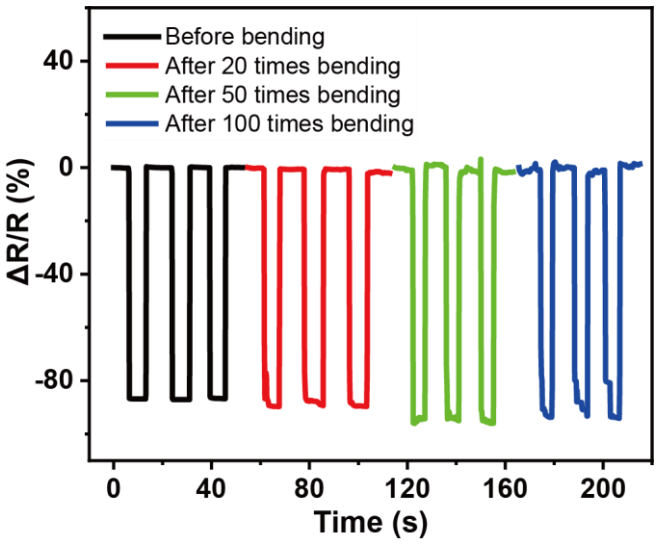

Figure 5.12 The resistance changes of the sensor before and after repeated bending.

5.4 Sensor-Machine Interface Design and Analysis

Due to the high sensitivity of the piezoresistive sensor in low pressure range, detection of small vibration and muscle motions are more suitable for this sensor. In this case, a speech recognition system was established based on the fabricated device to distinguish different pronunciations to help patients with communication. The system contains an ultra-sensitive flexible piezoresistive device, a microcontroller (Arduino Nano) with a Bluetooth module and a computer terminal. The device was attached to the throat of a participant to detect muscle movements during different pronunciations. The detected resistance data were transferred to the corresponding voltage readings through a voltage divider circuit. Then the readings were wirelessly transmitted to the computer terminal for post-processing.

A total of five words were collected, which are high frequency comes up in the health monitoring situation, including two monosyllabic words: "sick" and "help" and three disyllabic words "doctor", "patient", and "covid". The detection waveforms of the five words are shown in the Figure 5.13(a), and the corresponding peaks of the syllabic of each word can be seen clearly. For both monosyllabic words, the valley value of "help" is lower than that of "sick", which is probably attributed to the wider mouth opening when this word is pronounced, resulting in stronger laryngeal muscle stretching and contraction. Meanwhile, for disyllabic words, the waveforms contain two valleys according to the syllabic. The first valley of the "doctor" and "patient" is higher than the second one, while both valleys of "covid" are almost at the same level. This is because the shape of the mouth changes obviously for both syllabics of "covid" when pronouncing. Thus, the associated laryngeal muscle movement becomes

more pronounced. For post data-processing algorithm, a large amount of data was required. Therefore, the participant repeated each word 100 times to demonstrate reliability for a total of 500 times acquisition waveforms, in which 80% of the collected data are used as the training set and the remaining 20% as the test set.

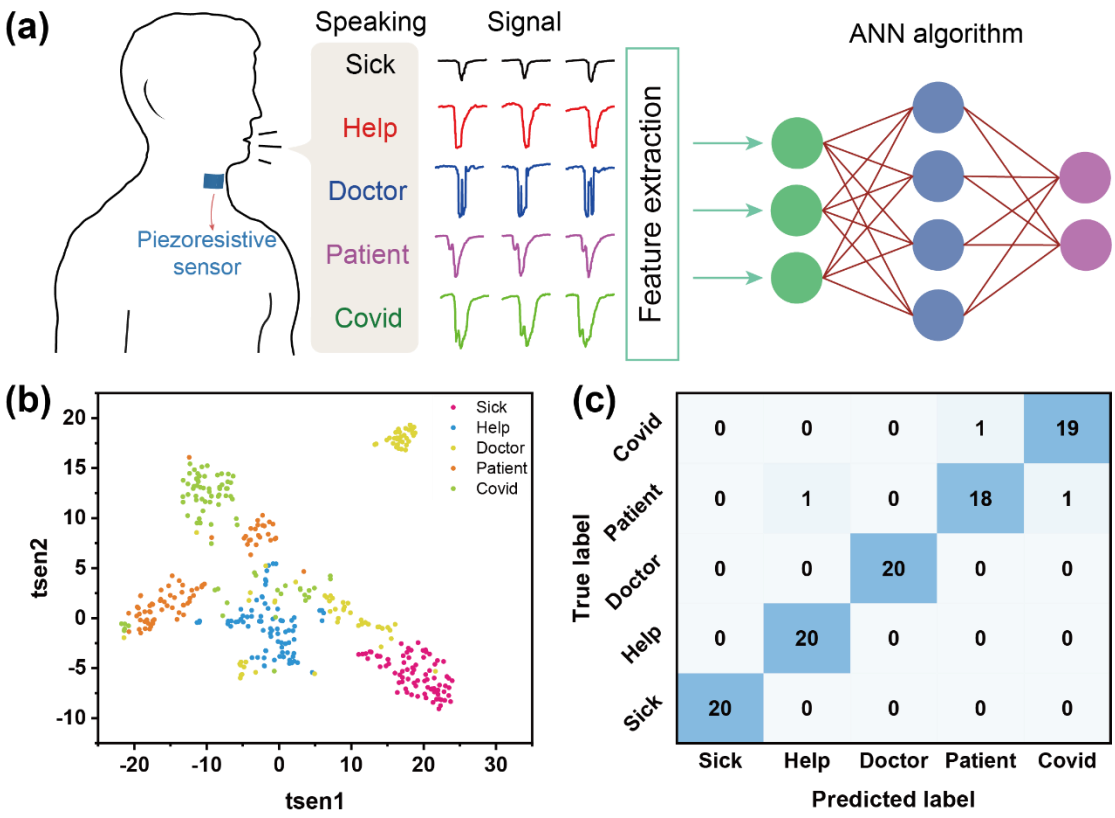

Figure 5.13 (a) Schematic diagram of the speech recognition process. (b) Cluster results of word signals. (c) Classification confusion matrix for 5 different pronunciations.

To classify the throat movements more precisely, an ANN deep learning algorithm was involved with good performance. The ANN network was constructed with three hidden layers, and each hidden layer had 10 neurons. More parameter settings of ANN can be found in Table 5.1, and the performance plot of the ANN mode is shown in Figure 5.14. Besides the collected signals, features including mean, minimum, peak

to peak, variance, percentiles, standard deviation as well as kurtosis, width and prominence of each curve are extracted from the time domain and also supplied to the classifier. To better understand the clustering performance of the dataset, t-distributed Stochastic Neighbour Embedding (t-SNE) is utilized to reduce the dimensionality, and the visualization results are shown in Figure 5.13(b). The classification accuracy reaches 96% for speech recognition by using the fabricated device. The confusion matrix of the prediction result is shown in Figure 5.13(c). The classifiers precisely separate two monosyllabic words from the others but are confused by " patient " and "covid".

Table 5.1 Parameters for the ANN training.

The number of hidden layers	3
The number of neurons in hidden layers	10 × 10 × 10
Nonlinear function of the three hidden layers	Symmetric sigmoid transfer function, Logarithmic sigmoid transfer function, Symmetric sigmoid transfer function
Training goal	10^{-5}
Training cycles	100

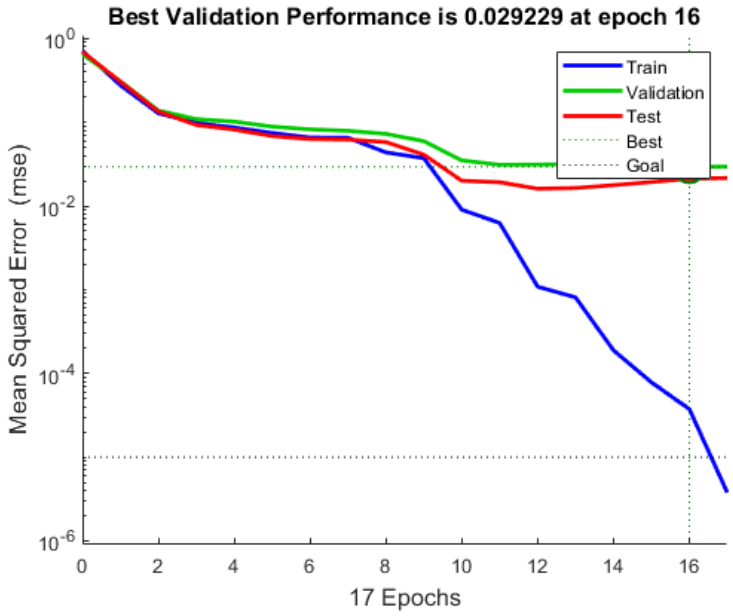

Figure 5.14 Training epoch of the ANN classifier.

5.5 Summary

In summary, a new type of piezoresistive sensor was fabricated using PS spheres as microstructures that were sandwiched between asymmetric layers of AgNW and rGO. An optimisation of the microsphere diameter and weight ratio resulted in an ultra-sensitive device in the low-pressure range (21.8 kPa^{-1}), which is more than 135 times better than the same device without PS spheres. Moreover, the prepared sensor exhibits fast response and recovery time properties (162 ms), ultralow detection limit (2.1 Pa) and excellent stability (>5000 loading/unloading cycles). These promising performance characteristics enable the sensor to monitor subtle human body activities and words as a wearable intelligent artificial throat to detect throat vibrations during speaking. The device successfully recognizes five different pronunciations by incorporating the deep learning algorithm with an accuracy of 96%, which further

demonstrates that it can be a valuable tool that facilitates communication for mute people.

A detailed comparison of our system with existing intelligent throats is shown in Table 5.2. In comparison with sensors, the flexible piezoresistive sensor with ANN algorithm developed in this chapter has achieved a higher classification result.

Table 5.2 Performance comparison of developed flexible sensor and similar intelligent throat products.

Sensor type	Number of sensors	Number of gestures	Algorithm	Accuracy	Flexible	Ref
Strain sensor	1	13	CNN	86.5%	Yes	[162]
Sound detector	1	2	CNN	76.7%	Yes	[107]
Strain sensor	1	15	LSTM	55%	Yes	[161]
Piezoresistive sensor	1	5	ANN	96%	Yes	This work

Chapter 6

Conclusions and Future Work

6.1 Conclusions

This thesis focuses on smart wearable devices based on electromechanical sensors to detect different human motions. Compared with traditional wearable applications with rigid sensors, the developed devices have advantages in comfortability by using the flexible sensors and they are “smarter” by combining with the ML algorithms.

This research has successfully developed three wearable applications to achieve human activities recognition. The thesis firstly introduces different types of pressure sensing techniques and provides an overview of current developments in materials and structures of wearable electromechanical sensors. Next, ML algorithms were also reviewed and the latest ML-assisted wearable pressure sensing systems with applications in terms of gesture recognition are highlighted.

Human hand is an attractive place that can convey rich information when human-

human interaction or human-machine interaction. In this case, piezoelectric sensors were used to detect finger motions since piezoelectric sensors are sensitive to dynamic stimuli. An array of six PZT ceramics were bounded on the human wrist to distinguish five fingers when tapping. Different ML algorithms (KNN, BT and SVM) were used to classify the collected data from sensors. The classification results of different ML algorithms are compared, and it is shown that the SVM algorithm achieved the best performance with 100% accuracy when dealing with extracted features.

Furthermore, to collect more information from the human hand, piezoresistive sensors were chosen to collect both static and dynamic information. Herein, a flake-sphere hybrid structure of rGO doped with PS spheres was fabricated to develop the highly sensitive, fast response and flexible piezoresistive sensor array, which is ultra-light (only 2.8 g) and demonstrates remarkable curved-surface conformability. The flexible wrist-worn device with a five-sensing array is used to measure pressure distribution around the wrist for accurate and comfortable hand gesture recognition. The intelligent wristband is able to classify 12 hand gestures with 96.33% accuracy for five participants using an ML algorithm. Furthermore, for demonstrating the practical applications of the proposed method, a real-time system was developed to control a robotic hand according to the classification results.

In addition, the thesis provides a new approach to achieving speech recognition based on the wearable device. In this case, a novel piezoresistive sensor is demonstrated, which consists of PS spheres as microstructures sandwiched between AgNWs and rGO layers. In fact, changes in the device’s conducting patterns were obtained by varying the weight ratio and size of the PS microspheres, which is a fast and convenient way to establish microstructures for improved sensitivity. The wearable

artificial throat device also exhibits high sensitivity, fast response time and ultralow intensity level detection. Moreover, the device's excellent mechanical-electrical performance allows it to detect subtle throat vibrations that can be converted into controllable sounds. In this case, an intelligent artificial throat was achieved by combining a deep learning algorithm with a highly flexible piezoresistive sensor to successfully recognize five different words (help, sick, patient, doctor and COVID) with an accuracy exceeding 96%.

6.2 Future Work

- Firstly, high performance and flexible electromechanical sensors are vital for future wearable electronics. Thus, novel materials, structures and manufacturing technologies should be developed to make the electromechanical sensor reliable and enduring in operation.

- Secondly, a multimodal sensing system can be realized by integrating various types of functional wearable sensors. Human motions are complex tasks that require multiple sensory elements rather than just one type. Each sensing technology has advantages and disadvantages. Thus it is possible to leverage the strengths of the sensors by integrating them. The fusion of various wearable sensors can acquire multimodal sensing data about temperature, pressure, pictures or optical information from the human body and the environment. This comprehensive information makes it possible to achieve robotic hand and skeletal myotubes.

- Thirdly, data processing of current studies is carried out on the computer after

sensor data transmitting wirelessly by the Bluetooth module. This out-sensor computation always spends extra time and energy to transmit the data. Therefore, in-sensor computing is highly required. Compared with transferring raw signals to an external computational device, local processing of collected data from wearables has the advantage of reducing the reaction delay and energy usage by decreasing the data transmission distance and the computing unit.

- Finally, widespread adoption of wearable technology is hindered by the duration time that they can be used without recharging. To ensure uninterrupted operation, wearable devices need a constant and battery less energy supply. Scavenging energy from the wearable's surroundings is, therefore, an essential step towards achieving genuinely autonomous and self-powered devices. Energy harvesting is a promising and efficient technique to generate electricity for powering wearable devices in response to body movements.

Reference

[1] E. Covi *et al.*, "Adaptive Extreme Edge Computing for Wearable Devices," *Frontiers in Neuroscience,* vol. 15, p. 611300, 2021-May-11 2021.

[2] *Wearable Technology Market Size, Share & Trends Analysis Report By Product (Head & Eyewear, Wristwear), By Application (Consumer Electronics, Healthcare), By Region (Asia Pacific, Europe), And Segment Forecasts, 2023 - 2030*. Available: https://www.grandviewresearch.com/industry-analysis/wearable-technology-market

[3] S. M. A. Iqbal, I. Mahgoub, E. Du, M. A. Leavitt, and W. Asghar, "Advances in healthcare wearable devices," *npj Flexible Electronics,* vol. 5, no. 1, p. 9, 2021/04/12 2021.

[4] S. Malwade *et al.*, "Mobile and wearable technologies in healthcare for the ageing population," *Computer Methods and Programs in Biomedicine,* vol. 161, pp. 233-237, 2018/07/01/ 2018.

[5] A. Papa, M. Mital, P. Pisano, and M. Del Giudice, "E-health and wellbeing monitoring using smart healthcare devices: An empirical investigation," *Technological Forecasting and Social Change,* vol. 153, p. 119226, 2020/04/01/ 2020.

[6] L. E. Romero, P. Chatterjee, and R. L. Armentano, "An IoT approach for integration of computational intelligence and wearable sensors for Parkinson's disease diagnosis and monitoring," *Health and Technology,* vol. 6, no. 3, pp. 167-172, 2016/11/01 2016.

[7] Y. Chu *et al.*, "Human Pulse Diagnosis for Medical Assessments Using a Wearable Piezoelectret Sensing System," *Advanced Functional Materials,* https://doi.org/10.1002/adfm.201803413 vol. 28, no. 40, p. 1803413, 2018/10/01 2018.

[8] J. V. Vaghasiya, C. C. Mayorga-Martinez, J. Vyskočil, and M. Pumera, "Black phosphorous-based human-machine communication interface," *Nature Communications,* vol. 14, no. 1, p. 2, 2023/01/03 2023.

[9] Q. Zhang *et al.*, "Flexible multifunctional platform based on piezoelectric acoustics for human–machine interaction and environmental perception," *Microsystems & Nanoengineering,* vol. 8, no. 1, p. 99, 2022/09/14 2022.

[10] H. Li, A. Shrestha, F. Fioranelli, J. Le Kernec, and H. Heidari, "FMCW radar and inertial sensing synergy for assisted living," *The Journal of Engineering,*

https://doi.org/10.1049/joe.2019.0558 vol. 2019, no. 20, pp. 6784-6789, 2019/10/01 2019.

[11] M. Zhu, T. He, and C. Lee, "Technologies toward next generation human machine interfaces: From machine learning enhanced tactile sensing to neuromorphic sensory systems," *Applied Physics Reviews,* vol. 7, no. 3, p. 031305, 2020/09/01 2020.

[12] Z. Zhang, F. Wen, Z. Sun, X. Guo, T. He, and C. Lee, "Artificial Intelligence-Enabled Sensing Technologies in the 5G/Internet of Things Era: From Virtual Reality/Augmented Reality to the Digital Twin," *Advanced Intelligent Systems,* https://doi.org/10.1002/aisy.202100228 vol. 4, no. 7, p. 2100228, 2022/07/01 2022.

[13] C. Ding and D. Tao, "Trunk-Branch Ensemble Convolutional Neural Networks for Video-Based Face Recognition," *IEEE Transactions on Pattern Analysis and Machine Intelligence,* vol. 40, no. 4, pp. 1002-1014, 2018.

[14] M. Wang, Y. D. Zhang, and G. Cui, "Human motion recognition exploiting radar with stacked recurrent neural network," *Digital Signal Processing,* vol. 87, pp. 125-131, 2019/04/01/ 2019.

[15] M. Wang, G. Cui, X. Yang, and L. Kong, "Human body and limb motion recognition via stacked gated recurrent units network," *IET Radar, Sonar & Navigation,* https://doi.org/10.1049/iet-rsn.2018.5054 vol. 12, no. 9, pp. 1046-1051, 2018/09/01 2018.

[16] M. Wang *et al.*, "Gesture recognition using a bioinspired learning architecture that integrates visual data with somatosensory data from stretchable sensors," *Nature Electronics,* vol. 3, no. 9, pp. 563-570, 2020/09/01 2020.

[17] C. C. Vu and J. Kim, "Highly elastic capacitive pressure sensor based on smart textiles for full-range human motion monitoring," *Sensors and Actuators A: Physical,* vol. 314, p. 112029, 2020/10/15/ 2020.

[18] M. H. Chowdhury *et al.*, "Estimating Blood Pressure from the Photoplethysmogram Signal and Demographic Features Using Machine Learning Techniques," *Sensors*, vol. 20, no. 11. doi: 10.3390/s20113127

[19] D. Lei *et al.*, "Roles of MXene in Pressure Sensing: Preparation, Composite Structure Design, and Mechanism," *Advanced Materials,* https://doi.org/10.1002/adma.202110608 vol. 34, no. 52, p. 2110608, 2022/12/01 2022.

[20] D. Wang *et al.*, "Biomimetic, biocompatible and robust silk Fibroin-MXene film with stable 3D cross-link structure for flexible pressure sensors," *Nano Energy,* vol. 78, p. 105252, 2020/12/01/ 2020.

[21] Y. Jung, J. Choi, W. Lee, J. S. Ko, I. Park, and H. Cho, "Irregular Microdome Structure-Based Sensitive Pressure Sensor Using Internal Popping of Microspheres," *Advanced Functional Materials,* https://doi.org/10.1002/adfm.202201147 vol. 32, no. 27, p. 2201147, 2022/07/01 2022.

[22] J. Heikenfeld *et al.*, "Wearable sensors: modalities, challenges, and prospects," *Lab on a Chip,* vol. 18, no. 2, pp. 217-248, 2018.

[23] H. P. Phan, D. V. Dao, K. Nakamura, S. Dimitrijev, and N. T. Nguyen, "The Piezoresistive Effect of SiC for MEMS Sensors at High Temperatures: A Review," *Journal of Microelectromechanical Systems,* vol. 24, no. 6, pp. 1663-1677, 2015.

[24] Y. Hou, D. Wang, X.-M. Zhang, H. Zhao, J.-W. Zha, and Z.-M. Dang, "Positive piezoresistive behavior of electrically conductive alkyl-functionalized graphene/polydimethylsilicone nanocomposites," *Journal of Materials Chemistry C,* 10.1039/C2TC00114D vol. 1, no. 3, pp. 515-521, 2013.

[25] D. Niu *et al.*, "Graphene-elastomer nanocomposites based flexible piezoresistive sensors for strain and pressure detection," *Materials Research Bulletin,* vol. 102, pp. 92-99, 2018/06/01/ 2018.

[26] D. Lee, H. Lee, Y. Jeong, Y. Ahn, G. Nam, and Y. Lee, "Highly Sensitive, Transparent, and Durable Pressure Sensors Based on Sea-Urchin Shaped Metal Nanoparticles," *Advanced Materials,* https://doi.org/10.1002/adma.201603526 vol. 28, no. 42, pp. 9364-9369, 2016/11/01 2016.

[27] Q. Zhou, T. Chen, S. Cao, X. Xia, Y. Bi, and X. Xiao, "A novel flexible piezoresistive pressure sensor based on PVDF/PVA-CNTs electrospun composite film," *Applied Physics A,* vol. 127, no. 9, p. 667, 2021/08/13 2021.

[28] L. Zhao, B. Jiang, and Y. Huang, "Self-healable polysiloxane/graphene nanocomposite and its application in pressure sensor," *Journal of Materials Science,* vol. 54, no. 7, pp. 5472-5483, 2019/04/01 2019.

[29] J. H. Oh, J. Y. Woo, S. Jo, and C.-S. Han, "Pressure-conductive rubber sensor based on liquid-metal-PDMS composite," *Sensors and Actuators A: Physical,* vol. 299, p. 111610,

2019/11/01/ 2019.

[30] J. Li, L. Fang, B. Sun, X. Li, and S. H. Kang, "Review—Recent Progress in Flexible and Stretchable Piezoresistive Sensors and Their Applications," *Journal of The Electrochemical Society,* vol. 167, no. 3, p. 037561, 2020/01/02 2020.

[31] F. He, X. You, W. Wang, T. Bai, G. Xue, and M. Ye, "Recent Progress in Flexible Microstructural Pressure Sensors toward Human–Machine Interaction and Healthcare Applications," *Small Methods,* https://doi.org/10.1002/smtd.202001041 vol. 5, no. 3, p. 2001041, 2021/03/01 2021.

[32] J. Park *et al.*, "Giant Tunneling Piezoresistance of Composite Elastomers with Interlocked Microdome Arrays for Ultrasensitive and Multimodal Electronic Skins," *ACS Nano,* vol. 8, no. 5, pp. 4689-4697, 2014/05/27 2014.

[33] M. Wang, Y. Qiu, J. Jia, C. Wang, J. Deng, and K. Pan, "Wavelength-Gradient Graphene Films for Pressure-Sensitive Sensors," *Advanced Materials Technologies,* https://doi.org/10.1002/admt.201800363 vol. 4, no. 1, p. 1800363, 2019/01/01 2019.

[34] Q. Shao *et al.*, "High-Performance and Tailorable Pressure Sensor Based on Ultrathin Conductive Polymer Film," *Small,* https://doi.org/10.1002/smll.201303601 vol. 10, no. 8, pp. 1466-1472, 2014/04/01 2014.

[35] K. Sun *et al.*, "Hybrid Architectures of Heterogeneous Carbon Nanotube Composite Microstructures Enable Multiaxial Strain Perception with High Sensitivity and Ultrabroad Sensing Range," *Small,* https://doi.org/10.1002/smll.201803411 vol. 14, no. 52, p. 1803411, 2018/12/01 2018.

[36] C. Pang *et al.*, "A flexible and highly sensitive strain-gauge sensor using reversible interlocking of nanofibres," *Nature Materials,* vol. 11, no. 9, pp. 795-801, 2012/09/01 2012.

[37] C.-L. Choong *et al.*, "Highly Stretchable Resistive Pressure Sensors Using a Conductive Elastomeric Composite on a Micropyramid Array," *Advanced Materials,* https://doi.org/10.1002/adma.201305182 vol. 26, no. 21, pp. 3451-3458, 2014/06/01 2014.

[38] B. Zhu *et al.*, "Microstructured Graphene Arrays for Highly Sensitive Flexible Tactile Sensors," *Small,* vol. 10, no. 18, pp. 3625-3631, 2014/09/01 2014.

[39] P. Nie *et al.*, "High-Performance Piezoresistive Electronic Skin with Bionic Hierarchical Microstructure and Microcracks," *ACS Applied Materials & Interfaces,* vol. 9, no. 17, pp. 14911-14919, 2017/05/03 2017.

[40] Y. Wei, S. Chen, Y. Lin, Z. Yang, and L. Liu, "Cu–Ag core–shell nanowires for electronic skin with a petal molded microstructure," *Journal of Materials Chemistry C,* 10.1039/C5TC01723H vol. 3, no. 37, pp. 9594-9602, 2015.

[41] B. Su, S. Gong, Z. Ma, L. W. Yap, and W. Cheng, "Mimosa-Inspired Design of a Flexible Pressure Sensor with Touch Sensitivity," *Small,* vol. 11, no. 16, pp. 1886-1891, 2015.

[42] T. Sun, L. Feng, X. Gao, and L. Jiang, "Bioinspired Surfaces with Special Wettability," *Accounts of Chemical Research,* vol. 38, no. 8, pp. 644-652, 2005/08/01 2005.

[43] Z. Tang, S. Jia, C. Zhou, and B. Li, "3D Printing of Highly Sensitive and Large-Measurement-Range Flexible Pressure Sensors with a Positive Piezoresistive Effect," *ACS Applied Materials & Interfaces,* vol. 12, no. 25, pp. 28669-28680, 2020/06/24 2020.

[44] H.-B. Yao *et al.*, "A Flexible and Highly Pressure-Sensitive Graphene–Polyurethane Sponge Based on Fractured Microstructure Design," *Advanced Materials,* https://doi.org/10.1002/adma.201303041 vol. 25, no. 46, pp. 6692-6698, 2013/12/01 2013.

[45] A. Tewari, S. Gandla, S. Bohm, C. R. McNeill, and D. Gupta, "Highly Exfoliated MWNT–rGO Ink-Wrapped Polyurethane Foam for Piezoresistive Pressure Sensor Applications," *ACS Applied Materials & Interfaces,* vol. 10, no. 6, pp. 5185-5195, 2018/02/14 2018.

[46] Y.-h. Wu *et al.*, "Channel Crack-Designed Gold@PU Sponge for Highly Elastic Piezoresistive Sensor with Excellent Detectability," *ACS Applied Materials & Interfaces,* vol. 9, no. 23, pp. 20098-20105, 2017/06/14 2017.

[47] X. Wu, Y. Han, X. Zhang, Z. Zhou, and C. Lu, "Large-Area Compliant, Low-Cost, and Versatile Pressure-Sensing Platform Based on Microcrack-Designed Carbon Black@Polyurethane Sponge for Human–Machine Interfacing," *Advanced Functional Materials,* https://doi.org/10.1002/adfm.201601995 vol. 26, no. 34, pp. 6246-6256, 2016/09/01 2016.

[48] Y. Ma *et al.*, "3D Synergistical MXene/Reduced Graphene Oxide Aerogel for a Piezoresistive Sensor," *ACS Nano,* vol. 12, no. 4, pp. 3209-3216, 2018/04/24 2018.

[49] H. Zhuo *et al.*, "A carbon aerogel with super mechanical and sensing performances for wearable piezoresistive sensors," *Journal of Materials Chemistry A,* 10.1039/C9TA00596J vol. 7, no. 14, pp. 8092-8100, 2019.

[50] J. Duan, X. Liang, J. Guo, K. Zhu, and L. Zhang, "Ultra-Stretchable and Force-Sensitive Hydrogels Reinforced with Chitosan Microspheres Embedded in Polymer Networks," *Advanced Materials,* https://doi.org/10.1002/adma.201602126 vol. 28, no. 36, pp. 8037-8044, 2016/09/01 2016.

[51] K. Uchino, *Advanced piezoelectric materials: Science and technology*. Woodhead Publishing, 2017.

[52] T. Hehn, Y. Manoli, and SpringerLink, *CMOS circuits for piezoelectric energy harvesters: efficient power extraction, interface modeling and loss analysis* (no. Book, Whole). Dordrecht: Springer, 2014.

[53] J. Feenstra, J. Granstrom, and H. Sodano, "Energy harvesting through a backpack employing a mechanically amplified piezoelectric stack," *Mechanical Systems and Signal Processing,* vol. 22, no. 3, pp. 721-734, 2008/04/01/ 2008.

[54] Q. Yang *et al.*, "Lead-free (Na0.83K0.17)0.5Bi0.5TiO3 nanofibers for wearable piezoelectric nanogenerators," *Journal of Alloys and Compounds,* vol. 688, pp. 1066-1071, 2016/12/15/ 2016.

[55] M. Pozzi and M. Zhu, "Plucked piezoelectric bimorphs for knee-joint energy harvesting: modelling and experimental validation," *Smart Materials and Structures,* vol. 20, no. 5, p. 055007, 2011/04/06 2011.

[56] R. Meier, N. Kelly, O. Almog, and P. Chiang, "A piezoelectric energy-harvesting shoe system for podiatric sensing," in *2014 36th Annual International Conference of the IEEE Engineering in Medicine and Biology Society*, 2014, pp. 622-625.

[57] K. Uchino and T. J. F. Ishii, "Energy flow analysis in piezoelectric energy harvesting systems," vol. 400, no. 1, pp. 305-320, 2010.

[58] C. R. Bowen, V. Y. Topolov, and H. A. Kim, *Modern piezoelectric energy-harvesting materials*. Springer, 2016.

[59] J. Tichý, J. Erhart, E. Kittinger, and J. Privratska, *Fundamentals of piezoelectric sensorics: mechanical, dielectric, and thermodynamical properties of piezoelectric materials*.

Springer Science & Business Media, 2010.

[60] N. Gogoi, Z. Yu, Y. Qin, J. Kirchner, and G. Fischer, "Insole Gait Acquisition System Based on Wearable Sensors," *Engineering Proceedings*, vol. 10, no. 1. doi: 10.3390/ecsa-8-11275

[61] R. Booth and P. Goldsmith, "A Wrist-Worn Piezoelectric Sensor Array for Gesture Input," *Journal of Medical and Biological Engineering,* vol. 38, no. 2, pp. 284-295, 2018/04/01 2018.

[62] Z. Yi, H. Yang, Y. Tian, X. Dong, J. Liu, and B. Yang, "Self-Powered Force Sensor Based on Thinned Bulk PZT for Real-Time Cutaneous Activities Monitoring," *IEEE Electron Device Letters,* vol. 39, no. 8, pp. 1226-1229, 2018.

[63] W.-S. Jung *et al.*, "Powerful curved piezoelectric generator for wearable applications," *Nano Energy,* vol. 13, pp. 174-181, 2015/04/01/ 2015.

[64] C. K. Jeong, C. Baek, A. I. Kingon, K.-I. Park, and S.-H. Kim, "Lead-Free Perovskite Nanowire-Employed Piezopolymer for Highly Efficient Flexible Nanocomposite Energy Harvester," *Small,* vol. 14, no. 19, p. 1704022, 2018.

[65] C. Gao, Z. Long, T. Zhong, S. Liang, and L. Xing, "A self-powered intelligent glove for real-time human-machine gesture interaction based on piezoelectric effect of T-ZnO/PVDF film," *Journal of Physics D: Applied Physics,* vol. 55, no. 19, p. 194004, 2022/02/16 2022.

[66] C. Baek *et al.*, "A flexible energy harvester based on a lead-free and piezoelectric BCTZ nanoparticle–polymer composite," *Nanoscale,* vol. 8, no. 40, pp. 17632-17638, 2016.

[67] M. Renaud, P. Fiorini, R. van Schaijk, and C. van Hoof, "Harvesting energy from the motion of human limbs: the design and analysis of an impact-based piezoelectric generator," *Smart Materials and Structures,* vol. 18, no. 3, p. 035001, 2009/01/27 2009.

[68] M. A. Halim and J. Y. Park, "Piezoelectric energy harvester using impact-driven flexible side-walls for human-limb motion," *Microsystem Technologies,* vol. 24, no. 5, pp. 2099-2107, 2018/05/01 2018.

[69] F. Guido, A. Qualtieri, L. Algieri, E. D. Lemma, M. De Vittorio, and M. T. Todaro, "AlN-based flexible piezoelectric skin for energy harvesting from human motion," *Microelectronic Engineering,* vol. 159, pp. 174-178, 2016/06/15/ 2016.

[70] K. C. Pradel, W. Wu, Y. Ding, and Z. L. Wang, "Solution-Derived ZnO Homojunction Nanowire Films on Wearable Substrates for Energy Conversion and Self-Powered Gesture Recognition," *Nano Letters,* vol. 14, no. 12, pp. 6897-6905, 2014/12/10 2014.

[71] Y. Cha, J. Hong, J. Lee, J.-M. Park, and K. Kim, "Flexible Piezoelectric Energy Harvesting from Mouse Click Motions," *Sensors,* vol. 16, no. 7, p. 1045, 2016.

[72] Z. He *et al.*, "Piezoelectric-Driven Self-Powered Patterned Electrochromic Supercapacitor for Human Motion Energy Harvesting," *ACS Sustainable Chemistry & Engineering,* vol. 7, no. 1, pp. 1745-1752, 2019/01/07 2019.

[73] B. Saravanakumar, S. Soyoon, and S.-J. Kim, "Self-Powered pH Sensor Based on a Flexible Organic–Inorganic Hybrid Composite Nanogenerator," *ACS Applied Materials & Interfaces,* vol. 6, no. 16, pp. 13716-13723, 2014/08/27 2014.

[74] Y. Bai *et al.*, "Investigation of a cantilever structured piezoelectric energy harvester used for wearable devices with random vibration input," *Mechanical Systems and Signal Processing,* vol. 106, pp. 303-318, 2018/06/01/ 2018.

[75] B. Shi *et al.*, "Body-Integrated Self-Powered System for Wearable and Implantable Applications," *ACS Nano,* vol. 13, no. 5, pp. 6017-6024, 2019/05/28 2019.

[76] D. Jiang, B. Shi, H. Ouyang, Y. Fan, Z. L. Wang, and Z. Li, "Emerging Implantable Energy Harvesters and Self-Powered Implantable Medical Electronics," *ACS Nano,* vol. 14, no. 6, pp. 6436-6448, 2020/06/23 2020.

[77] Z. L. Wang, "Triboelectric nanogenerators as new energy technology and self-powered sensors–Principles, problems and perspectives," *Faraday discussions,* vol. 176, pp. 447-458, 2015.

[78] F.-R. Fan, Z.-Q. Tian, and Z. Lin Wang, "Flexible triboelectric generator," *Nano Energy,* vol. 1, no. 2, pp. 328-334, 2012/03/01/ 2012.

[79] H. Ouyang *et al.*, "Self-Powered Pulse Sensor for Antidiastole of Cardiovascular Disease," *Advanced Materials,* vol. 29, no. 40, p. 1703456, 2017.

[80] H. Ouyang *et al.*, "Symbiotic cardiac pacemaker," *Nature Communications,* vol. 10, no. 1, p. 1821, 2019/04/23 2019.

[81] Y. Han *et al.*, "Self-powered gait pattern-based identity recognition by a soft and

stretchable triboelectric band," *Nano Energy,* vol. 56, pp. 516-523, 2019/02/01/ 2019.

[82] H. Wang *et al.*, "Flexible capacitive pressure sensors for wearable electronics," *Journal of Materials Chemistry C,* 10.1039/D1TC05304C vol. 10, no. 5, pp. 1594-1605, 2022.

[83] T. Li *et al.*, "Flexible Capacitive Tactile Sensor Based on Micropatterned Dielectric Layer," *Small,* https://doi.org/10.1002/smll.201600760 vol. 12, no. 36, pp. 5042-5048, 2016/09/01 2016.

[84] F. Yi *et al.*, "A highly shape-adaptive, stretchable design based on conductive liquid for energy harvesting and self-powered biomechanical monitoring," *Science Advances,* vol. 2, no. 6, p. e1501624.

[85] L. Y. W. Loh, U. Gupta, Y. Wang, C. C. Foo, J. Zhu, and W. F. Lu, "3D Printed Metamaterial Capacitive Sensing Array for Universal Jamming Gripper and Human Joint Wearables," *Advanced Engineering Materials,* https://doi.org/10.1002/adem.202001082 vol. 23, no. 5, p. 2001082, 2021/05/01 2021.

[86] X. Pu *et al.*, "Ultrastretchable, transparent triboelectric nanogenerator as electronic skin for biomechanical energy harvesting and tactile sensing," *Science Advances,* vol. 3, no. 5, p. e1700015.

[87] T. Yao *et al.*, "Highly sensitive capacitive flexible 3D-force tactile sensors for robotic grasping and manipulation," *Journal of Physics D: Applied Physics,* vol. 53, no. 44, p. 445109, 2020/08/10 2020.

[88] F. Cai *et al.*, "Ultrasensitive, passive and wearable sensors for monitoring human muscle motion and physiological signals," *Biosensors and Bioelectronics,* vol. 77, pp. 907-913, 2016/03/15/ 2016.

[89] Y. Geng *et al.*, "A high-sensitive wearable sensor based on conductive polymer composites for body temperature monitoring," *Composites Part A: Applied Science and Manufacturing,* vol. 163, p. 107269, 2022/12/01/ 2022.

[90] B. A. Kuzubasoglu, E. Sayar, C. Cochrane, V. Koncar, and S. K. Bahadir, "Wearable temperature sensor for human body temperature detection," *Journal of Materials Science: Materials in Electronics,* vol. 32, no. 4, pp. 4784-4797, 2021/02/01 2021.

[91] P. Pirovano *et al.*, "A wearable sensor for the detection of sodium and potassium in human sweat during exercise," *Talanta,* vol. 219, p. 121145, 2020/11/01/ 2020.

[92] D. R. Seshadri *et al.*, "Wearable sensors for monitoring the physiological and biochemical profile of the athlete," *npj Digital Medicine,* vol. 2, no. 1, p. 72, 2019/07/22 2019.

[93] L. Li, S. Jiang, P. B. Shull, and G. Gu, "SkinGest: artificial skin for gesture recognition via filmy stretchable strain sensors," *Advanced Robotics,* vol. 32, no. 21, pp. 1112-1121, 2018 2018.

[94] A. Rattanasak *et al.*, "Real-Time Gait Phase Detection Using Wearable Sensors for Transtibial Prosthesis Based on a kNN Algorithm," *Sensors*, vol. 22, no. 11, p. 4242. doi: 10.3390/s22114242

[95] Y. Su, K. Ma, X. Mao, M. Liu, and X. Zhang, "Highly Compressible and Sensitive Flexible Piezoresistive Pressure Sensor Based on MWCNTs/Ti3C2Tx MXene @ Melamine Foam for Human Gesture Monitoring and Recognition," *Nanomaterials*, vol. 12, no. 13. doi: 10.3390/nano12132225

[96] G. M. Jeong, P. H. Truong, and S. I. Choi, "Classification of Three Types of Walking Activities Regarding Stairs Using Plantar Pressure Sensors," *IEEE Sensors Journal,* vol. 17, no. 9, pp. 2638-2639, 2017.

[97] T. Zhang, G. D. Fulk, W. Tang, and E. S. Sazonov, "Using decision trees to measure activities in people with stroke," in *2013 35th Annual International Conference of the IEEE Engineering in Medicine and Biology Society (EMBC)*, 2013, pp. 6337-6340.

[98] P. Xanthopoulos, P. M. Pardalos, and T. B. Trafalis, "Linear Discriminant Analysis," in *Robust Data Mining*, P. Xanthopoulos, P. M. Pardalos, and T. B. Trafalis, Eds. New York, NY: Springer New York, 2013, pp. 27-33.

[99] P. Tan *et al.*, "Self-Powered Gesture Recognition Wristband Enabled by Machine Learning for Full Keyboard and Multicommand Input," *Advanced Materials,* https://doi.org/10.1002/adma.202200793 vol. 34, no. 21, p. 2200793, 2022/05/01 2022.

[100] X. Liang, R. Ghannam, and H. Heidari, "Wrist-Worn Gesture Sensing With Wearable Intelligence," *IEEE Sensors Journal,* vol. 19, no. 3, pp. 1082-1090, 2019.

[101] Z. Sun, M. Zhu, X. Shan, and C. Lee, "Augmented tactile-perception and haptic-feedback rings as human-machine interfaces aiming for immersive interactions," *Nature Communications,* vol. 13, no. 1, p. 5224, 2022/09/05 2022.

[102] O. I. Abiodun *et al.*, "Comprehensive Review of Artificial Neural Network Applications to

Pattern Recognition," *IEEE Access,* vol. 7, pp. 158820-158846, 2019.

[103] Y. Pang *et al.*, "Skin-inspired textile-based tactile sensors enable multifunctional sensing of wearables and soft robots," *Nano Energy,* vol. 96, p. 107137, 2022/06/01/ 2022.

[104] Q. Zhang *et al.*, "Wearable Triboelectric Sensors Enabled Gait Analysis and Waist Motion Capture for IoT-Based Smart Healthcare Applications," *Advanced Science,* https://doi.org/10.1002/advs.202103694 vol. 9, no. 4, p. 2103694, 2022/02/01 2022.

[105] F. Wen, Z. Zhang, T. He, and C. Lee, "AI enabled sign language recognition and VR space bidirectional communication using triboelectric smart glove," *Nature Communications,* vol. 12, no. 1, p. 5378, 2021/09/10 2021.

[106] S. Sundaram, P. Kellnhofer, Y. Li, J.-Y. Zhu, A. Torralba, and W. Matusik, "Learning the signatures of the human grasp using a scalable tactile glove," *Nature,* vol. 569, no. 7758, pp. 698-702, 2019/05/01 2019.

[107] Y. Jin *et al.*, "Deep-Learning-Enabled MXene-Based Artificial Throat: Toward Sound Detection and Speech Recognition," *Advanced Materials Technologies,* https://doi.org/10.1002/admt.202000262 vol. 5, no. 9, p. 2000262, 2020/09/01 2020.

[108] Z. Zhang *et al.*, "Deep learning-enabled triboelectric smart socks for IoT-based gait analysis and VR applications," *npj Flexible Electronics,* vol. 4, no. 1, p. 29, 2020/10/26 2020.

[109] Y. Lu *et al.*, "Decoding lip language using triboelectric sensors with deep learning," *Nature Communications,* vol. 13, no. 1, p. 1401, 2022/03/17 2022.

[110] S.-T. Antoni, C. Sonnenburg, T. Saathoff, and A. Schlaefer, "Feasibility of interactive gesture control of a robotic microscope," *Current Directions in Biomedical Engineering,* vol. 1, no. 1, pp. 164-167, 2015.

[111] R. Huang, C. Harris-Adamson, D. Odell, and D. Rempel, "Design of finger gestures for locomotion in virtual reality," *Virtual Reality & Intelligent Hardware,* vol. 1, no. 1, pp. 1-9, 2019/02/01/ 2019.

[112] D. Sim, Y. Baek, M. Cho, S. Park, A. S. M. S. Sagar, and H. S. Kim, "Low-Latency Haptic Open Glove for Immersive Virtual Reality Interaction," *Sensors*, vol. 21, no. 11. doi: 10.3390/s21113682

[113] !!! INVALID CITATION !!! [1-4].

[114] Y. Sun *et al.*, "Gesture Recognition Based on Kinect and sEMG Signal Fusion," *Mobile Networks and Applications,* vol. 23, no. 4, pp. 797-805, 2018/08/01 2018.

[115] S. Bhushan, M. Alshehri, I. Keshta, A. K. Chakraverti, J. Rajpurohit, and A. Abugabah, "An Experimental Analysis of Various Machine Learning Algorithms for Hand Gesture Recognition," *Electronics*, vol. 11, no. 6. doi: 10.3390/electronics11060968

[116] Q. Chen, N. D. Georganas, and E. M. Petriu, "Hand Gesture Recognition Using Haar-Like Features and a Stochastic Context-Free Grammar," *IEEE Transactions on Instrumentation and Measurement,* vol. 57, no. 8, pp. 1562-1571, 2008.

[117] G. Ogris, M. Kreil, and P. Lukowicz, "Using FSR based muscule activity monitoring to recognize manipulative arm gestures," in *2007 11th IEEE International Symposium on Wearable Computers*, 2007, pp. 45-48.

[118] B. Wan, R. Wu, K. Zhang, and L. Liu, "A new subtle hand gestures recognition algorithm based on EMG and FSR," in *2017 IEEE 21st International Conference on Computer Supported Cooperative Work in Design (CSCWD)*, 2017, pp. 127-132.

[119] M. B. I. Reaz, M. S. Hussain, and F. Mohd-Yasin, "Techniques of EMG signal analysis: detection, processing, classification and applications," *Biological Procedures Online,* vol. 8, no. 1, pp. 11-35, 2006/12/01 2006.

[120] Y. Dong, J. Liu, and W. Yan, "Dynamic Hand Gesture Recognition Based on Signals From Specialized Data Glove and Deep Learning Algorithms," *IEEE Transactions on Instrumentation and Measurement,* vol. 70, pp. 1-14, 2021.

[121] D. W. O. Antillon, C. R. Walker, S. Rosset, and I. A. Anderson, "Glove-Based Hand Gesture Recognition for Diver Communication," *IEEE Transactions on Neural Networks and Learning Systems,* pp. 1-13, 2022.

[122] P. Pławiak, T. Sośnicki, M. Niedźwiecki, Z. Tabor, and K. Rzecki, "Hand Body Language Gesture Recognition Based on Signals From Specialized Glove and Machine Learning Algorithms," *IEEE Transactions on Industrial Informatics,* vol. 12, no. 3, pp. 1104-1113, 2016.

[123] S. Jiang, Q. Gao, H. Liu, and P. B. Shull, "A novel, co-located EMG-FMG-sensing wearable armband for hand gesture recognition," *Sensors and Actuators A: Physical,* vol.

301, p. 111738, 2020/01/01/ 2020.

[124] M. Tavakoli, C. Benussi, P. Alhais Lopes, L. B. Osorio, and A. T. de Almeida, "Robust hand gesture recognition with a double channel surface EMG wearable armband and SVM classifier," *Biomedical Signal Processing and Control,* vol. 46, pp. 121-130, 2018/09/01/ 2018.

[125] D. Esposito *et al.*, "A Piezoresistive Array Armband With Reduced Number of Sensors for Hand Gesture Recognition," *Frontiers in Neurorobotics,* Original Research vol. 13, 2020.

[126] X. Liang *et al.*, "Fusion of Wearable and Contactless Sensors for Intelligent Gesture Recognition," *Advanced Intelligent Systems,* vol. 1, no. 7, p. 1900088, 2019/11/01 2019.

[127] A. Moin *et al.*, "A wearable biosensing system with in-sensor adaptive machine learning for hand gesture recognition," *Nature Electronics,* vol. 4, no. 1, pp. 54-63, 2021/01/01 2021.

[128] T. Hastie, R. Tibshirani, and J. Friedman, *The elements of statistical learning: data mining, inference, and prediction*. Springer Science & Business Media, 2009.

[129] G. Li, D. Chen, C. Li, W. Liu, and H. Liu, "Engineered Microstructure Derived Hierarchical Deformation of Flexible Pressure Sensor Induces a Supersensitive Piezoresistive Property in Broad Pressure Range," *Advanced Science,* vol. 7, no. 18, p. 2000154, 2020.

[130] H. Chen *et al.*, "Omnidirectional Bending and Pressure Sensor Based on Stretchable CNT-PU Sponge," *Advanced Functional Materials,* https://doi.org/10.1002/adfm.201604434 vol. 27, no. 3, p. 1604434, 2017/01/01 2017.

[131] M. Zhu *et al.*, "Hollow MXene Sphere/Reduced Graphene Aerogel Composites for Piezoresistive Sensor with Ultra-High Sensitivity," *Advanced Electronic Materials,* https://doi.org/10.1002/aelm.201901064 vol. 6, no. 2, p. 1901064, 2020/02/01 2020.

[132] Y. Wei, S. Chen, X. Dong, Y. Lin, and L. Liu, "Flexible piezoresistive sensors based on “dynamic bridging effect” of silver nanowires toward graphene," *Carbon,* vol. 113, pp. 395-403, 2017/03/01/ 2017.

[133] J. Jia, G. Huang, J. Deng, and K. J. N. Pan, "Skin-inspired flexible and high-sensitivity pressure sensors based on rGO films with continuous-gradient wrinkles," *Nanoscale* vol. 11, no. 10, pp. 4258-4266, 2019.

[134] T. Gong *et al.*, "Highly responsive flexible strain sensor using polystyrene nanoparticle doped reduced graphene oxide for human health monitoring," *Carbon,* vol. 140, pp. 286-295, 2018/12/01/ 2018.

[135] J. Xu *et al.*, "Multifunctional Graphene Microstructures Inspired by Honeycomb for Ultrahigh Performance Electromagnetic Interference Shielding and Wearable Applications," *ACS Nano,* vol. 15, no. 5, pp. 8907-8918, 2021/05/25 2021.

[136] P. Tan *et al.*, "Self-powered gesture recognition wristband enabled by machine learning for full keyboard and multi-command input," *Advanced Materials,* https://doi.org/10.1002/adma.202200793 vol. 34, no. 21, p. 2200793, 2022/05/01 2022.

[137] S. Jiang *et al.*, "Feasibility of Wrist-Worn, Real-Time Hand, and Surface Gesture Recognition via sEMG and IMU Sensing," *IEEE Transactions on Industrial Informatics,* vol. 14, no. 8, pp. 3376-3385, 2018.

[138] P. B. Shull, S. Jiang, Y. Zhu, and X. Zhu, "Hand Gesture Recognition and Finger Angle Estimation via Wrist-Worn Modified Barometric Pressure Sensing," *IEEE Transactions on Neural Systems and Rehabilitation Engineering,* vol. 27, no. 4, pp. 724-732, 2019.

[139] D. Jiang, Y. Wu, and A. Demosthenous, "Hand Gesture Recognition Using Three-Dimensional Electrical Impedance Tomography," *IEEE Transactions on Circuits and Systems II: Express Briefs,* vol. 67, no. 9, pp. 1554-1558, 2020.

[140] N. Siddiqui and R. H. M. Chan, "Hand Gesture Recognition Using Multiple Acoustic Measurements at Wrist," *IEEE Transactions on Human-Machine Systems,* vol. 51, no. 1, pp. 56-62, 2021.

[141] Y. T. Liu, Y. A. Zhang, and M. Zeng, "Novel Algorithm for Hand Gesture Recognition Utilizing a Wrist-Worn Inertial Sensor," *IEEE Sensors Journal,* vol. 18, no. 24, pp. 10085-10095, 2018.

[142] J. Hirschberg, P. H. Dejonckere, M. Hirano, K. Mori, H. J. Schultz-Coulon, and K. Vrtička, "Voice disorders in children," *International Journal of Pediatric Otorhinolaryngology,* vol. 32, pp. S109-S125, 1995/06/01/ 1995.

[143] R. Kaye, C. G. Tang, and C. F. Sinclair, "The electrolarynx: voice restoration after total laryngectomy," (in eng), *Medical devices,* vol. 10, pp. 133-140, 2017.

[144] H. Liu and M. L. Ng, "Electrolarynx in voice rehabilitation," *Auris Nasus Larynx,* vol. 34, no.

3, pp. 327-332, 2007/09/01/ 2007.

[145] K. Takei, W. Honda, S. Harada, T. Arie, and S. Akita, "Toward Flexible and Wearable Human-Interactive Health-Monitoring Devices," *Advanced Healthcare Materials,* https://doi.org/10.1002/adhm.201400546 vol. 4, no. 4, pp. 487-500, 2015/03/01 2015.

[146] Y. Zang, F. Zhang, C.-a. Di, and D. Zhu, "Advances of flexible pressure sensors toward artificial intelligence and health care applications," *Materials Horizons,* vol. 2, no. 2, pp. 140-156, 2015.

[147] T. Nguyen *et al.*, "Advances in ultrasensitive piezoresistive sensors: from conventional to flexible and stretchable applications," *Materials Horizons,* 10.1039/D1MH00538C vol. 8, no. 8, pp. 2123-2150, 2021.

[148] R. B. Mishra, N. El-Atab, A. M. Hussain, and M. M. Hussain, "Recent Progress on Flexible Capacitive Pressure Sensors: From Design and Materials to Applications," *Advanced Materials Technologies,* https://doi.org/10.1002/admt.202001023 vol. 6, no. 4, p. 2001023, 2021/04/01 2021.

[149] Y. Liu *et al.*, "Piezoelectric energy harvesting for self-powered wearable upper limb applications," *Nano Select,* vol. 2, no. 8, pp. 1459-1479, 2021.

[150] X.-S. Zhang, M. Han, B. Kim, J.-F. Bao, J. Brugger, and H. Zhang, "All-in-one self-powered flexible microsystems based on triboelectric nanogenerators," *Nano Energy,* vol. 47, pp. 410-426, 2018/05/01/ 2018.

[151] X.-S. Zhang *et al.*, "Frequency-Multiplication High-Output Triboelectric Nanogenerator for Sustainably Powering Biomedical Microsystems," *Nano Letters,* vol. 13, no. 3, pp. 1168-1172, 2013/03/13 2013.

[152] Y. Ma *et al.*, "A highly flexible and sensitive piezoresistive sensor based on MXene with greatly changed interlayer distances," *Nature Communications,* vol. 8, no. 1, p. 1207, 2017/10/31 2017.

[153] Q. Zheng, J.-h. Lee, X. Shen, X. Chen, and J.-K. Kim, "Graphene-based wearable piezoresistive physical sensors," *Materials Today,* vol. 36, pp. 158-179, 2020/06/01/ 2020.

[154] C. Ma *et al.*, "Robust Flexible Pressure Sensors Made from Conductive Micropyramids for Manipulation Tasks," *ACS Nano,* vol. 14, no. 10, pp. 12866-12876, 2020/10/27 2020.

[155] Z. Han *et al.*, "Ultralow-Cost, Highly Sensitive, and Flexible Pressure Sensors Based on Carbon Black and Airlaid Paper for Wearable Electronics," *ACS Applied Materials & Interfaces,* vol. 11, no. 36, pp. 33370-33379, 2019/09/11 2019.

[156] S. Gong *et al.*, "A wearable and highly sensitive pressure sensor with ultrathin gold nanowires," *Nature Communications,* vol. 5, no. 1, p. 3132, 2014/02/04 2014.

[157] Y. Ma and L. Zhi, "Graphene-Based Transparent Conductive Films: Material Systems, Preparation and Applications," *Small Methods,* https://doi.org/10.1002/smtd.201800199 vol. 3, no. 1, p. 1800199, 2019/01/01 2019.

[158] J. A. Quezada-Renteria, C. O. Ania, L. F. Chazaro-Ruiz, and J. R. Rangel-Mendez, "Influence of protons on reduction degree and defect formation in electrochemically reduced graphene oxide," *Carbon,* vol. 149, pp. 722-732, 2019/08/01/ 2019.

[159] L.-Q. Tao *et al.*, "An intelligent artificial throat with sound-sensing ability based on laser induced graphene," *Nature Communications,* vol. 8, no. 1, p. 14579, 2017/02/24 2017.

[160] Y. Wei *et al.*, "A Wearable Skinlike Ultra-Sensitive Artificial Graphene Throat," *ACS Nano,* vol. 13, no. 8, pp. 8639-8647, 2019/08/27 2019.

[161] D. Ravenscroft, I. Prattis, T. Kandukuri, Y. A. Samad, G. Mallia, and L. G. Occhipinti, "Machine Learning Methods for Automatic Silent Speech Recognition Using a Wearable Graphene Strain Gauge Sensor," *Sensors*, vol. 22, no. 1. doi: 10.3390/s22010299

[162] Y. Qiao *et al.*, "Intelligent and highly sensitive strain sensor based on indium tin oxide micromesh with a high crack density," *Nanoscale,* 10.1039/D1NR08005A vol. 14, no. 11, pp. 4234-4243, 2022.